Peyman Mohseni

Brittle and Ductile Fracture of X80 Arctic Steel

Thesis for the degree of Philosophiae Doctor

Trondheim, October 2012

Norwegian University of Science and Technology
Faculty of Natural Sciences and Technology
Department of Materials Science and Engineering

NTNU – Trondheim
Norwegian University of
Science and Technology

NTNU
Norwegian University of Science and Technology

Thesis for the degree of Philosophiae Doctor

Faculty of Natural Sciences and Technology
Department of Materials Science and Engineering

ISBN 978-82-471-3824-3 (printed ver.)
ISBN 978-82-471-3825-0 (electronic ver.)
ISSN 1503-8181

Doctoral theses at NTNU, 2012:258
IMT-Report 2012:161

Printed by NTNU-trykk

Preface

This thesis is submitted in partial fulfilment of the requirements for the degree of philosophiae doctor (PhD) at the Norwegian University of Science and Technology (NTNU) in Trondheim. The work presented in this thesis has been carried out at the Department of Materials Science and Engineering at NTNU in the period of August 2008 to August 2012.

This project was financed by the Norwegian Research Council (NRC) as an Institution based Strategic Project (ISP) and by Norwegian University of Science and Technology (NTNU). During the work, I have had a close cooperation with the NRC-financed Petromaks Programme "Arctic Materials", which also has financed parts of the work. This project was cooperation between NTNU and Industrial Research (SINTEF) in Norway.

This work has been supervised by Professor Jan Ketil Solberg at Department of Materials Science and Engineering, NTNU, Trondheim, as the main supervisor and Professor II Morten Karlsen at Department of Materials Science and Engineering, NTNU, Tondheim, as a co-supervisor.

The main results presented in this thesis have been published, or are in the process of being published, in international scientific journals, including *Materials Science and Technology, Materials Science and Engineering A, Journal of Microscopy* and *Metallurgical and Materials Transaction A*.

Trondheim, August 2012.

Peyman Mohseni

Acknowledgements

First of all, I would like to express my sincere gratitude to my supervisor, Professor Jan Ketil Solberg, for his support, guidance and encouragement throughout the work on the thesis. Thank you giving me the opportunity to be a part of your research group. In addition, I always appreciate his ongoing friendship, care and support on a personal level. I would also like to acknowledge my co-supervisor Professor II Morten Karlsen, Statoil, for his valuable discussions in this work.

I greatly appreciate the cooperation with Professor II Odd Magne Akselsen and Dr. Erling Østby, Department of Applied Mechanics and Corrosion, SINTEF for their valuable comments and guidance.

I would like to thank the technical staff at the Department of Materials Science and Engineering, NTNU, for their help and cooperation with the experimental work. I would like to thank Pål Ulseth, Torild Krogstad, Dr. Yinga Yu, Morten Raanes, Tor Nilsen and Wilhelm Dall. It has been a pleasure to work with all of them.

I want to thank PhD candidates Masoud Asgari, Amin Shahrestani Azar, and Dr. Christopher Nwakwuo for their assistance in the laboratory work and discussions at different stages of the work. I also acknowledge all my other colleagues at the department for providing a sociable and an inspiring work environment.

I am thankful to Salma and all my friends that I met during these years.

Finally, I am grateful to my parents, and I would like to dedicate this work to them for their patience, continuous support and encouragement and providing me with moments of full happiness.

Abbreviations

ACC	Accelerated Controlled Cooling
AFM	Atomic Force microscopy
ASM	American Society for Metals
BCC	Body Centred Cubic
CGHAZ	Coarse Grained Heat Affected Zone
CTOD	Crack Tip Opening Displacement
DBTT	Ductile to Brittle Transition Temperature
EBSD	Electron Backscatter Diffraction
EDS	Energy Dispersive Spectroscopy
EPMA	Electron Probe Micro Analysis
FIB	Focused Ion Beam
FCC	Face Centred Cubic
HAZ	Heat Affected Zone
HSLA	High Strength Low Alloy
ICCGHAZ	Intercritically Coarse Grained Heat Affected Zone
ICGHAZ	Intercritical Heat Affected Zone
LVFESEM	Low Vacuum Field Emission Scanning Electron Microscopy
M-A	Martensite – Austenite Constituent
ND	Normal Direction
RD	Rolling Direction
SADP	Selected Area Diffraction Pattern
SCHAZ	Subcritical Heat Affected Zone
SEM	Scanning Electron Microscopy
SPM	Scanning Probe Microscopy
STM	Scanning Tunneling Microscopy
TEM	Transmission Electron Microscopy
TD	Transverse Direction
TMCP	Thermo Mechanical Controlled Process
WDS	Wavelength Dispersive Spectroscopy

Summary of Publications

The experimental results from the present PhD work have been or will be presented in the following scientific publications and oral presentations:

- P. Mohseni, JK. Solberg, M. Karlsen, OM. Akselsen, E. Østby: "Investigation of the mechanism of cleavage fracture initiation in the intercritically coarse grained heat affected zone of an HSLA steel", Materials Science and Technology, (In Press), DOI: 10.1179/1743284712Y.0000000056.
- P. Mohseni, JK. Solberg, M. Karlsen, OM. Akselsen, E. Østby: "Cleavage fracture initiation at M-A constituents in the intercritically coarse grained heat affected zone of a HSLA steel", Submitted to Metallurgical and Materials Transaction A.
- P. Mohseni, JK. Solberg, M. Karlsen, OM. Akselsen, E. Østby: "Slip system activation during low cycle fatigue at low temperatures in HSLA steels", Submitted to Materials Science and Engineering A.
- P. Mohseni, JK. Solberg, M. Karlsen, OM. Akselsen, E. Østby: "Application of combined EBSD and 3D-SEM technique on crystallographic facet analysis of the X80 steel at low temperature", Submitted to Journal of Microscopy.
- P. Mohseni, JK. Solberg, M. Karlsen, OM. Akselsen, E. Østby: "Determination of crystallographic facet orientation of fracture surface in Arctic steels at low temperature by using EBSD", Proceedings of ISOPE 2012, Rhodes, Greece, June 18-24, Vol.4, pp. 305-309.
- P. Mohseni, JK. Solberg, OM. Akselsen, E. Østby: "Application of electron backscatter diffraction (EBSD) on face crystallographic orientation studies in Arctic steels", Proceedings of ISOPE 2011, Hawaii, USA June 19-24, Vol. 4, pp 402-406.

- P. Mohseni, JK. Solberg, M. Karlsen, OM. Akselsen, E. Østby: "Application of electron backscatter diffraction (EBSD) on fractography analysis of Arctic Steels at low temperatures", Nasjonal Konferanse for Materialteknologi, Sommermøte 2012, Trondheim, Norway, May 9 & 10, 2012.
- P. Mohseni, JK. Solberg, OM. Akselsen, E. Østby: "Application of electron backscatter diffraction (EBSD) on facet crystallographic orientation studies in Arctic Steels", 6th NTNU, EBSD workshop, 2010, May 31, 2010.
- P. Mohseni, JK. Solberg, OM. Akselsen, E. Østby: "Brittle and Ductile fracture of Arctic Steels", Meeting at AkerSolutions, Fornebu, Norway, November 9, 2010.

Abstract

This PhD work has focused on the effect of microstructure and changes in microstructure introduced by welding procedure, on the brittle to ductile transition properties of high strength low alloy steels which have been developed for application at low temperatures (Arctic regions). For this purpose, the experimental work was based on the new pipeline steel API X80 that has a low transition temperature. The relationship between the brittle to ductile transition temperature and the microstructure in the coarse grained heat affected zone, CGHAZ, and the intercritically reheated coarse grained heat affected zone, ICCGHAZ was studied by applying Smitweld TCS1405 weld simulation for producing the HAZ microstructures. During the weld thermal cycles, both single and double cycle, the specimens were resistance heated to 1350°C by a rate of 150°C/s. The cooling rate was adjusted to give a cooling time between 800°C and 500°C ($\Delta t_{8/5}$) of 15 seconds. The second heating cycle had a peak temperature, T_{p2}, of 780°C, and the cooling rate was the same as during the first cycle to simulate the reheated intercritical coarse grained HAZ. Fracture toughness was measured at low temperatures down to -90°C by both tensile and CTOD testing. In order to study the slip system activity of this steel, low cycle three point bending fatigue tests were also performed on polished specimens in the same temperature range. Fracture surfaces and changes in microstructure were analyzed by scanning and transmission electron microscopy and by light optical microscopy.

In summary, the present work showed that, at each temperature the ICCGHAZ specimens had lower fracture toughness values than the CGHAZ specimens. Thus, the fracture mechanism is potentially more brittle in the case of ICCGHAZ specimens, and this is probably connected to the microstructure. The microstructure evalutions revealed that the ICCGHAZ contained blocky M-A constituents along prior austenite grain boundaries and stringer M-A constituents between the bainite laths. A more detailed investigation of the fracture surfaces by electron microscopy revealed also the existence of M-A constituents at the initiation points of the

cleavage cracks. During deformation, the stress concentration is expected to increase due to the presence of the M-A constituents, and thus the level of stress and strain concentration around the M-A constituents become significantly larger than the nominal stress value and then causes initiation of cleavage fracture. Fracture surface analysis of fractured specimens documented that the cracks initiated either from debonded M-A constituents or from the region between two or more closely separated blocky M-A constituents where the transformation induced stress fields overlapped.

In the present work, the initiation of cleavage fracture occurred within the double CTOD distance from the crack tip. This implies that brittle fracture is easily initiated when M-A constituents are located near the fatigue crack tip, and it is also controlled by accumulation of continuum stress fields and local plastic strains.

The slip system analysis revealed that several slip systems are activated with a variety of Schmid factors within one grain, and in some cases the first activated slip system is not necessarily that with the highest Schmid factor. Thus, it can be concluded that the Schmid factor is not the only parameter that determines activation of slip.

Finally, the crystallographic facet analysis by EBSD illustrated that the {100} planes are the most potent cleavage facet planes in both CGHAZ and ICCGHAZ specimens. It was also shown that the {100} and {110} planes in the case of CGHAZ, and the {100} and {211} planes in the case of ICCGHAZ were the most favourable cleavage facet planes at subzero temperatures.

Table of Contents

1. Introduction

High strength low alloy (HSLA) steels can provide an excellent combination of strength and toughness over a wide range of plate thickness for different applications such as oil and gas pipelines. Thermo-mechanically controlled processing (TMCP) followed by accelerated controlled cooling (ACC) of these steels can optimize the required microstructural features. HSLA steels are used for high pressure pipeline operations to improve the transportation efficiency and pipeline safety and offshore structural installations. Due to their excellent combination of mechanical properties and excellent low temperature fracture toughness (ductile to brittle transition properties) pipeline steels are used for transporting oil and gas over long distances. Pipelines are sometimes installed in severe environments such as in the Arctic regions [1, 2]. Thus, the demand for high strength, good fracture toughness and weldability at low temperatures of pipeline steels has increased. In order to achieve the best welding procedure and safety against brittle fracture, especially at low temperatures, it is essential to understand the mechanism of phase transformations within the heat affected zone, which in many cases is considered to be the most critical part of the weld [3-5]. Low temperature performance and capability to resist heavy deformation are two features of large interest in Arctic applications of steel structures. The low temperature requirements raise the focus on brittle fracture behaviour [6, 7].

The transition temperature of structural steels is the temperature at which there occurs a sudden drop in the failure energy caused by a change of fracture mechanism from void coalescence to cleavage. Even though the change of fracture properties at low temperatures has been known for more than a century, some of the fundamentals controlling the transformation temperature have not yet been adequately explained [8]. The parameters that affect this transition are e.g. the chemical composition of the steel, its microstructure (grain size, phase composition, morphology of pearlite/cementite, slag particles like MnS, etc.), crystallographic texture, aging, cold deformation, surface notches, geometrical conditions, loading

history, and the occurrence of deformation twinning (nucleating cleavage) prior to final fracture. Moreover, welding introduces new chemical compositions (due to filler metal) and changes in the microstructure (HAZ). Due to these complex relations there is a lack of specifications for structural installations at arctic temperatures. There is a need for a deeper understanding of the factors that influence the brittle to ductile transition temperature to (i) provide background knowledge for steel development, (ii) for making specifications for oil and gas installations under arctic conditions (e.g. welding procedures), and (iii) for avoiding brittle fracture due to extreme ice interactions (cold deformation introduced by ice loadings may enhance the risk for subsequent brittle fracture through an increase in the brittle to ductile temperature).

1. 1 Objective

The main aim of this work is to increase our knowledge on mechanisms of brittle fracture in HSLA steels at low temperatures, in order to develop improved steel qualities for the extremely demanding conditions met in the Arctic. The focus is to identify the effect of microstructure and changes in microstructure introduced during the welding process that affect the ductile to brittle transition of steels for Arctic applications.

2. Theoretical Background

2.1 High Strength Low Alloy Steels

2. 1. 1 History of HSLA Steels

In the early 1960's, high strength steels were developed for naval applications. Ferrite-pearlite steels were used for many years for high strength structural applications. Medium carbon low alloy steels in quenched and tempered conditions were also usually used in engineering structures. The demands on high strength steels have increased for special reasons such as: (a) higher yield strength for larger load bearing capacity of thin sections, (b) higher resistance to brittle fracture with low impact transition temperature, and (c) a high degree of weldability, which are the main reasons for advancements of high strength steels [9]. Thus, a new series of low carbon steels has been developed based on (1) low carbon content, (2) sufficient alloying elements to achieve required transition temperatures, and (3) microstructural refinement by microalloying and thermomechanical processing [10].

High strength low alloy steels are used for high pressure pipeline operations to improve the transportation efficiency and pipeline safety. Steel pipelines, used for transporting natural gas and oil over long distances, became stronger, tougher, larger and thicker for cost reductions and high pressure transportations. Hence, a larger volume of oil and gas can be transported in a given time over longer distances by simply increasing the operating pressure [1, 2]. This has also resulted in the quest for higher strength steel pipelines, enabling a reduction in both wall thickness and diameter of a pipeline for a given pressure. Further incentives were decreased construction costs and reduced pipeline steel volumes. In addition, decreased wall thickness decreases the construction time, due to the lower volume of weld metal deposition [11].

Strength levels have increased through projects such as the Trans Siberian pipeline (X70) and the Ruhrags pipeline (X80), with toughness levels increased to cope with

the greater wall thickness and colder environments, like in the Arctic regions [12]. The requirements behind high strength pipeline steel development are shown schematically in Fig. 1.

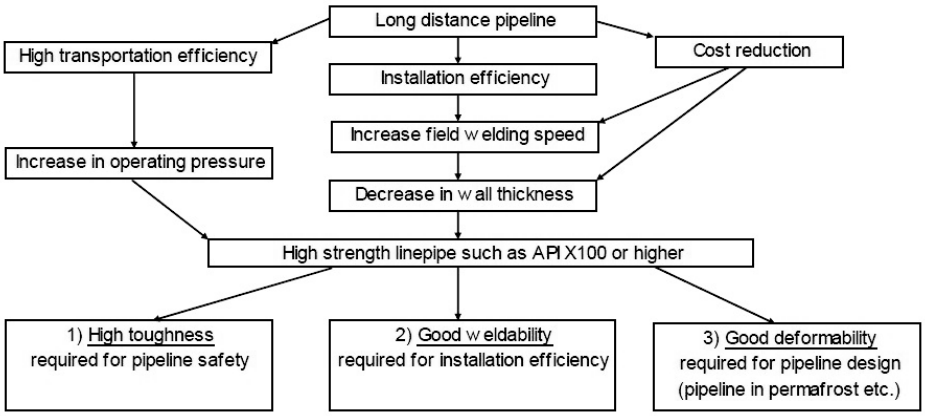

Fig. 1. *The requirements of high strength steel pipelines [13].*

A summary of pipeline development from the mid 1960's to the early 1990's is given in the following:

- API 5L X52 was one of the first high strength low alloy pipeline steels to be used for the transportation of oil and gas. The microstructure essentially consisted of ferrite and pearlite with varying amounts of interspersed pearlite.

- The API 5L X70 pipeline steel is generally categorized as being ferritic-pearlitic structured [14]. X70 was introduced to satisfy the higher strength and toughness requirements. Improvements in mechanical properties were achieved by a combination of strengthening mechanisms, microalloying and TMCP technology [15].

- API 5L X80 pipeline steel. Whereas the X70 pipeline steel has a predominantly ferrite and pearlite microstructure, X80 steels are said to comprise a ferritic/bainitic microstructure [16], or tempered bainite and tempered martensite

[17]. The chemical composition of X80 is based on low carbon and high manganese contents, with microalloying combinations typically involving niobium and titanium or niobium and vanadium. Additional elements such as copper, chromium, nickel, molybdenum and boron are sometimes present.

2. 1. 2 Physical Metallurgy of HSLA Steels

Classification

The American Society for Metals (ASM) has classified the different types of high strength low alloy steels into four main categories described as follows [18a, 18b]:

1- As hot-rolled pearlitic high strength low alloy steels with minimum yield strength of 275-345 MPa.

2- Microalloyed HSLA steels with properties that result from low alloy element additions and controlled hot rolling with minimum yield strength of 275-450 MPa.

3- High strength structural carbon steels either in normalized or in quenched and tempered condition with minimum yield strength of 290-690 MPa.

4- Quenched and tempered low alloy steels with minimum yield strength of 620-690 MPa.

Alloying Elements

Microalloying elements and chemical composition are two significant factors that affect the microstructure and properties of HSLA steels. For instance, in order to achieve a proper grain refinement and precipitation hardening, some microalloying elements such as niobium, titanium and vanadium have been added to the steels. In general, the total amount of alloying elements is less than 3 wt%. Alloying elements such as nickel, copper, chromium and molybdenum can be used to improve strength, toughness, hardenability, corrosion resistance and weldability properties of HSLA steel for specific applications. In order to control HAZ hardness, toughness and cold cracking, the level of carbon is kept below 0.07 wt% [19]. Cr, Ni and Mo can improve the toughness of the steel. The hardenability is raised by the addition of Ni,

Mn, and Mo. The corrosion resistance in marine environments can also be improved by the addition of Cu, Mo and Cr [20-24].

Carbon is typically used to increase the strength of the steel. Carbides and carbonitrides form upon adding carbon to the steel composition, and this has a major effect on the mechanical properties of the steels. The higher levels of carbon can deteriorate weldability and low temperature toughness of HSLA steels. HSLA steels with low carbon content have been developed due to increasing demand of high toughness at low temperatures for pipelines with good weldability and formability [25, 26].

Manganese can also be added in a wide range of wt%, and it acts as austenite stabilizer and carbide former. Mn prevents hot-shortness, which is due to the presence of sulphur. Hardenability, without a reduction in toughness, can be increased by the addition of manganese. It can also decrease the ductile to brittle transition temperature of the steel [27].

The hardenability of steels can be influenced by adding *chromium*, *nickel*, and *molybdenum*, which also increases solid solution strengthening. It has been reported that Ni up to 3.5 wt% alone or in combination with Cr was initially used to modify HSLA steels [28, 30]. Cr can raise the yield strength and the corrosion resistance properties and it also depresses the austenite transformation temperature. Cr, Mn and B are used in places of Mo as hardenability agents. Mo is added due to its effect on continuous cooling transformation characteristics. The hot shortness can be reduced by suppressing the boundary segregation of copper with the addition of nickel [19, 27].

Titanium, vanadium and *niobium* can act as grain refiners and precipitation formers in HSLA steels. These microalloying elements are strong carbide and nitride forming elements even at very low concentrations, and they increase strength, ductility and toughness [31]. The strengthening mechanisms are related to precipitation hardening, grain refining and dislocation hardening mechanisms. Nb

gives a significant grain refinement with moderate precipitation hardening, while V imparts moderate strengthening with relatively weak grain refinement. Ti imparts strength through precipitation hardening and grain refinement [32].

Silicon is well known as a ferrite strengthener, and it increases the tensile strength with loss in ductility and increases impact transition temperature [28]. *Aluminium* contributes to the formation of fine grained steel; when added to the steel, it forms fine aluminium nitrides. Microalloying elements like *titanium*, *vanadium* and *niobium* combines with nitrogen to form nitrides and/or carbonitrides, which can act as grain refiners. They can also act as a precipitation formers in order to increase the strength of the steel [29]. *Nitrogen* beyond a certain amount is not a desirable element in steels. Due to the detrimental effects of s*ulphur* and *phosphorus* on the properties of steels, their content should be less than 0.02 wt% in HSLA steels.

Copper can be added as a grain refiner as well as a precipitation and solid solution strengthener. The strength in Cu-bearing steels through age hardening can be increased by adding copper, and it can improve the toughness as well as corrosion resistance of steels [33]. Furthermore, Cu reduces the transformation temperature of martensite (M_s) and bainite (B_s) upon quenching from austenite (γ) at 900ºC. Okada et al. showed that higher amount of Cu (>1.5 wt %) in combination with Mn decreases the transformation temperature of austenite in HSLA steels [34].

2. 1. 3 Microstructural Evolution

The thermomechanical procedure and the microalloying elements control the final microstructures of HSLA steels. The formation of different phases in HSLA steels, ferrite-pearlite, acicular ferrite, bainitic ferrite, martensite, and martensite-austenite (M-A) constituents depend on the mechanism of the transformation kinetics of austenite. Several factors like transformation temperature and the amount of deformation etc. can also affect the transformation kinetics of austenite.

A summary of microstructure evaluation of HSLA steels after welding process is given in the following:

Formation of Acicular Ferrite

The formation of acicular ferrite occurs during continuous cooling at a temperature range slightly higher than the temperature range of bainitic transformation. The microstructure of acicular ferrite consists of non-equiaxed ferrite with a little amount of dispersed carbide. The acicular ferrite microstructure has the potential of combining high strength and high toughness. Reason for this is that the plates of acicular ferrite nucleate intragranularly on non-metallic inclusions within large austenite grains, and grow in many different orientations from those inclusions whilst maintaining an orientation relationship with the austenite. The resulting microstructure is less organized when compared with ordinary bainite or Widmanstätten ferrite, where there is a tendency to form packets of parallel plates which are identically oriented [6, 7]. A crack therefore has to follow a more tortuous path through an acicular ferritic microstructure, thereby leading to improved toughness without compromising strength [35].

An optimum microstructural combination with respect to HAZ toughness is one that is dominated by acicular ferrite with evenly dispersed M-A constituents between acicular ferrite plates rather than the highest level of acicular ferrite [83]. In addition to acicular ferrite, the toughness of the HAZ depends on the amount, type and distribution of M-A constituents that form during intercritical heating of the prior weld bead (ICCGHAZ) and the base plate (ICHAZ).

Formation of Bainite

Bainite forms during thermal treatment at cooling rates too fast for pearlite to form, yet not rapid enough to produce martensite. Two main forms can be identified: upper and lower bainite. This latter distinction is valuable because there are clear differences in the mechanical properties of upper and lower bainite [36].

Upper bainite consists of fine plates of ferrite, each of which is about 0.2 μm thick and about 10 μm long. The plates grow in clusters called sheaves. Upper bainite evolves in distinct stages beginning with the nucleation of ferrite plates at the austenite grain boundary.

Lower bainite is obtained by transformation at relatively low temperatures. Lower bainite has a microstructure and crystallographic features which are very similar to those of upper bainite. The major difference is in the nature of the carbide precipitates in that carbides also precipitate inside the ferrite plates of lower bainite. The transition between upper and lower bainite is believed to occur over a narrow range of temperature. It is possible for both forms to occur simultaneously during isothermal transformation near the transition temperature, as depicted in Fig. 2 [37].

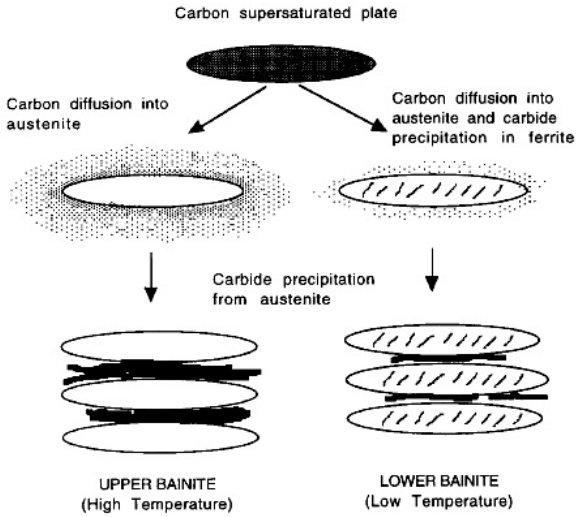

Fig. 2. *Schematic representation of transition from upper to lower bainite [37].*

The main difference between bainite (bainitic ferrite) and acicular ferrite is related to the nucleation and growth mechanism. In bainite, ferrite constituent initiates on the austenite grain boundaries, forming sheaves of parallel plates with nearly the same crystallographic orientation. However, acicular ferrite nucleates intragranularly at nonmetalic inclusions, within large austenite grains and on the surfaces of existing acicular ferrite laths, Fig. 3 [38-40].

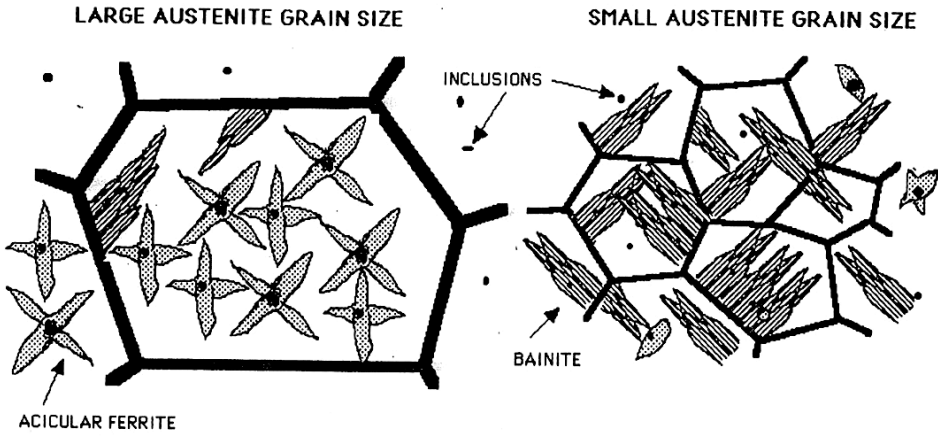

Fig. 3. *Schematic illustration of the nucleation and growth mechanism of acicular ferrite and bainite [39].*

Formation of Martensite

The quenching to room temperature of austenite can lead to the formation of martensite, a very hard phase in which the carbon, formerly in solid solution in the austenite, remains in solution in the new phase [36]. Unlike ferrite or pearlite, martensite forms by a deformation of the austenite lattice without any diffusion of atoms. The deformation causes a change in the shape of the transformed region, caused by a large shear and a volume expansion. The formation of martensite is therefore often referred to as a diffusionless shear transformation, which is highly crystallographic in character because it is generated by a specific deformation of the austenite. When the formation of martensite is constrained by its surroundings, it forms as thin plates or laths in order to minimize the strain energy due to the deformation [37].

Formation of M-A Constituents

The M-A constituents are formed in the intercritically reheated coarse grained HAZ (ICCGHAZ). During multipass welding, the former CGHAZ is reheated between the A_{c1} and A_{c3} temperature range. Thus, parts of the microstructure were

transformed into austenite, which nucleated and grew preferentially along the prior austenite grain boundaries and bainite lath boundaries [49]. These austenite islands became enriched in carbon due to the high diffusivity of carbon in ferrite and its high solubility in austenite, and they transformed to M-A constituents during the subsequent cooling stage [45]. The amount of M-A constituents increases with carbon and alloy contents of the steel. In addition, boron, nitrogen, niobium, aluminium and vanadium enhance the formation of M-A constituents [6, 7]. The peak temperature of the CGHAZ thermal cycle and the prior austenite grain size have a minor influence on the amount of M-A constituents, but they probably have a significant influence on their distribution [3, 6, 7, 41].

2. 2 Effect of welding procedure

In order to achieve the best economic welding and safety against brittle failure it is essential to understand the mechanisms of phase transformations in the heat affected zone and the key effects of the microstructure on resistance to brittle fracture. The cleavage fracture resistance of bainitic microstructures is closely related to both prior austenite grains and bainite packets [6, 43].

The combination of high strength and high fracture toughness of a steel can be deteriorated after welding thermal cycles. The degradation of the fracture toughness after welding is attributed to the formation of "local brittle zones" in the welded joints. Significant embrittlement can be encountered in the coarse-grained heat affected zone (CGHAZ), in particular, and in the intercritically reheated CGHAZ (ICCGHAZ) of multipass welds [7, 44, 45].

The heat affected zone is in many cases considered to be the most critical part of the weld. The region of lowest toughness after the welding procedure is related to the heat affected zone (HAZ). In general, the coarse grained HAZ (CGHAZ) and the intercritically reheated coarse grained HAZ (ICCGHAZ) is considered to have the lowest toughness after single and multipass weld thermal cycles, respectively.

However, investigations on normalized ferritic/pearlitic offshore steels and on low carbon thermomechanically processed steels have shown that the lowest toughness is sometimes found in the intercritical HAZ (ICHAZ) or subcritically reheated coarse grained HAZ (SCHAZ) [1, 4, 5, 44, 46, 47]. During double pass welding, the first CGHAZ is modified by the second pass thermal cycle forming localized zones.

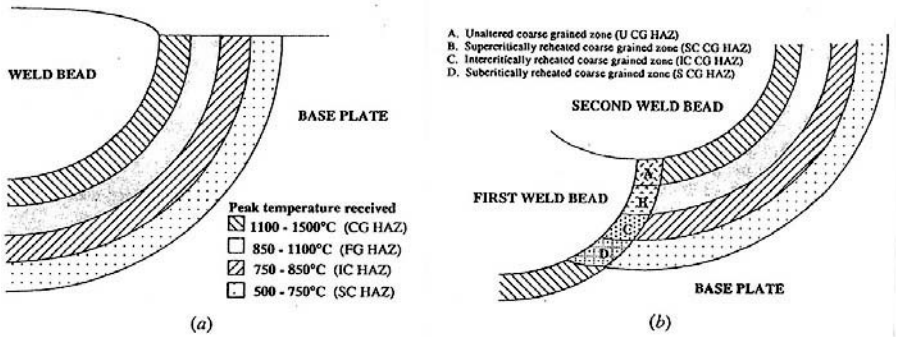

Fig. 4. *Schematic presentation of microstructures in (a) single or (b) multipass weld [47].*

According to data in the literature, the fracture toughness of these local brittle zones are influenced by metallurgical factors such as prior austenite grain size, bainite packet size, and the distribution of second phases such as carbides and martensite-austenite (M-A) constituents [4, 5, 46, 48-50]. The cleavage facet size has been related to the prior austenite grain size. The bainite packet boundaries influence the brittle fracture properties of the heat affected zone (HAZ) in bainitic steels, and M-A constituents have a deleterious effect on both crack initiation and propagation. However, the correlation between welding thermal cycles, the resulting microstructures, and the fracture toughness properties has not by far been clarified in detail [6, 7, 41]. Improvements in weldability, on the other hand, provide a challenging problem because weldability is determined by a combination of weld joint, welding procedure, welding technology and alloy composition and properties. However, from a metallurgical point of view, weldability includes hardenability, HAZ properties, HAZ and weld metal cracking and response of steels to post-weld heat treatments [41].

In consequence, the technique used to manufacture steel can significantly affect the toughness of the heat affected zone [51]. Modern steelmaking technology has made new possibilities for manufacturing high strength thermomechanical by controlled processing (TMCP) steels. Such improvements include a better control of titanium microalloying and nitrogen levels as well as the use of titanium killing, both of which can be expected to improve the toughness of the base plate and the weld HAZ. In titanium killed plates, titanium oxide particles are known to facilitate the nucleation of acicular ferrite intragranularly, improving the toughness of the HAZ as has been shown in laser welded joints. This has opened up the use of titanium killed steels for offshore structures and pipes, where a good fracture toughness of the coarse grained HAZ can be guaranteed after high heat input welds. Titanium killing is also applied to improve the toughness of the filler metal. Normally, the high and intermediate oxygen content (200–800 ppm) in the weld metal of conventionally welded (SMAW, GMAW, SAW) joints can provide enough favourable inclusions for the nucleation of acicular ferrite [52-55].

2. 3 Martensite-Austenite (M-A) constituents

In high strength low alloy steels, M-A constituents can form within intercritical HAZ (ICHAZ) and intercritically reheated coarse grained HAZ (ICCGHAZ). During intercritical heating of low carbon microalloyed steels, austenite grows rapidly into the pearlite until the dissolution process is completed. The transformation continues into the ferrite at a rate controlled by either carbon diffusion in the austenite or diffusion of substitutional elements (for example manganese) in the ferrite [4, 46].

The intercritically reheated coarse grained HAZ is formed by reheating the CGHAZ into the mixed austenite and ferrite region (between A_{c1} and A_{c3}) during multipass welding, and therefore consists of bainite (or martensite, depending on heat input) with a large prior austenite grain size. During the second thermal cycle, austenite nucleates and grows preferentially along the prior austenite grain boundaries and

bainite lath boundaries. Due to the high heating rate of the weld thermal cycle and the short time in the intercritical temperature region, only carbon is partitioned between ferrite and austenite. The austenite islands are thus enriched in carbon, and finally they transform to hard and brittle M-A constituents during the subsequent cooling stage [4, 45, 49, 56, 57].

The temperatures A_{c1} and A_{c3} specify the temperatures at which ferrite starts to transform to austenite and when the transformation is completed [58]. Andrews has proposed the following equations for predicting A_{c1} and A_{c3} (elements in wt %):

A_{c1} (ºC) = 723 - 10.7Mn - 3.9Ni + 29Si + 16.7Cr + 290As + 6.38W
A_{c3} (ºC) = 910 - 230$C^{0.5}$ - 15.2Ni + 44.7Si + 104V + 31.5Mo + 13.1W

Both equations are valid for low alloy steel containing less than 0.6 wt% C [59].

The M-A constituents play an important role in the control of the fracture toughness of the HAZ. They cause a sudden drop in toughness because of the crack susceptibility of martensite. Earlier investigations have shown that the toughness of the ICCGHAZ is mainly controlled by the size and volume fraction of high carbon M-A constituents [60]. However, it has also been reported that the loss in toughness is not only due to the presence of M-A, but that it is also related to the morphology and distribution of the M-A constituents, as well as the matrix microstructure [49].

2. 3. 1 Formation mechanism

The main transformation products of carbon rich austenite after rapid cooling are martensite in lath or plate form and retained austenite. In some cases, the simulated heat affected zone of high strength steels contains M-A constituents that may contain cementite precipitated from retained austenite at higher temperatures as well as precipitated from lath martensite during self-tempering [61]. The transformation

to martensite is accomplished with the maximum expenditure of strain energy by a homogeneous distortion of the austenite. The strain can occur either by slip at higher martensite start (M_s) temperatures or by twinning at lower M_s temperatures.

Retained austenite is located either inside the M-A constituents or between the bainite/martensite laths. According to previous works, martensite is situated in the centre and retained austenite in the periphery within the M-A constituents [62]. Retained austenite has a lower dislocation density than the surrounding ferrite or lath martensite or bainite. It has also been reported that small austenite islands (0.5–1.0 μm) do not completely transform into martensite, so that the resulting M-A particle contains mainly retained austenite. Thus, the elongated M-A constituents located between bainite laths and packets consisted mostly of retained austenite [62, 63].

The precipitation of cementite from austenite can occur at temperatures between 250°C and 500°C. The carbon concentration in retained austenite is then so much decreased that a part of the retained austenite can transform to lath martensite at 400°C. Other parts of the retained austenite with higher carbon concentration may transform to plate martensite at considerably lower temperatures (200°C). Lath martensite can undergo a self tempering process, during which fine cementite is precipitated from it. And, finally, some portion of the retained austenite may remain untransformed [64].

2. 3. 2 Type and properties of M-A constituents

With respect to the shape of M-A constituents, they can be classified into two main types: elongated (or stringer like) M-A constituents with L/W > 3 and massive (or blocky) M-A constituents with L/W < 3(L: length, W: width) [66, 67]. The elongated M-A constituents being approximately 0.2 to 1 μm in width and 5 to 10 μm in length, develop preferentially between bainite and martensite laths in the ICCGHAZ [49]. The blocky M-A constituents have a diameter of about 3 to 5 μm

and are preferentially formed at the prior austenite grain boundaries or inside the grains in the ICCGHAZ. The blocky type of M-A constituents have also been observed in a necklace like structure located along prior austenite grain boundaries in a connected or nearly connected network [49]. It has been reported that blocky M-A constituents seriously deteriorate the low temperature toughness of ICCGHAZ [67]. Several works have documented that the stress concentrations in the ICCGHAZ are inhomogeneous. The dominant parameter that controls the fracture process at low temperatures is the size of the M-A constituents. Chen et al. [48] showed that high stress concentrations occur close to the interface between the matrix and the M-A constituents, and they also identified that only a small load is required to initiate microcracks in the case of large M-A constituents [49]. In order to explain the effect of M-A constituents on the toughness, Yoneda and Nakanishi et al. have suggested that the M-A constituents act as an initiation sites for cracks and promote their propagation [48, 66].

Matsuda et al. [66] report that the crack propagation energy within CGHAZ was decreased significantly while the crack initiation energy was comparable to that within the base metal if only elongated M-A constituents were formed in the CGHAZ. The elongated M-A constituents have only a small influence on the crack initiation energy. When the fraction of blocky M-A constituent increase and become larger than that of elongated M-A, both the crack initiation and the propagation energies were significantly decreased. The large tensile plastic strain region around blocky constituents extends over a wider volume than around elongated constituents. The size of M-A constituent is a controlling factor in fracture initiation, and the increase in the size of the M-A constituents lowers the critical fracture stress. Thus, the occurrence of a crack satisfying Griffith's condition is higher around the blocky M-A constituents than around the elongated ones [66].

The carbon content of M-A constituents has been claimed to be almost independent of the carbon content of the base steel. Lambert-Perlade et al. showed that for steels

containing carbon contents higher than about 0.06 wt%, the carbon content in the M-A constituents is about (0.6-1.1) wt% with an increased hardness level [44].

The strength and hardness of M-A constituents have earlier been shown to be related to their carbon content in nearly a linear manner [68]. The hardness of blocky and elongated M-A constituents has earlier been reported to be in the range of 800 to 1200HV and 600 to 800HV, respectively [64, 65]. The hardness of M-A constituents (HV_{M-A}) can be expressed as follows [65]:

$$HV_{M-A} = 575xC + 15$$

where C denotes the carbon content of the M-A constituents.

During heating, decomposition of M-A constituents has been observed to start at temperatures higher than 200 °C and to be completed around 500 °C, depending on their shape, size and chemical composition [64, 65]. Matsuda *et al.* [68] showed that the elongated M-A constituents were more easily decomposed than the blocky M-A constituents. The decomposition of the blocky M-A constituents first started at the boundary between the M-A constituents and the matrix. Hence, it can be concluded, that the retained austenite was decomposed first. After annealing for 1 h at 350 °C, the hardness of the M-A constituents was decreased to a range of 350–550 HV.

The martensite within the M-A constituents within ICCGHAZ has been reported to have two kinds of microstructure in accordance with general martensite theory:
1- Lath martensite in which laths contain a high density of dislocations. This martensite should have a higher M_s temperature, and during self-tempering, very fine needle like or dendritic cementite particles precipitate [65].
2- Plate like martensite in which laths are internally twinned. In this martensite, the cementite particles were not found neither morphologically nor by means of electron diffraction.

The residual austenite inside M-A constituent has a lower dislocation density than the surrounding ferrite. Cementite particles can be found within the austenite or on the boundary between austenite and martensite. Two types of cementite particles have been identified in M-A constituent as explained below:

1- Coarser, usually more globular cementite particles inside residual austenite or at the boundary of the retained austenite. The cementite of this type precipitates from austenite.

2- Very fine needle like or dendritic cementite particles that are precipitated inside the lath martensite during the self-tempering stage.

According to the above mentioned types, it can be concluded that the martensite within M-A constituents can have different M_s temperatures. The critical temperatures for the formation of M-A constituent are thus as follows:

- Temperature at which the austenite transforms to a constituent free from cementite participitates.
- The M_s temperature of lath marteniste.
- The M_s temperature of plate martensite.
- Temperatures below Ms giving self-tempering, i.e. precipitation of tiny cementite particles.

2. 3. 3 Factors affecting the M-A constituents

Chemical composition of steel

Earlier research has shown that many alloying elements in steel encourage the formation of M-A constituents in the HAZ. For instance, nitrogen, boron and carbon have been identified to be the strongest ones, followed by carbide forming elements like niobium, vanadium, molybdenum and chromium. The effect of manganese, nickel and copper is less significant, Fig. 5 [70-72].

Furthermore, the segregation of manganese, nickel and phosphorus during solidification and carbon, nitrogen and boron during the austenite to ferrite transformation could increase the formation of M-A constituents within the HAZ [71].

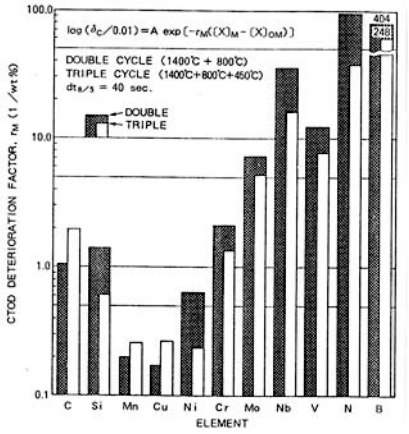

Fig. 5. *CTOD deterioration factors for alloying elements: simulated HAZ (double and triple thermal cycle) [71].*

Carbon and carbon equivalent

It is well known that the amount of M-A constituents increases with the carbon content of the steel, which has a slight influence on the carbon content of the M-A constituents. For the evaluation of the effect of the other alloying elements on the fraction of M-A constituents, the following alloy factor (AlF) was developed by Harrison and Webster (1994) [73]:

AlF = (Si + Mn)/6 + (Cr + Mo + V)/5 + (Ni + Cu)/15, 0.06< C < 0.11 %

If the AlF value is less than 0.32, the fraction of M-A constituents is rather low, normally less than 6 vol. %.

Niobium and Vanadium

Niobium and vanadium, carbide forming elements, increase the hardenability of the reaustenitized region during the second thermal cycle, which promotes the formation of M-A constituents. These elements also retard the decomposition of M-A constituents during the third thermal cycle by preventing the diffusion of carbon [70, 71].

A previous work [49] showed that a higher volume fraction of the M-A constituent as well as larger average and maximum sizes of the M-A constituents resulted from increasing the level of vanadium from 0.05 to 0.11 wt%. Therefore, a significant deterioration in toughness was observed in steels with high levels of vanadium. In addition, by adding 0.031 % Nb, the largest size of the M-A constituents and thus the lowest toughness were achieved [49].

Chromium, Molybdenum and Manganese

High levels of manganese, chromium and molybdenum contents in the steel increase the formation of M-A constituents by reducing the bainite start (B_s) temperature. Carbide forming elements such as chromium and molybdenum enhance the hardenability of the reaustenitized regions during the second welding thermal cycle, and promote the formation of M-A constituents [71].

Boron and Nitrogen

The influence of nitrogen content depends on the titanium and boron contents in the weld metal. The maximum impact toughness of the weld metal can be achieved when the titanium and nitrogen contents are 400 ppm and 40 ppm, respectively [74]. The toughness of the base plate and the weld metal can be increased by decreasing the nitrogen content of the high strength low alloy steel.

Nickel and Copper

The amount of M-A constituents can be reduced by decreasing the copper and nickel content of high strength steel, due to a decreased hardenability and upper bainite content [75]. The addition of nickel has been shown to lower the influence of excess aluminium on the mechanical properties due to an attractive force between Al-Ni in the austenite. This results in a reduction of the carbon enrichment in the austenite formed between bainitic ferrite plates during the weld cycle [75].

Aluminium and Silicon

High free aluminium content in steels has been shown to promote the formation of M-A constituents by preventing carbon diffusion and precipitation of carbides from the high carbon austenite [71]. Silicon has been found to enhance the formation of M-A constituents and twinned martensite during the intercritical heat cycle. High silicon contents in steels increase the formation of M-A constituents by retarding the precipitation of cementite [51, 71].

Cooling rate

The influence of the intercritical thermal cycle cooling rate on the volume fraction of M-A constituents has not been fully established. The formation of M-A constituents in the ICCGHAZ depends on the microstructure in the CGHAZ, which in turn depends on the cooling rate. In high strength steels the volume fraction of M-A constituents increases strongly when $\Delta t_{8/5}$ becomes longer than 10–20s. Then the volume fraction of M-A constituents decreases with increasing cooling time due to the decomposition of M-A constituents into carbides in ferrite. This decomposition begins at $\Delta t_{8/5}$= 50 s [71].

The relation between absorbed charpy V energy, hardness of the CGHAZ and the cooling time, $\Delta t_{8/5}$, during weld simulation of X70 pipeline steel, is presented in Fig.

6. It is seen that the absorbed energy is at a maximum at $\Delta t_{8/5}$=8s. The absorbed energy decreases when $\Delta t_{8/5}$ is shorter or longer than 8s. It can also be seen that the hardness decreases with increasing cooling time. Therefore, choosing suitable heat input during welding is important in order to obtain better toughness and suitable hardness, which is beneficial to prevent hydrogen assisted cracking. For high peak temperature, most particles, such as V(C, N), Nb(C, N) dissolve into the steel, leading to austenite grain growth and reduced toughness with increasing cooling time. The reason for the high toughness at $\Delta t_{8/5}$=8s is that the microstructure for this cooling time is composed of a large amount of granular bainite and retained austenite films which possess high toughness. In addition, the microstructure and the proportion, size and distribution of M-A constituents also directly affect the toughness of the granular bainite [76].

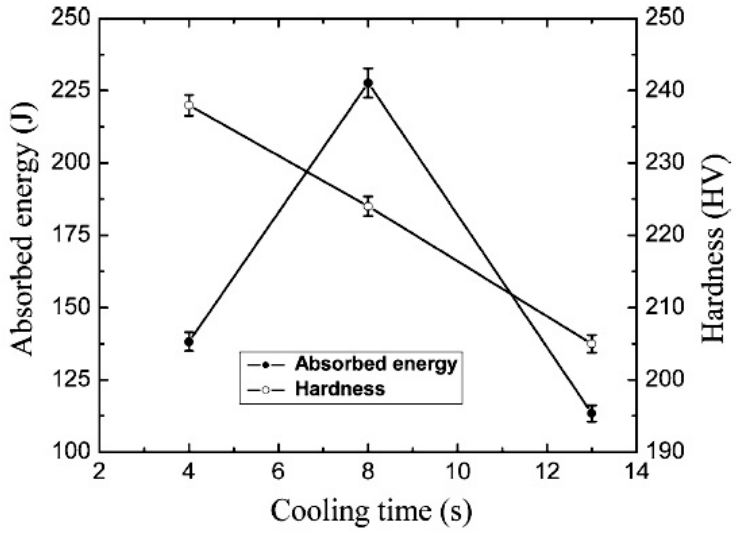

Fig. 6. *Variation of charpy V absorbed energy and HAZ hardness with cooling time during weld simulation of CGHAZ [76].*

Peak temperature

The peak temperature of the thermal cycle of CGHAZ has been shown to have only a slight influence on the volume fraction of M-A constituents, but it probably has a significant influence on their distribution. The peak temperature of the second intercritical thermal cycle has been found to have a significant influence on the volume fraction of M-A constituents in the ICCGHAZ. The volume fraction of M-A constituents was enhanced by increasing the temperature of the second cycle from 660°C to 800°C and reached a maximum value between 750°C to 770°C. During the second thermal cycle between A_{c1} and A_{c3}, the first nucleation and growth of austenite begins from carbides and pre-existing M-A constituents at the prior austenite grain boundaries. In the cooling stage, M-A constituents first form along the prior austenite grain boundaries and then at the interfaces between martensite and ferrite laths [4, 62, 71].

2. 4. Effect of M-A constituents on the fracture mechanism

Earlier investigations have shown that M-A constituents can initiate both ductile and brittle fracture. Debonding of M-A constituents from the surrounding matrix and cracking of M-A constituents are generally reported for initiation events of fracture. A crack can nucleate at three positions: inside M-A constituents, in the matrix near a M-A constituent, and at or close to the interface between the matrix and the M-A constituents. The generally accepted mechanism for crack initiation caused by M-A constituents is based on the concentration and triaxiality of internal stresses in regions close to the M-A constituents and in the matrix/M-A interfaces. The phenomenon is explained as follows:

− The volume expansion due to the transformation of austenite into M-A constituents may enhance the elastic and plastic strain at the interface and inside the matrix by increasing the transformation induced stresses [4, 47].

− The higher hardness value of M-A constituents with respect to the matrix (hardness of 800–1200 HV for blocky M-A constituents and about 300 HV for matrix) can cause dislocation pile-ups in front of the M-A constituents during loading, exerting a high stress concentration on it that initiates a crack [4, 48].
− M-A constituents crack readily as a brittle phase and initiate a microcrack. The stringer M-A constituents have been shown to crack instantly, but the individual blocky M-A constituents do so quite seldom [47].
− A difference in elastic straining between the M-A constituents and the matrix during loading and further strain partitioning between the M-A constituents and the matrix cause strain accumulation only in the matrix [4].
− Connected or nearly connected M-A constituents along prior austenite grain boundaries enables an array of debonded M-A constituents to produce a constrained region of high stress fields between M-A constituents, where a cleavage crack may be formed [47, 57].
− A microcrack may form at the M-A/matrix interface through interfacial decohesion [47].
− Carbon segregation at the interface between a M-A constituent and the matrix reduces the interfacial energy [47, 57].

The role of M-A constituents in crack propagation is not clear. On one hand, M-A constituents can promote brittle fracture by re-initiating cleavage crack, either in the cracked M-A constituents or generation of small cracks at the M-A constituent/matrix interface. On the other hand, M-A constituents can cause kinks in the fracture surface and thus hinder fracture propagation [64, 65].

2. 4. 1 Ductile fracture

During heavy deformation at moderate temperatures, the matrix can yield easily, thereby increasing the stress concentration at the M-A constituent/matrix interface. This high stress concentration causes the M-A constituents to crack or debond. With

an increasing strain level, cracks generate voids which grow to become deep holes. Then a main crack forms and propagates by lateral growth, and the coalescence of deep holes due to internal necking leads to rupture of the specimen [47, 48, 64, 65, 77]. It has also been documented that microvoids can form on M-A constituents and on M-A/matrix interfaces,and they form more easily on interfaces of stringer M-A constituents orientated 40–50 degrees to the tensile axis than from individual blocky M-A constituents, or from stringers oriented parallel to the tensile axis, Fig. 7 [60].

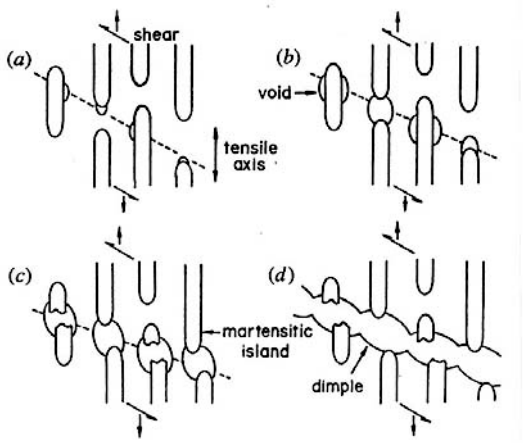

Fig. 7. *Schematic illustration of the ductile fracture mechanism in coarse grained HAZ (CGHAZ) of a HSLA steel weld. [60].*

2. 4. 2 Brittle fracture

The initiation mechanism of a brittle fracture has been found to be similar to that of a ductile fracture. In the case of cleavage fracture, the microvoids formed at M-A/matrix interfaces as a result of triaxial stresses interlink and propagate as a cleavage crack, rapidly reaching prior austenite grain boundaries, Fig. 8 [48, 60].

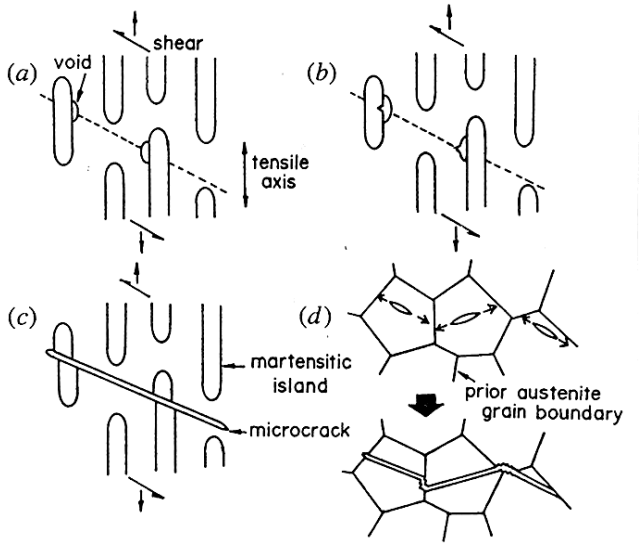

Fig. 8. *Schematic illustration of the cleavage fracture mechanism in the CGHAZ of a HSLA steel weld [60].*

A significant reduction in toughness has been found when blocky M-A constituents form in a connected or nearly connected network along the prior austenite grain boundaries. The stress concentration will be magnified because the transformation-induced stress fields overlap. Therefore, two closely spaced blocky M-A constituents produce a constrained region with a high stress field that forms a small crack that initiates local cleavage, Fig. 9 [48, 57].

Lambert et al. [63, 78] have studied the effect of temperature on the mechanism of cleavage fracture. At very low temperatures (below -150°C), cleavage fracture was claimed to be nucleation controlled, but at higher temperatures, the nucleation of microcracks took place in M-A constituents (or at M-A constituent/matrix interfaces) followed by their propagation into the surrounding matrix.

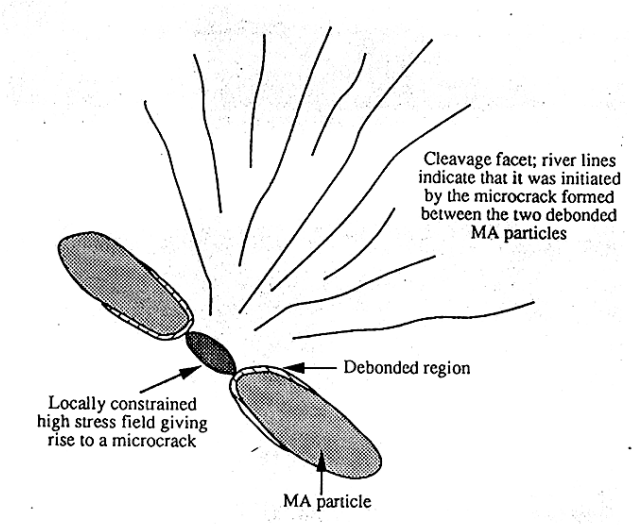

Fig. 9. *Schematic diagram showing proposed mechanism by which connected or nearly connected M-A constituents initiate a cleavage fracture [57].*

Chen et al. [48] observed high stress concentrations at the boundaries between α-Fe and M-A constituents. At moderate and high temperatures, these stresses made the boundaries crack or debond. With increasing strain, cracks grew to voids that developed into deep holes. At lower temperatures, however, stiffer blocky M-A constituents gave rise to high concentrations of triaxiality of stresses at points near the boundary on the ferrite side, and causing initiation of a cleavage crack. The most important issue is the size of the M-A; the larger the size, the smaller is the load that is required to initiate a new crack [61].

A crack arrest took place at high angle boundaries (misorientations over 40°), while lower angle boundaries (misorientations around 20°) were found to induce only a slight deviation in the crack path. In previous works, M-A constituents were shown to assist the propagation of cleavage fracture due to the fact that a cleavage fracture preferentially propagates along the interface between the M-A constituents and the matrix [64, 65].

In summary, four possible fracture mechanisms have been proposed in the literature to explain cleavage initiated by M-A constituents, and these are shown schematically in Fig. 10 [49, 79 and 80]:

(1) The M-A constituent is a brittle phase and cracks readily. This microcrack initiates cleavage in the ferrite matrix.

Previous works have shown that M-A constituents can act as initiation sites for cracks and also promote their propagation [44, 48]. At low temperatures, the blocky M-A constituents increase the matrix stresses close to the interface between the M-A constituents and the matrix, and may cause cleavage crack initiation [64]. Stringer type M-A constituents have been shown to crack readily and provide no effective obstacle to crack propagation [56].

(2) Transformation-induced residual tensile stresses are produced in the surrounding ferrite matrix, assisting cleavage fracture.

Austenite forms at prior austenite grain boundaries and transforms to M-A constituents during cooling. The volume expansion related to this transformation results in elastic and plastic stress concentrations in the surrounding matrix, assisting cleavage fracture. In the case of the closely spaced blocky M-A constituents, the stress and strain concentrations will be magnified because the transformation induced stress fields overlap.

(3) The M-A has higher hardness than the surrounding ferrite and causes a stress concentration in the neighbouring ferrite matrix. This stress concentration assists cleavage fracture.

The hardness of a M-A constituent is significantly higher than that of the surrounding matrix, and during deformation, the stress concentration increases due to this hardness difference. During loading, the matrix will start to deform plastically, and an internal stress can be generated in the matrix close to the M-A constituent [48, 49, 80]. A high stress will develop across the interface and may cause the M-A constituent to debond from the matrix. In addition, it has been

suggested that the M-A constituent/matrix interface may be weakened by carbon segregation [68].

(4) A microcrack that is formed at the M-A/matrix interface through interface decohesion can initiate fracture that propagates either in a brittle manner or by interlinkage with other debonded regions.

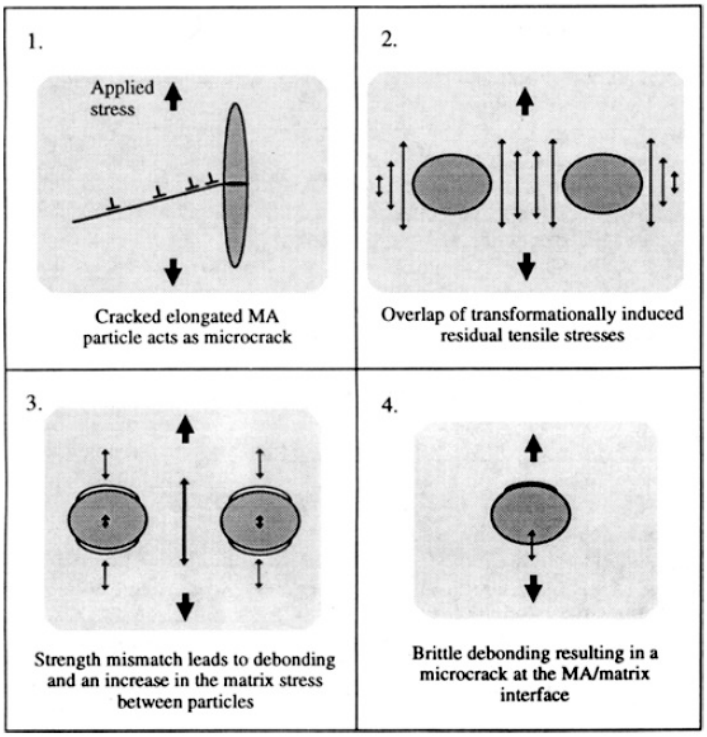

Fig. 10. *Schematic representation of the four proposed initiation mechanisms [80].*

In addition to the four initiation mechanisms illustrated in Fig. 10, M-A constituents contribute to the brittleness of the weld by re-initiating cleavage fracture (i. e. forming new facet initiation points ahead of the advancing crack tip). The re-initiated cracks were found to occur on either side of the M-A constituent due to high stress concentrations in the surrounding ferrite matrix. Also cracked M-A constituents have been found to be re-initiation sites [64].

2. 4. 3. Factors affecting the critical fracture stress

The main factors affecting the critical fracture stress (σ_f) are prior austenite grain size and presence of M-A constituents. Fig. 11 shows that the critical fracture stress versus grain size and amount of M-A constituents in the CGHAZ. It can be seen that the critical fracture stress is reduced by increasing the amount of M-A constituents and grain size.

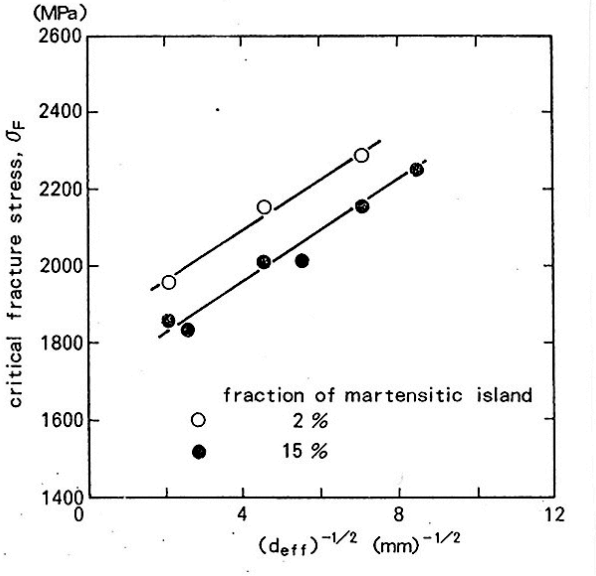

Fig. 11. *Change of critical fracture stress with effective grain size and amount of M-A constituents: simulated HAZ (Tp1 =900–1400 ℃, Tp2 =800 ℃) [70].*

Although σ_f decreased with increasing effective grain size and volume fraction of M-A constituents, the influence of the grain size was relatively small. The influence of M-A constituents on σ_f is expected to be significant. When CTOD values decrease with decreasing σ_f or increasing yield strength a decrease in the CTOD value with increasing peak temperature is mainly due to the increase in yield strength rather than due to an increase in the effective grain size [70].

2. 4. 4 Toughness improvement mechanisms

The toughness of the ICCGHAZ is strongly influenced by metallurgical factors such as the amount, type and distribution of M-A constituents and the microstructure of the matrix. The characteristics of M-A constituents (amount, hardness and size) have been found to be strongly correlated to the peak temperature and cooling rate of the previous pass, which have a great influence on the prior austenite grain size of the previous pass. The amount of M-A constituents has been considered a dominant factor influencing the toughness of the ICCGHAZ only when the cooling time is short. When the cooling time increases, the hardness difference between M-A constituents and the softened matrix have been found to be dominant, Fig. 12.

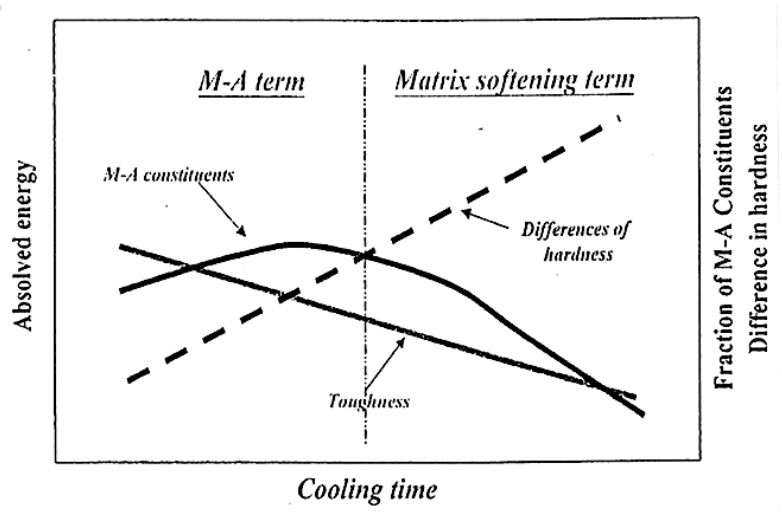

Fig. 12. *Effect on toughness of M-A constituents and difference in hardness [82].*

For short cooling times, the toughness deterioration mechanism caused by M-A constituents is based on high stress fields between two M-A constituents at the prior austenite grain boundary followed by the formation of microvoids and their growth into the matrix [57, 60]. For longer cooling times, microvoids can nucleate around the hard and coarse M-A constituents or carbides after their separation from the prior austenite grain boundaries, lath boundaries or the softer matrix [81].

In recent studies, the amount, type and distribution of M-A constituents and the packet size of bainite or the dimension of ferrite side plates have been found to be the main factors affecting the toughness of the HAZ of high strength low alloy steels [63]. High carbon, blocky martensite located at the prior austenite grain boundaries was claimed to be more deleterious than retained austenite located between the laths of bainite packets or grains of ferrite side plates. For both kinds of M-A constituents, martensite have been found to be located at the centre and retained austenite at the periphery because of a chemical and/or mechanical stabilisation mechanism [63].

Formation of acicular ferrite instead of bainite in the CGHAZ will improve the toughness of the ICCGHAZ, because an acicular ferrite microstructure will lead to a more homogeneous distributing of M-A constituents than a bainite microstructure. The toughness improvement is based on both fracture initiation and fracture propagation. During crack initiation, small homogenously distributed M-A constituents can distribute the loading and transformation stresses more evenly than the blocky M-A constituents at prior austenite grain boundaries or stringer M-A constituents between large bainite packets or ferrite grains do and by that retard the nucleation of microvoids. The intragranularly nucleated acicular ferritic microstructure can retard crack propagation more effectively than a coarse bainitic-ferritic microstructure due to numerous high angle boundaries between acicular ferrite laths.

Crystallographic grains and lath packets define neighbouring units with constant crystallographic orientation within the same unit. In body centred cubic (bcc) iron like acicular ferrite, a cleavage fracture typically propagates along {100} planes, which means that the crack must be deflected at high angle grain or packet boundaries as shown in Figure 13. Gourgues et al. [83] have found that in acicular ferrite, nearly all boundaries between acicular ferrite laths were high angle boundaries with misorientation angles greater than 45°.

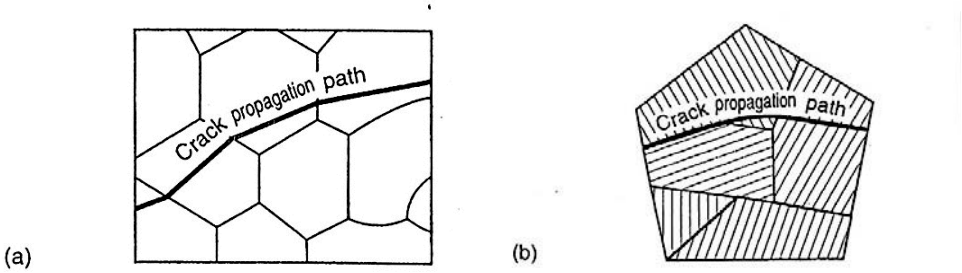

Fig. 13. *Schematic illustration showing crack deflection at interfaces: a) high angle ferrite grain boundaries and b) high angle packet boundaries (bainitic microstructure) [84].*

2. 5. Ductile to Brittle Transition Behaviour

The variation of fracture behaviour with temperature has been traditionally characterized by a ductile to brittle transition curves, which is characterized by a sudden and dramatic drop in the energy absorbed by a metal subjected to impact loading. It is well known that in body centred cubic (bcc) metals such as low carbon steel, toughness and ductility decrease with decreasing temperature, and the fracture mode changes from ductile at high temperature to brittle at low temperature [42]. As temperature decreases, the ability of a metal to absorb impact energy decreases. The fracture energy transition temperature range might not be narrow enough to be able to identify a unique transition temperature. This is often the case for steels. The width of this range varies with the alloy. Fracture in this range is a mixture of ductile and brittle modes of failure. Often, criteria other than the energy transition are used to define the transition temperature [8].

As far as the fracture criteria for various modes of fracture are concerned, it is commonly assumed that brittle fracture occurs when a critical fracture stress is achieved ahead of the crack tip (stress controlled fracture), and that ductile fracture occurs when a critical fracture strain is obtained ahead of the crack tip (strain controlled fracture) [85].

An examination of a fracture surface will reveal whether the fracture occurred by ductile or brittle processes. Examination with an SEM clearly reveals the cleavage appearance, river lines and other planar microcrack characteristics of brittle fracture. Brittle fracture can occur intergranularly or transgranularly. Ductile fracture is usually transgranular, and its fracture surfaces show a significant amount of plastic deformation between nearly spherical microvoids.

The parameters that affect this transition, are *e.g.* the chemical composition of the steel, its microstructure (grain size, phase composition, morphology of pearlite/ cementite, slag particles like MnS, etc.), crystallographic texture, aging, cold deformation, surface notches, geometrical conditions, loading history, and the occurrence of deformation twinning (nucleating cleavage) prior to final fracture. Moreover, welding introduces new chemical compositions (filler metal) and changes in the microstructure (HAZ) [8].

2. 5. 1 Testing of ductile to brittle transition temperature

Determination of the ductile to brittle transition temperatures is mostly done by the standard Charpy V-notch test, which has become the common quality control toughness test for steel products because of its fast and simple application. However, a relatively large notch root radius (0.25 mm) in the Charpy V specimens has a limited capability to take micromechanical features into consideration and does not contribute to the increase in the stress-strain state necessary for formation of microcracks as effectively as CTOD specimens with a smaller root radius [81].

2. 5. 2 Crack tip opening displacement transition temperatures

The idea of the CTOD test is to develop a ductile crack into the critical length for cleavage fracture. The CTOD test with through thickness fatigue notched specimens has been regarded as being too conservative due to the fact that in many

applications, cracks are nucleated at the surface. Moreover, the CTOD results for small scale samples from simulated heat affected zones are even more conservative due to the shape effect.

The sharp fatigue pre-crack tip of CTOD specimens promotes the sensitivity of CTOD specimens to M-A constituents compared to Charpy V-notch specimens. Thus, a large scattering is characteristic of the CTOD test results, particularly in the ductile to brittle transition temperature range [70, 81]. It has been observed in numerous studies that M-A constituents have a significant role in the deterioration of toughness by decreasing crack initiation and propagation energies [71-73].

Crack propagation depends on the type of loading. Under the static loading of bainitic or martensitic CTOD samples, a crack that propagates in a packet boundary may continue to propagate in another packet along a certain plane that possesses a low resistance to fracture. Since CTOD tests from welded joints are very difficult and expensive to carry out, the correlations between CTOD and Charpy V impact tests have been conducted and used in numerous design codes. The correlations are based on the parabolic relationship between the results of Charpy V and CTOD tests [56].

2. 6 Electron backscatter diffraction (EBSD) Technique

2. 6. 1 Introduction

The electron backscatter diffraction (EBSD) technique in the scanning electron microscope is a powerful tool for characterizing important crystallographic features of a wide variety of materials. This technique has been developed for a range of applications including phase identification, grain and surface crystallography and cystallographic plane and orientation of fracture surfaces [86, 87]. But complex microstructures are difficult to handle due to problems in obtaining reliable EBSD

data from samples containing more than one phase or exhibiting a high intristic dislocation density.

The EBSD pattern consists of a set of Kikuchi lines which are characteristic of the sample crystal structure and orientation. An EBSD pattern is generated by illuminating a steeply tilted crystalline sample in the SEM with a stationary focused electron beam. The sample is tilted to about 70º to obtain diffraction patterns of sufficient intensity, and backscattered electrons are captured on a transparent phosphor screen that is placed parallel with the incident electron beam and the tilt axis of the stage [88]. A typical arrangement of the sample with respect to the electron beam and the phosphor screen is shown in Fig. 14.

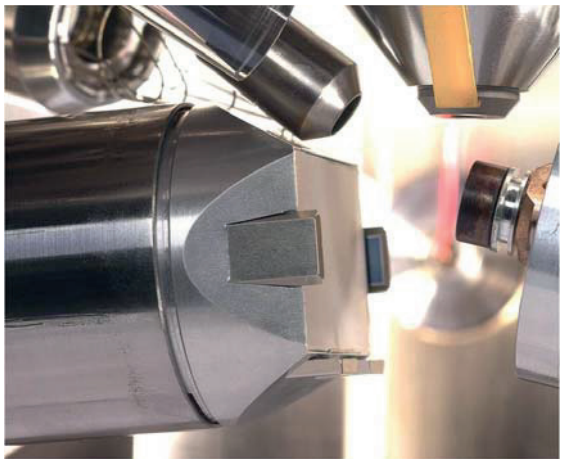

Fig. 14. *Micrograph of typical EBSD hardware inside the SEM chamber (www.ebsd.com).*

The crystallographic indexing of the patterns is determined by specifying two sets of reference systems, or more exactly, a sample and a crystal coordinates system. The crystallographic orientation for a given point at the specimen surface is calculated as the misalignment between these two coordinate systems, i.e. the rotation required to make the two systems coincide [88]. The axes in the sample reference system usually refer to directions that are related to the processing of the material, such as the rolling direction (RD), the transverse direction (TD) and the normal direction (ND) of a rolled product.

The crystallographic orientations of individual crystals are commonly given by the Euler angles or Miller indices convention. The Euler angles are three sequential rotations that convert the sample reference system to the coordinate system of the unit cell. There are various conventions for expressing the Euler angles, depending on the axes about which the rotations are conducted [94]. The stepwise rotations defining the Bunge notation, which is by far the most widely used technique, are presented in Fig. 15. According to the Bunge notation, the crystallographic orientation of a crystal is specified by the three Euler angles φ_1, Φ and φ_2. In the first sequence, the crystal is rotated the angle φ_1 about the ND axis. The following step involves the rotation Φ about the new RD axis. Finally, the third rotation is the angle of φ_2 about the new axis ND.

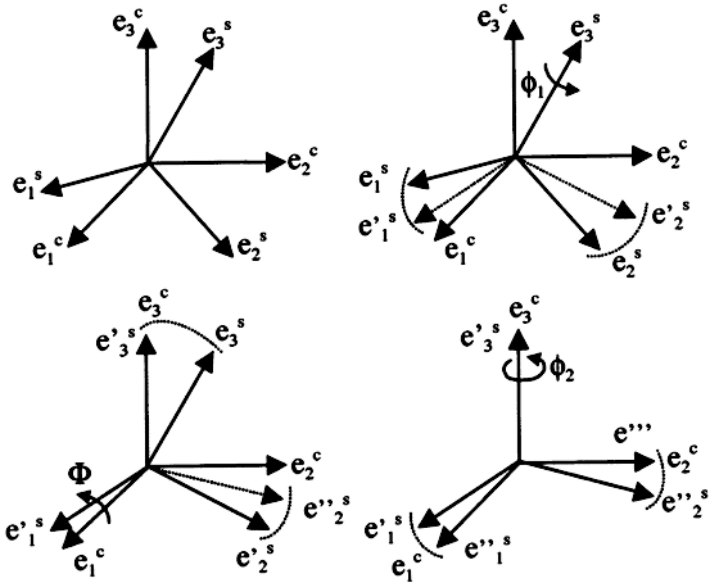

Fig. 15. *Sequential rotations carried out to express the Euler angles in terms of the Bunge notation [94].*

When using the Miller indices notation, the crystallographic orientation is expressed in terms of planes and directions in a crystal [88]. The orientation is generally written as (hkl)[uvw], where (hkl) specifies the crystal plane perpendicular to the normal of the sample and [uvw] the crystal direction parallel to sample axis defined

by the operator. The use of Miller indices is a convenient way to denote the crystallographic orientation because it relates planes and directions in the crystal with the sample reference system.

2. 6. 2 Application of EBSD in fracture surface studies

The application of electron backscatter diffraction to fracture studies has provided a new method for investigating the crystallography of fracture surfaces [87]. A fracture surface will possess several different surface facets and therefore also several different facet normals. From a given facet the electrons will be diffracted in various directions depending on the crystallographic orientation of the grain that forms the facet, resulting in an EBSD pattern that is defined by the crystallographic orientation of that grain. By indexing the pattern, the crystallographic indices of the facet, e.g. a cleavage plane, can be identified. Either the crystallographic orientation can be determined directly from the fracture surface, or it can be determined indirectly from a metallographically prepared surface perpendicular to and adjacent to the fracture surface, Fig. 16 [87, 89]. A two-dimensional analysis technique has been developed in which EBSD measured crystal orientations are combined with secondary electron imaging to obtain the trace of the crack facet with the section plane of the indirect method [90, 91].

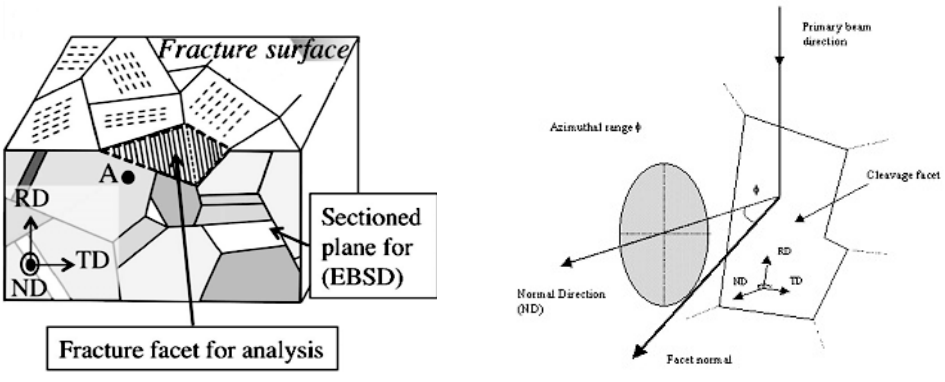

(a) *(b)*

Fig. 16. *Schematic illustration of EBSD technique, (a) Indirect and (b) Direct method.*

2. 6. 3 Application of EBSD in Slip System Activity Analyses

Dislocation glide during plastic deformation leads to the formation of slip markings on the metal surface. It is commonly accepted that dislocation glide takes place on slip systems being favourably oriented with respect to the tensile direction, i.e. on those systems having the highest Schmid factor [81, 93]. A slip system is supposed to be activated when associated slip markings are observed at the metal surface [94]. Therefore, by calculating the Schmid factors of all possible slip systems the slip activity within the different grains (12 possible slip systems within FCC grains, i.e. {111} <110>; 48 slip systems within BCC grains i.e. {110} <111>, {112} <111> and {123} <111>), during plastic deformation can be evaluated [95]. The Schmid factors for a given grain can be calculated by using the Euler angles determined by the EBSD technique applied on a pre-polished surface after a deformation test. The orientation data of the grains are stored as Euler angles ($\varphi 1$, ϕ, $\varphi 2$), and the transverse (TD) direction in the standard pole figures is usually set equal to the specimen tensile axis.

3. Experimental procedure

3. 1 Material

A commercial grade of API X80 pipeline steel which was produced by the JFE steel corporation in Japan was selected for the present PhD work. The outer diameter and the wall thickness of the pipe were 508mm (20 inches) and 14mm, respectively. The chemical composition is given in Table 1 and was measured by the Molab AS in Norway.

Table 1 Chemical Composition of the steel (mass %) [1]

C	Si	Mn	P	S	Cr	Cu	Ni	Mo
0.06	0.08	1.79	0.012	0.004	0.12	0.28	0.16	0.15

[1] With 0.044%Nb, 0.013%Ti and 0.028%Al.

3. 2 Weld Simulation

The relationship between the brittle to ductile transition temperature and the microstructure in the coarse-grained heat affected zone, CGHAZ, and the intercritically reheated coarse-grained heat affected zone, ICCGHAZ was studied by applying a Smitweld, weld simulator using resistance heating for producing the HAZ microstructures. To simulate CGHAZ and ICCGHAZ microstructures, specimens of dimensions 11x11x100 mm^3 were cut with the longest dimension along the rolling direction of the pipe and subjected to single and double cycle HAZ simulation, Fig. 1. During the thermal cycle, the specimen was resistance heated to 1350°C by a rate of 150°C/s, followed by cooling at a rate corresponding to a cooling time between 800°C and 500°C ($\Delta t_{8/5}$) of 15 seconds. The second heating cycle had a peak temperature, T_{p2}, of 780°C, and the cooling rate was the same as during the first cycle, Table. 2.

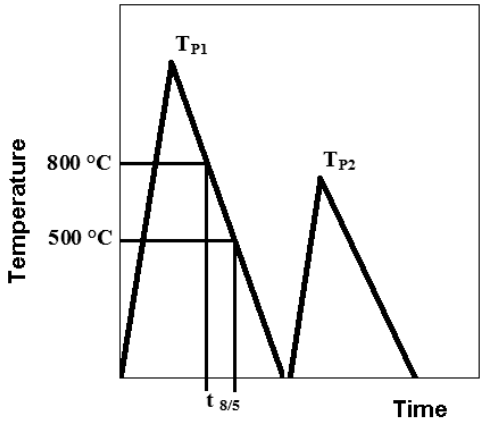

Fig. 1. *Weld Thermal Simulation.*

Table 2 The thermal cycle for the simulation of HAZ

	CGHAZ	**ICCGHAZ**
First peak T_{P1} (°C)	1350	1350
Holding time at 1350°C	1s	1s
Cooling time $\Delta t_{8/5}$	15s	15s
Second peak T_{p2} (°C)	-	780
Holding time at peak	-	1s
Cooling time $\Delta t_{8/5}$	-	15s

3. 3 Mechanical Testing

After the HAZ simulation, Crack Tip Opening Displacement (CTOD) specimens were machined with a 5 mm deep through width notch cut into the samples and subjected to CTOD testing at 0,-30,-60 and -90 ºC, Fig. 2. CTOD testing was performed inside a temperature chamber according to standard BS7448 part 1. Thermocouples were welded directly on to the backside of the specimens, and the temperature was allowed to stabilize at the target test temperature for 10 minutes before executing the test. In addition, stress-strain curves of HAZ simulated samples were obtained by tensile testing of smooth round bar specimens at corresponding test temperatures. The tensile testing was carried out using a universal 30 kN electromechanical testing machine, Zwick/Roell Z030. An

extensometer was used during the tensile test, and it was located within the heat affected zone region, 15mm between the clips. The tensile tests were carried out using a strain rate of $3x10^{-4}$ s^{-1} at 0,-30,-60 and -90 ºC, and they were performed inside a temperature chamber cooled by nitrogen gas in a similar manner as for the CTOD testing.

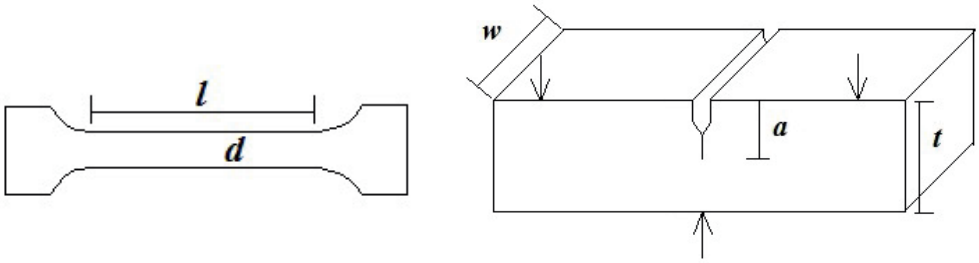

(a) d=4mm, l= 20mm *(b) t=w=10mm, a/t=0.5*

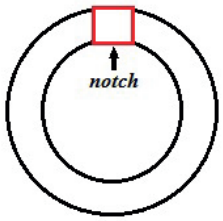

(c)

Fig. 2. *Dimensions of a) tensile, b) CTOD testing specimens, and c) orientation of notch respect to the pipe.*

In order to identify the slip system activity at low temperatures, slip markings were formed on the polished specimen surfaces (mechanically ground and polished down to 1μm and finally polished with a colloidal silica suspension, OPS suspension, for 20 minutes) by applying low cycle three point bending fatigue test. The fatigue tests were also performed at temperatures down to -90 ºC (0, -30, -60 and -90 ºC) under load control with a total stress amplitude below the yield stress (L_{max}=0.95σ_y and R ratio of 0.1). After 2000 cycles the tests were stopped. The testing was carried out using a universal 30 kN electromechanical testing machine, Zwick/Roell Z030. The features of the slip markings on the polished specimen surfaces after the fatigue tests

were examined light optically with a Leica MEF4M microscope, scanning electron microscope and scanning probe microscope. A Zeiss Supra 55VP, LVFESEM, (operated at 20kV acceleration voltage, 82µA probe current and 30µm aperture size) was used to observe slip markings and microstructure in the polished surfaces. EBSD analysis was done close to the slip markings with a TSL (TexSem Laboratories) EBSD system interfaced with the SEM.

3. 4 Characterization

The HAZ microstructures were examined by optical microscopy, Leica MEF4M attached with JENOPTIK (laser optik system) CCD camera, and by scanning electron microscopy, Zeiss Supra 55VP. Samples for light microscopy were mechanically prepared by conventional grinding and polishing techniques and etched by a Lepera solution (mixture of 4% Picral and 1gr Sodium Thiosulphate ($Na_2S_2O_3$) in 100ml distilled water in a 1:1 ratio) [96], which make the M-A constituents appear white. Fig. 3 shows a photograph of the Zeiss Supra 55 VP which is low vaccum field emission SEM (LVFESEM). It was used to observe the fracture surfaces and HAZ microstructures, operated at 20kV, 82µA and 30µm aperture size.

Fig. 3. *Photograph showing the Zeiss Supra 55 VP SEM.*

The Zeiss SEMs can operate with acceleration voltages in the range from 100 V to 30 kV. They use the Schottkey field emission source, which combines the high stability and low beam noise of thermal emitters and the high brightness and low energy spread of the cold field emitters, but at a much higher probe current. These characteristics are very convenient for EBSD measurements. Moreover, the applied SEMs are equipped with various imaging and characterization capabilities, including EBSD, energy dispersive X-ray spectrometers (EDS), secondary electron (SE) and backscattered electron (BE) detecors. In addition, they have a large vacuum chamber so large specimens can be investigated. Finally, the microscopes are equipped with a very user-friendly Windows based SmartSEM control software that can be controlled by mouse, keyboard and a dedicated joystick.

In order to obtain information about the chemical composition of second phase particles, EDS spectroscopy was performed with an EDAX Genesis spectrometer interfaced with the SEM microscope. In addition, the carbon concentration of the blocky M-A constituents was studied by wavelength dispersive spectroscopy (WDS) in a Jeol JXA-8500 electron probe micro-analyzer (EPMA), operated in spot mode at 10 kV accelerating voltage and 50nA probe current. An LDE6H crystal was used for this measurement.

Scanning probe microscope analysis was carried out with a Hysitron TI 750 UbiTM with a performechTM control unit scanning Nanoindentation system (operated at 0.5 Hz scanning rate, 16 μm/Sec tip velocity and 2μN set point). The size of the investigated region was 12x12 μm^2.

The Hysitron Triboscan is a quantitative nanoindentation system with ability to image the surface before and after indentation. The nanoindenter is an attachment (accessory) to a scanning probe microscope and does not utilize the piezo feedback or the Atomic Force Microscope (AFM) cantilever to perform its tests. The Scanning Probe Microscope (SPM) software is used to interpret the voltage signal from the transducer, and the microscope piezos enable displacement control when

imaging. The resolution of the image is not as good as those obtained with an Atomic Force Microscope (AFM) or Scanning Tunneling Microscopy (STM) tip due to the bluntness of the indenter. It does give sufficient resolution to identify desired surface features and to choose optimal areas to indent. The system has a depth resolution of 0.2 nm and can apply indentation loads as high as 8.0 mN with a resolution of 0.1 μN.

3. 5 EBSD Analysis

The EBSD analysis presented in this PhD thesis was carried out using systems that are based on on-line EBSD data collection. The on-line EBSD measurements were performed using the EDAX/TSL 4.5 and 5.2 software versions. Both softwares versions are composed of two separate programs, one for automatic collection and indexing of Kikuchi patterns and storing of the calculated crystallographic orientations, and one for the data analysis following the EBSD measurements. Furthermore, the on-line measurements were carried out using the Nordif CD 200 EBSD detector equipped with a Hamamatsu digital CCD camera. This camera is designed with the ability to vary the number of pixels constituting an image to vary the sensitivity, and hence the data collection speed.

a) EBSD analysis of fracture surfaces with 3D SEM studies

EBSD specimens were prepared by cutting length sections normal to the fracture surface close to the notch tip, Fig. 4, so that EBSD could be made near the fracture surface with a TSL EBSD system interfaced with the SEM.

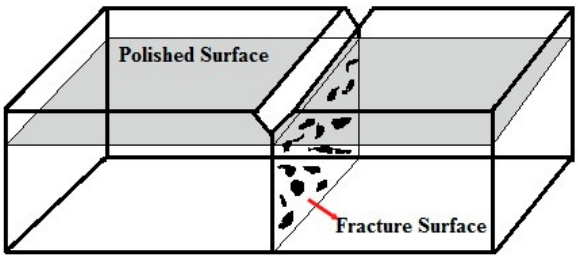

Fig.4. *Schematic scetch showing the position from which EBSD samples were taken.*

These length sections were mechanically ground and polished down to 1μm and finally polished with a colloidal silica suspension (OPS suspension) for 20 minutes in order to remove any deformation from the mechanical grinding and polishing.

b) EBSD and SPM analysis of slip system activity in fatigue tested specimens

After the HAZ simulation, for further investigations by electron backscatter diffraction and scanning probe microscopy, a perfectly polished flat surface is required in order to observe very small reliefs (induced by deformation) in the SPM images, and to obtain a good quality of the EBSD patterns. As a consequence, the sample preparation contained many stages. The specimens were ground and mechanically polished down to 1μm. For the final polishing, the samples were polished with colloidal silica suspension (OPS suspension) for 20 minutes. The fine polishing was done before the fatigue tests.

3. 6 3D SEM analysis

Computer assisted 3D-imaging was carried out by using the Mex software (Alicona imaging). During 3D imaging, images of a fracture surface were taken at minimum two different tilt angles, and they were combined to produce a three-dimensional reconstruction of the fracture surface. This method was applied to measure the angles between cleavage facets and the adjacent polished surface, and then this

measurement was applied together with EBSD diffraction data to determine the crystallographic planes of the facets.

3. 7 TEM Investigation

For detailed analysis of the microstructure, Transmission Electron Microscopy (TEM) was carried out on thin samples from the ICCGHAZ region. The thin samples were prepared from the fractured CTOD specimens by using the Focus Ion Beam (FIB) technique, applying a HELIOS NANOLAB 600 from FEI. The FIB thinning process of the sample included two steps: (i) Thinning with an ion beam (30 kV), starting with a high current, 460 pA, that successively was reduced to 50 pA. (ii) Final thinning with a box pattern with ions at 5 kV and 16 pA (approximately 1.5 minutes at each side) to eliminate all damage produced by the first step. The TEM observations were performed in a conventional JEOL-JEM 2010 microscope at 200 kV acceleration voltage.

3. 8 Hardness Measurements

The hardness of the M-A constituents and the neighbouring base metal was measured by a nanoindentation technique applying a Hysitron TI 750 UbiTM instrument with a performechTM control unit scanning nanoindentation system. The measurements were performed within the HAZ region (80μm x 80μm) of the samples after polishing and etching by Lepera solution; the step size being 4μm.

Vickers microhardness measurements were also done by using 5gf (gram force) load in a Leica VMHTMOT instrument. In both cases the indents were small enough (approximately 4μm in diameter in the Leica) to predominantly sample either a M-A constituent or the matrix.

4. Overview of Results

4. 1 Paper 1

Investigation of the mechanism of cleavage fracture initiation in the intercritically coarse grained heat affected zone of an HSLA steel.

In this work, a systematic investigation was performed to identify the brittle fracture crack initiation mechanism in the ICCGHAZ of the arctic steel X80. The main purpose of the work is to reveal the mechanism by which M-A constituents deteriorate the HAZ toughness. By analyzing the fracture mechanisms, the effect of M-A constituents on the fracture toughness has been investigated.

The microstructures of ICCGHAZ were examined by optical microscopy and by scanning electron microscopy. Two main types of M-A constituents were identified as illustrated in Fig. 1. It can be seen that blocky M-A constituents are located at prior austenite grain boundaries or inside the grains, while elongated M-A stringers have formed between bainite or martensite laths.

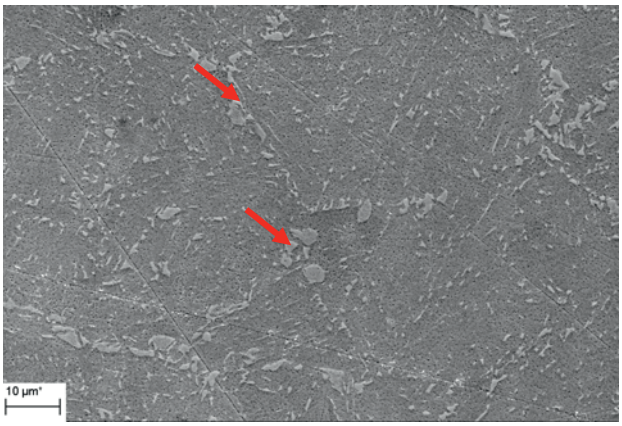

(a)

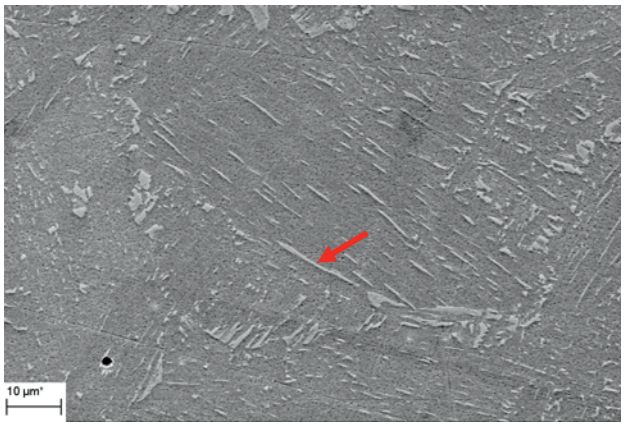

(b)

Fig. 1. *SEM micrographs from weld simulated ICCGHAZ region, a) blocky and b) elongated M-A constituent, indicated by arrows.*

The hardness of the M-A constituents was measured by the Vickers microhardness method and by nanomechanical testing. It was shown that the hardness of the M-A constituents was significantly higher than that of the neighbouring matrix. The hardness of M-A constituents was in the range of 600-1000 Hv in this investigation. The carbon content of a number of M-A constituent was measured by EPMA line scan analysis, through the particles and into the surrounding matrix, one example is given in Fig. 2. It can be seen that the carbon content of the M-A constituents was significantly higher than the carbon content of the matrix (within the range of 0.6-1.1%). The results of EDS analyses from the matrix and the M-A constituents showed that there was no detectable compositional difference between the blocky M-A constituents on the fracture surfaces and the matrix. The obtained hardness and chemical composition of the constituents prove that they really are M-A constituents.

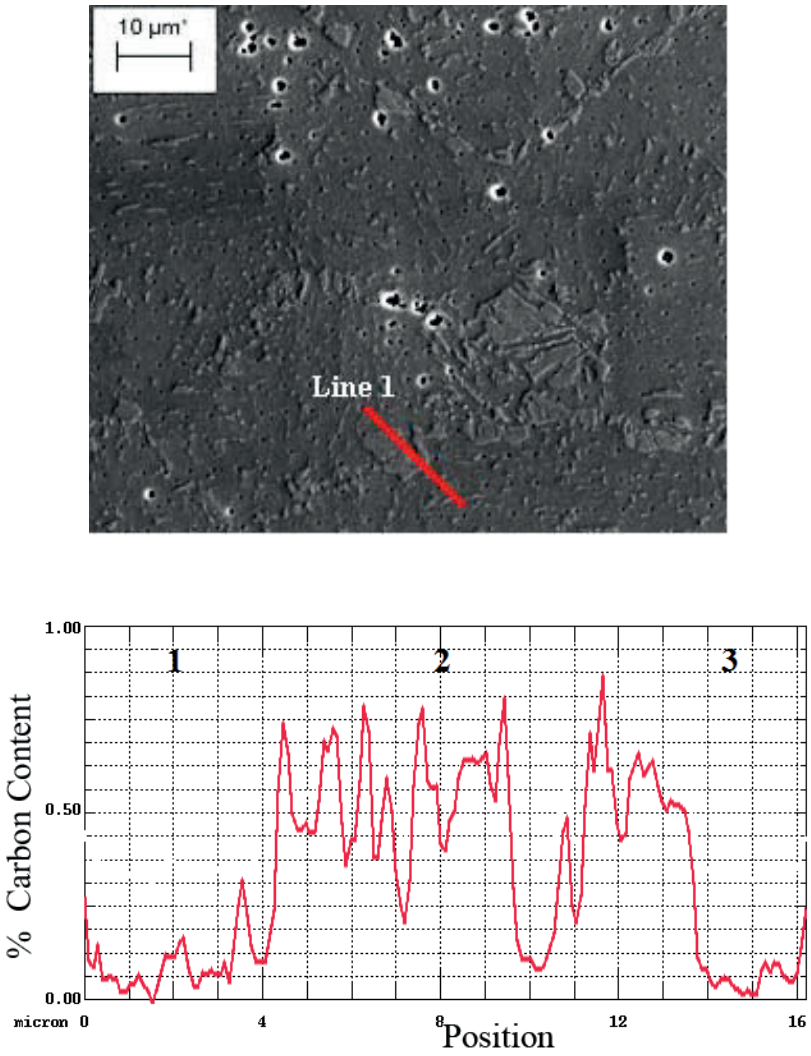

Fig. 2. *EMPA line scan analysis along line 1.*

In order to identify and classify the cleavage crack initiation sites, a detailed fractographic examination was carried out on the fractured specimens by SEM. These observations indicated that blocky M-A constituents were located at the initiation points of the cleavage cracks, Fig. 3. The opposite surfaces showed holes corresponding to the location where the particle had been located and pulled out.

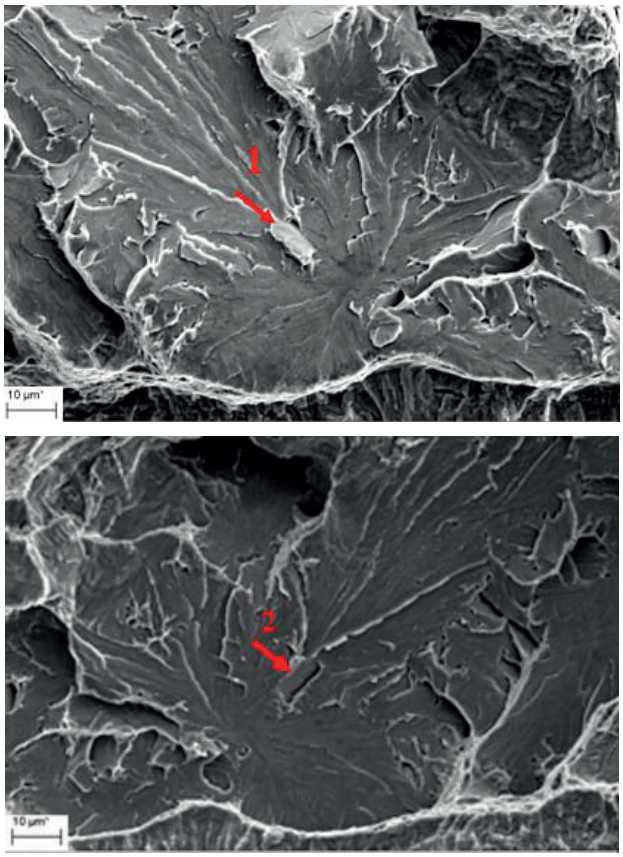

Fig. 3. *Fracture surface of the specimen tested at 0°C.*

According to these observations, it can be concluded that the brittle fracture initiation occurred at blocky M-A constituents formed on prior austenite grain boundaries. The main fracture mechanism appeared to be debonding between the M-A constituents and the surrounding matrix.

However, in some cases, a cleavage facet initiated from the area between two connected or nearly connected M-A constituents in the microstructure. Detailed TEM analysis revealed the presence of twinned martensite inside particles located at initiation sites of cleavage facets, proving that they are M-A constituents, and thus that M-A constituents are potential initiation sites for cleavage cracks. The TEM specimen cut from the fracture surface by applying the FIB technique.

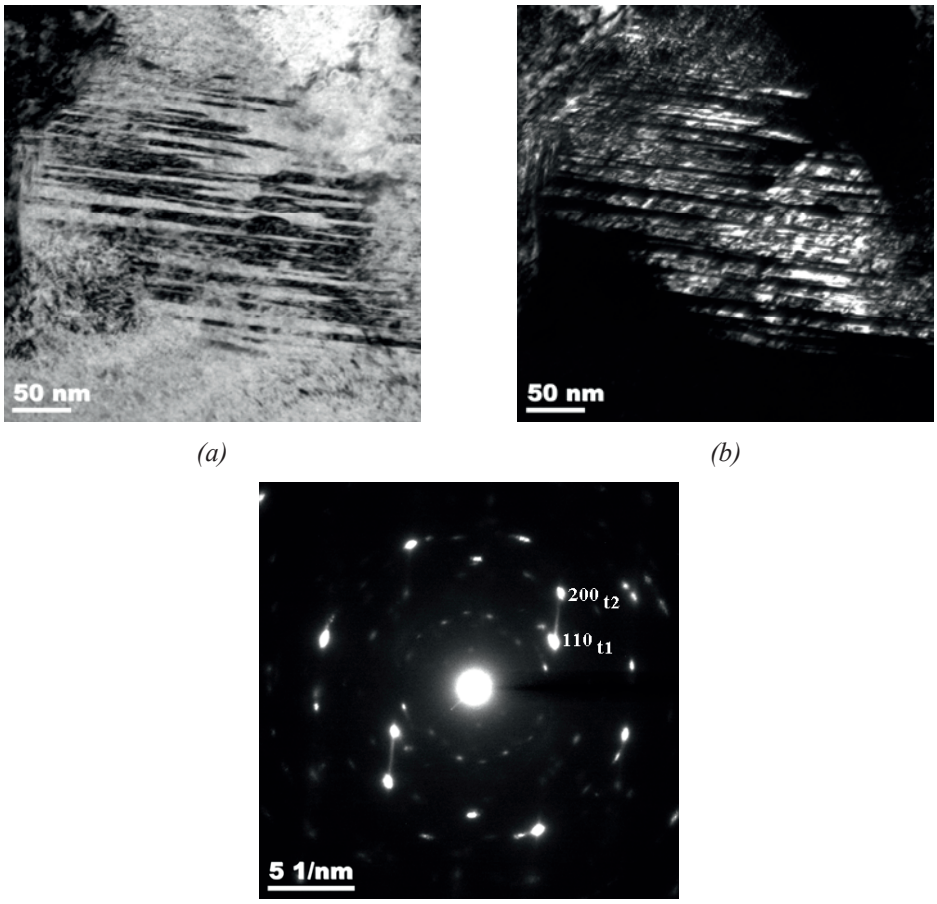

(a) *(b)*

(c)

Fig. 4. *(a) and (b) show bright and dark field micrographs of twinned martensite, (c) selected area diffraction pattern (SADP) of the twinned region in(a) and (b).*

Two main different initiation sites of fracture in HSLA steels subjected to ICCGHAZ weld simulation have been reported: 1- debonding of the M-A constituent/matrix interface, 2- cracking of the M-A constituent. During the present work, the blocky M-A constituents were not observed to crack. In the majority of cases the fracture facets had initiated preferentially from the M-A constituents that debonded rather than cracked.

4. 2 Paper 2

Cleavage fracture initiation at M-A constituents in the intercritically coarse grained heat affected zone of a HSLA steel.

The main objective of this paper is to identify the M-A constituents initiating brittle fracture within the intercritically coarse grained HAZ by using transmission electron microscopy (TEM). For this purpose, the focused ion beam (FIB) technique was applied to make site specific TEM specimens of M-A constituents located at cleavage facet initiation points on fracture surfaces of the Arctic pipeline steel X80. However, a cleavage crack can also be initiated from the area between two nearby M-A constituents where the residual phase transformation stresses and stress concentrations due to debonding of the M-A constituents are overlapping. The initiation sites were identified from the river line pattern radiating from each single initiation point.

Fig. 1 shows matching cleavage facets in the opposite fracture surfaces of a CTOD samples tested at -60ºC. The figure illustrates an example of re-initiation occurring in the region between several blocky M-A constituents, indicated by arrows 2, 3 and 4. The volume between the debonded M-A constituents has probably been constrained due to high local stresses, which has caused a microcrack to form.

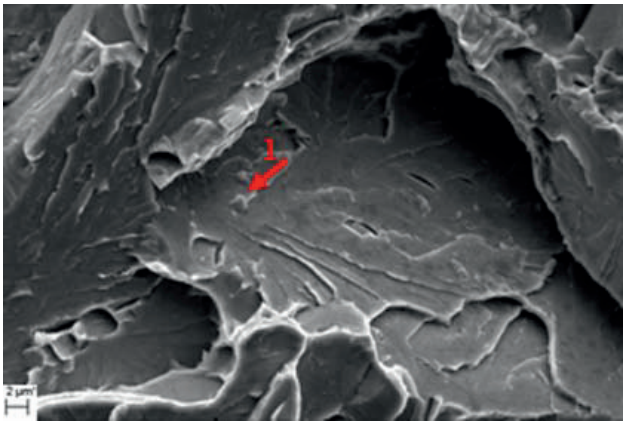

(a)

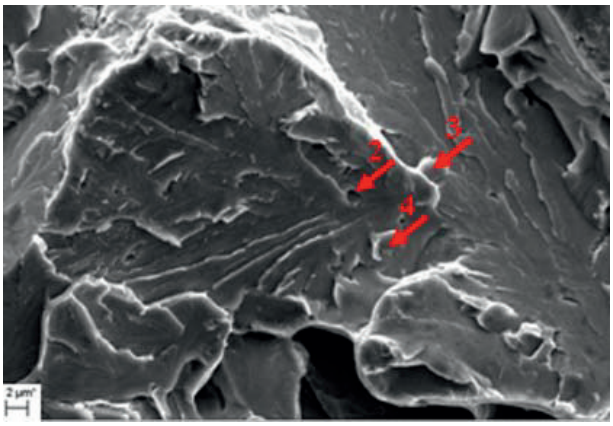

(b)

Fig. 1. *Opposite fracture surfaces of the specimen CTOD tested at -60 °C.*

Fig. 2 shows an example of bright and dark field images from a particle that was located in one of the facet initiation points of a cleavage crack. The bright and dark field images show that the particle is composed of twinned martensite. A selected area diffraction pattern (SADP) from a volume including this twinned martensite region is shown in Fig. 2c. The spot pattern in Fig. 2d is a schematic illustration of this diffraction pattern, and it shows that the pattern is composed of two individual patterns from each of the two twin orientations with 211 as a common diffraction spot. The two spots indexed 110t1 and 200t2 are from the two different twin orientations, respectively. The common diffraction spot 211 proves that the twin plane is (211), and in accordance with this, the [211] direction is oriented normal to the twin planes.

TEM micrographs of other particles located in initiation sites of cleavage facets showed that the presence of twinned martensite within the particles in all cases (five cases). In each case, the two dark field images showed opposite twin contrast, for instance, Fig. 3 shows the TEM micrographs of particle located in initiation sites of the cleavage facets of CTOD tested at -60°C.

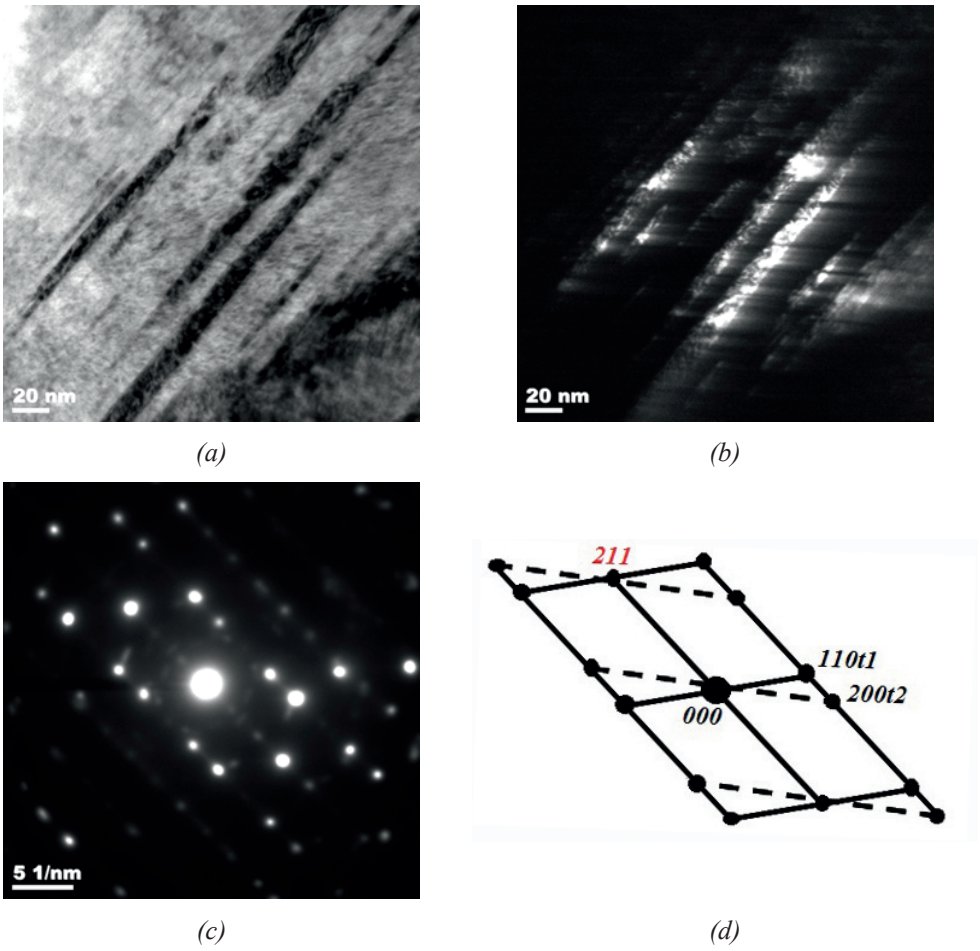

Fig. 2. *(a) and (b) show bright and dark field micrographs of twinned martensite, (c) selected area diffraction pattern of twin region, (d) schematic presentation of (c).*

Thus it can be concluded that the particles located in all the cleavage initiation sites are M-A constituents containing high carbon plate martensite. It can be concluded that the formation of M-A constituents along prior austenite grain boundaries is one of the most important reasons for the loss in ICCGHAZ toughness after welding.

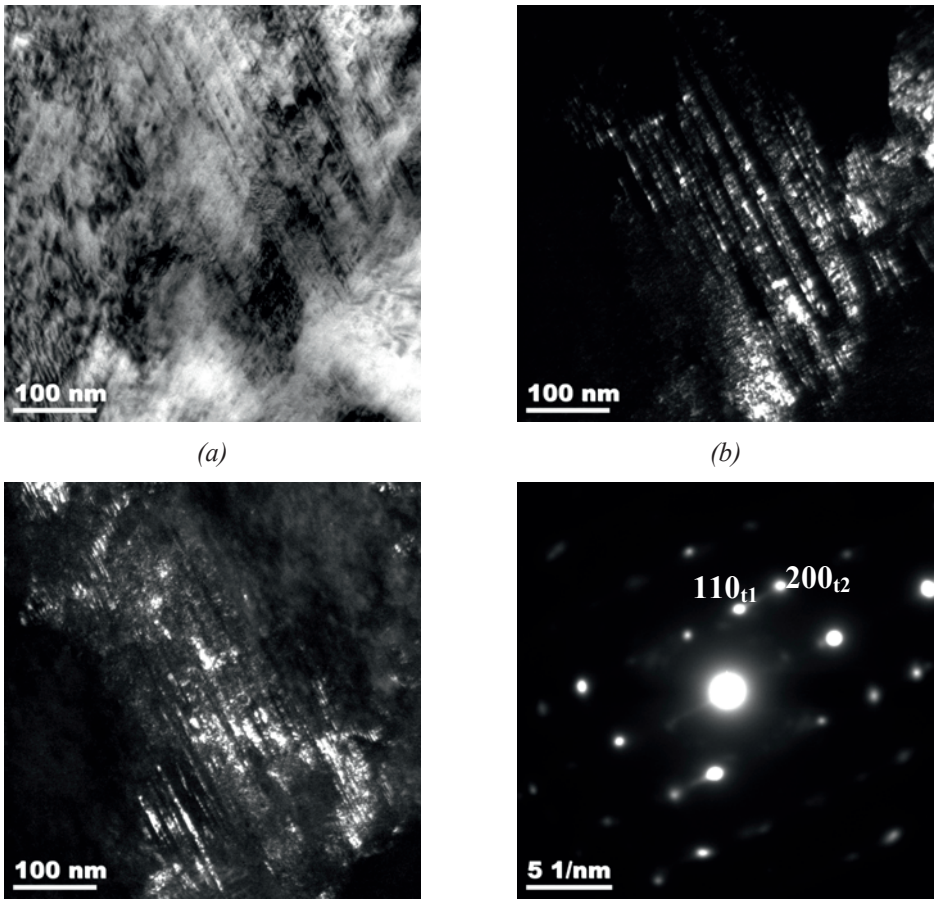

Fig. 3. *(a), (b) and (c), Bright and dark field micrographs of twinned martensite, (d) selected area diffraction pattern (SADP) of twin region. The dark-field image was obtained by using the indexed spots marked t_1 and t_2 in the SAD pattern (c).*

The distance between the pre-fatigue crack tip and the initiation sites of cleavage fracture, Xc, were also measured by scanning electron microscopy. The measured Xc values are presented in Fig. 4, as a function of temperature and CTOD value. It is seen that the critical distance from the pre-fatigue crack tip to the crack initiation site of the cleavage crack increased with increasing CTOD value. The maximum tensile stress is typically located at distances corresponding to the double CTOD value from the crack tip where the blue line represents in Fig. 4. In this work the

cleavage crack initiation sites were always located at distances less than the double CTOD value from the fatigue notch, Fig. 4. It can be concluded that the cleavage initiation is not only influenced by the maximum tensile stress distribution in front of the crack tip, but also by the strain condition. These results indicating that a combination of high stresses and high strains triggered the initiation of the cracks.

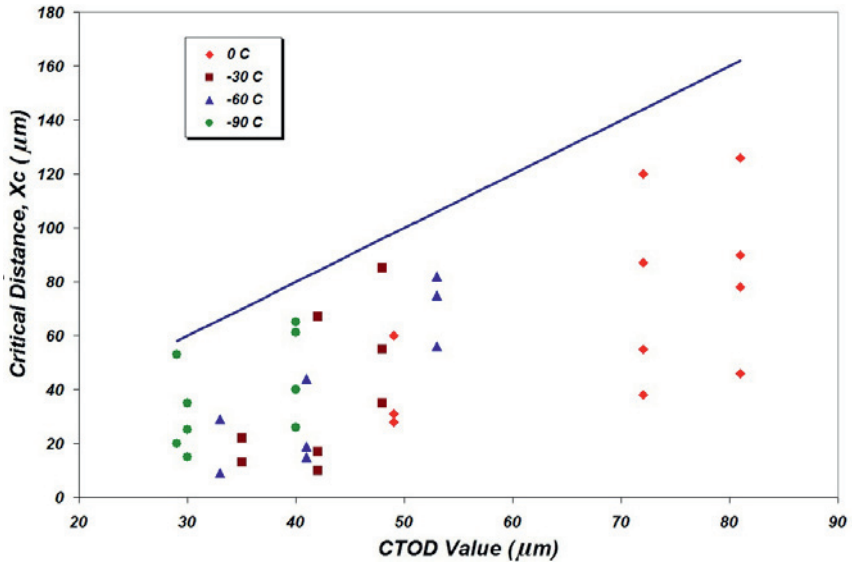

Fig. 4. *Relationship between Xc and CTOD Value in the CTOD specimens fractured at low temperatures.*

The presence of a blocky M-A constituent may cause an increase in the matrix stress close to the interface between the M-A constituent and the matrix. During deformation, the stress concentration increases due to the hardness difference between the M-A constituent and the surrounding matrix. It can be concluded the total level of stress around the M-A constituents may become significantly larger than the nominal stress value and consequently cause initiation of cleavage fracture. This implies that brittle fracture is easily initiated when M-A constituents are located near the fatigue crack tip, and it is also controlled by the accumulation of a continuum stress field and local plastic strain.

4. 3 Paper 3

Slip system activation during low cycle fatigue at low temperatures in HSLA steels

The main goal of this paper is to identify the active slip systems in the free surface of the coarse-grained heat affected zone of the bainitic X80 steel during deformation at low temperatures. Cyclic bend loading was chosen as deformation mode for this purpose. EBSD studies combined with observations made in the scanning electron microscope (SEM) and the scanning probe microscope (SPM) were applied in order to investigate the slip activity and to identify the operating slip systems.

In order to identify the slip system activity after the fatigue tests, scanning electron microscopy and scanning probe microscopy were used. Fig. 1 shows the specimen surface features after 2000 cycles at high magnification. It can be seen that there are still some grains or packets without any detectable slip markings on the surface of the specimen, and probably these grains have only been elastically strained at this strain level. The SPM image in Fig. 1b shows a series of nearly equidistant and parallel slip lines present within the red square in Fig. 1a. The intersection between an active slip plane and the polished specimen surface has created a step which height can be accurately measured by SPM, Fig. 1d. The different steps of different heights correspond to the slip lines formed at the free surface of the polished specimen.

EBSD measurements were performed to identify the active slip systems during the fatigue tests. In order to identify the actual slip system (slip plane and slip direction), the values of the Schmid factors (μ) were also calculated for each slip marking.

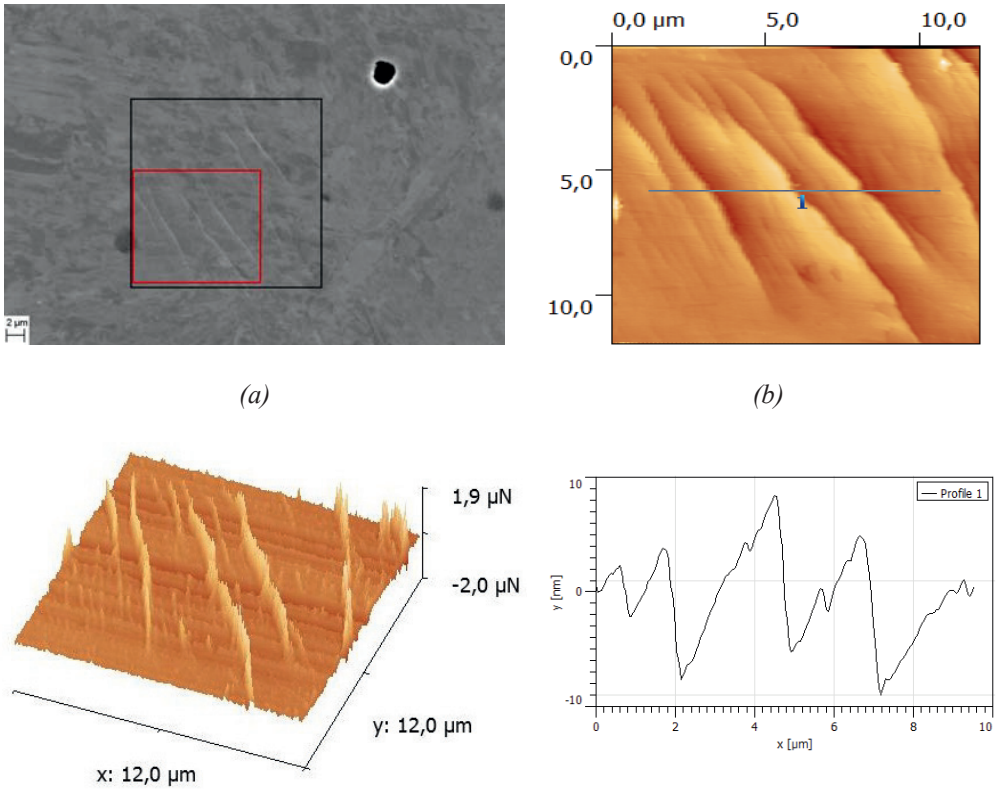

Fig. 1. *(a) SEM micrograph of the specimen after bending, (b) corresponding SPM image to the red square in (a), (c) 3D image of the same area as (b), (d) Profile of the slip step along the cross section indicated in (b) by line 1.*

According to Schmid's law, the activated slip system is supposed to be that with the highest Schmid factor. For this purpose, the Schmid factors for each potential slip system in the BCC structure (i.e. {110} <111>, {112} <111> and {123} <111>) were calculated by using the Euler angles that were obtained from the EBSD results. The crystallographic orientation data of the grains were stored as Euler angles (φ1, ϕ, φ2).

Fig. 2 shows the poles of all active slip planes which were investigated in this work. The angles between the normal of the active slip planes and the loading direction identified by applying the Wulfs net. From this figure it is seen that in most cases,

the poles of the active slip planes are located 40-50º from the loading direction. This agrees well with theory, stating that the maximum possible Schmid factor of 0.5 is reached in slip planes oriented 45º to the loading direction.

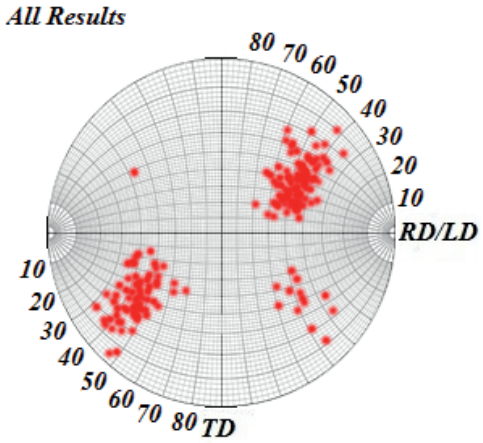

Fig. 2. *Poles of activated slip planes were obtained by EBSD.*
RD: Rolling Direction, LD: Loading Direction, TD: Transverse Direction.

Fig. 3 illustrates the frequencies of the maximum Schmid factors calculated for all potential slip systems in all ferritic grains, blue symbols. It can be seen that the highest Schmid factor is larger than 0.32 in the whole temperature range. The frequencies of the Schmid factors corresponding to the activated slip systems of the same ferritic grains are given by the red symbols. As can be seen, these values define two different regions with a slope change at around μ=0.4, defining two characteristic domains. In the low μ region (μ= 0.32-0.4) the red and blue values are almost overlapping, thus it can be concluded that in this range the Schmid's law is obeyed. On the contrary, in the high μ region (μ higher than 0.4) the two values do not overlap, clearly indicating that the activated slip systems are not necessarily those having the highest Schmid factor.

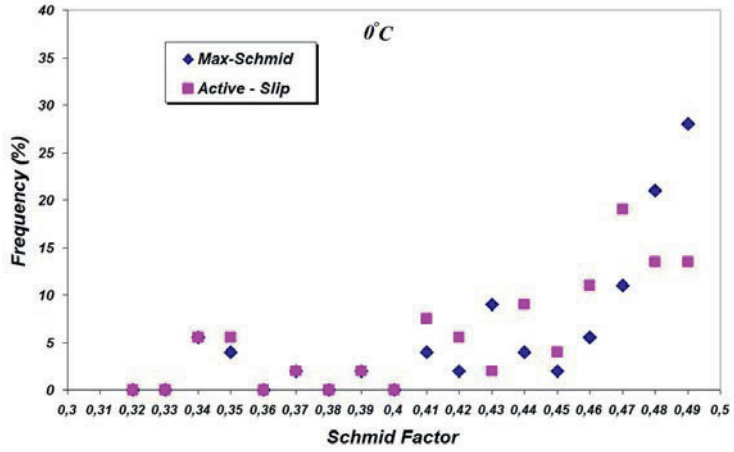
0°C
Max-Schmid
Active - Slip
Frequency (%)
0 5 10 15 20 25 30 35 40
0,3 0,31 0,32 0,33 0,34 0,35 0,36 0,37 0,38 0,39 0,4 0,41 0,42 0,43 0,44 0,45 0,46 0,47 0,48 0,49 0,5
Schmid Factor

(a)

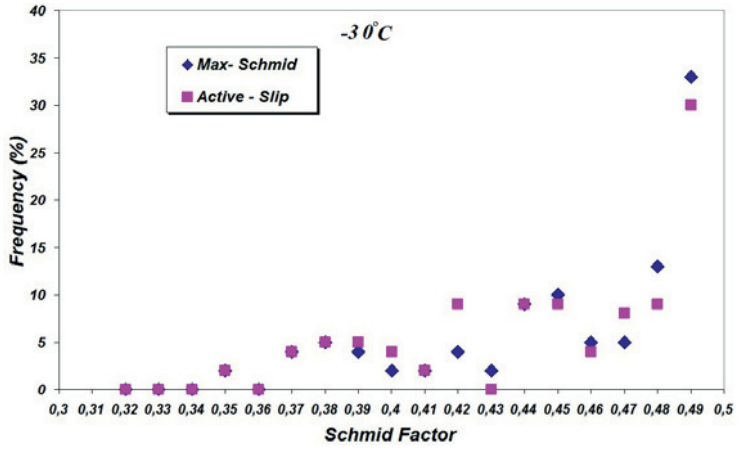
-30°C
Max- Schmid
Active - Slip
Frequency (%)
0 5 10 15 20 25 30 35 40
0,3 0,31 0,32 0,33 0,34 0,35 0,36 0,37 0,38 0,39 0,4 0,41 0,42 0,43 0,44 0,45 0,46 0,47 0,48 0,49 0,5
Schmid Factor

(b)

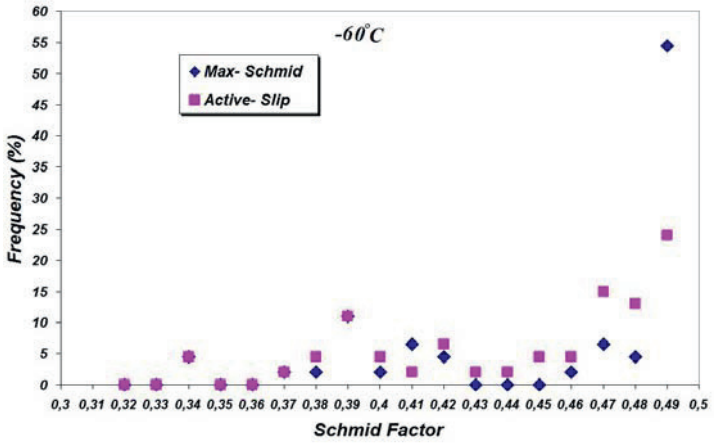
-60°C
Max- Schmid
Active- Slip
Frequency (%)
0 5 10 15 20 25 30 35 40 45 50 55 60
0,3 0,31 0,32 0,33 0,34 0,35 0,36 0,37 0,38 0,39 0,4 0,41 0,42 0,43 0,44 0,45 0,46 0,47 0,48 0,49 0,5
Schmid Factor

(c)

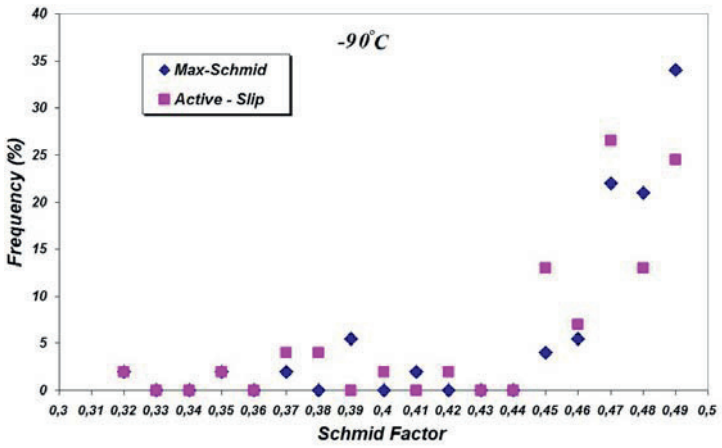

(d)

Fig. 3. *Accumulated frequency of the highest Schmid factors and activated slip systems within the deformed region at different temperatures, (a) 0ºC, (b) -30 ºC, (c) -60 ºC and (d) -90 ºC*

The distribution of the angles between the slip trace markings and the loading axis, Φ, and angles between the loading axis and the theoretical surface trace of the slip planes with the highest Schmid factor, λ were also presented in Fig. 4. It can be seen that there is a similar tendency in the actual distribution of activated slip plane traces and the theoretical distribution of slip plane traces, which illustrates that most grains follow Schmid's law during the fatigue test. It is also seen that the distribution of angles λ and Φ is not exactly the same, thus it is concluded that some grains of the steel studied do not follow Schmid's law.

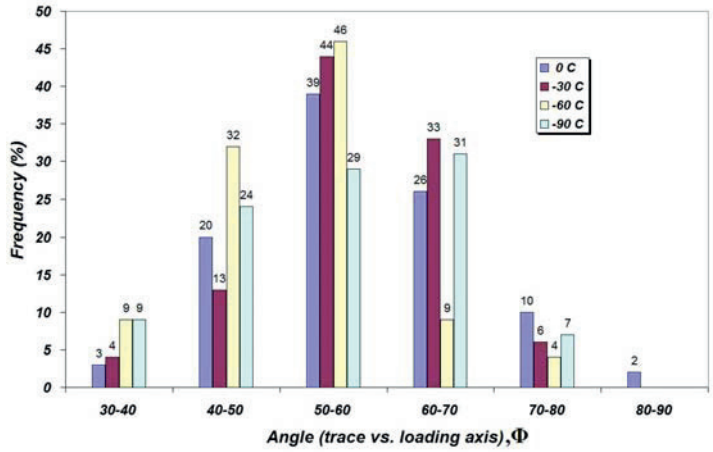

(a)

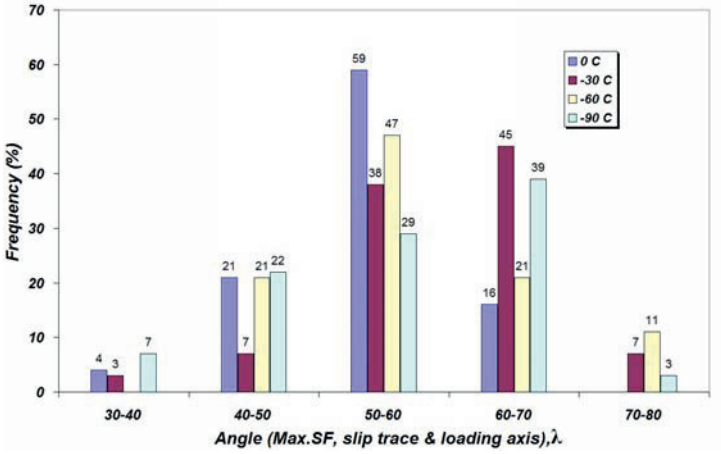

(b)

Fig. 4. *Distribution of the angle between a loading axis and (a) trace of slip marking, (b) maximum Schmid factor slip traces.*

It can be thus concluded, the Schmid factor is not the only determining parameter for activation of slip within ferritic grains, and other parameters must be considered to explain whether or not a ferritic grain develops plastic deformation. The slip activity in BCC structures depends on the applied stress, grain size, internal stresses concentrated at the grain boundary, as well as the slip activity developed in the neighbouring grains and their relative orientation.

4. 4 Paper 4

Application of combined EBSD and 3D-SEM technique on crystallographic facet analysis of the X80 steel at low temperature

In this paper, electron backscatter diffraction has been applied to assess crystallographic features of fracture surfaces after CTOD testing of weld thermally simulated CGHAZ and ICCGHAZ samples of API X80 pipeline steel. This technique has been combined with computer assisted 3D- Imaging. The objective of the paper has been to apply this method to determine the crystallographic planes and orientations of cleavage facets within the heat affected zone in the fracture surfaces created at low temperatures down to -90ºC.

The fracture toughness (CTOD) values as a function of test temperature for both HAZ conditions are shown in Fig. 1. It can be seen that, the mean CTOD value at each temperature is higher for the CGHAZ specimens than for the ICCGHAZ specimens.

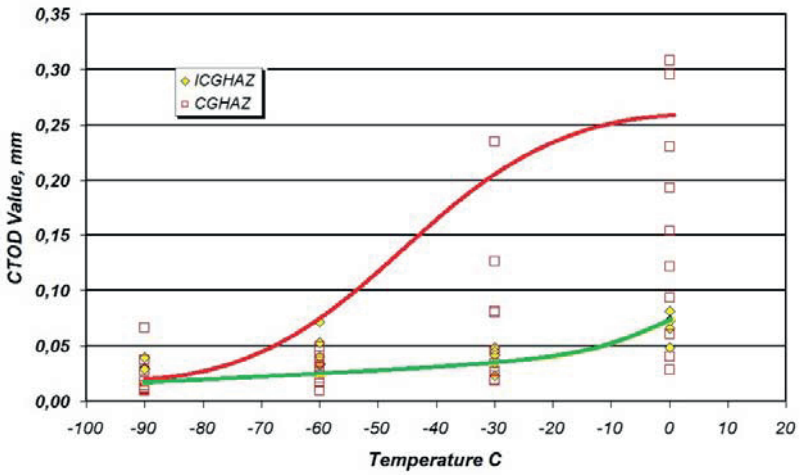

Fig. 1. *The variation of CTOD values with test temperature.*

Moreover, this difference becomes larger with increasing temperature. In the case of CGHAZ, the temperature dependence of the CTOD value (mean value) could be represented by a sigmoidal curve, between a lower and upper shelf plateau, associated with brittle and ductile fracture, respectively. On the other hand, the mean fracture toughness values for the ICCGHAZ specimens were approximately independent of test temperature (within the tested range) and also lower than those of the CGHAZ specimens in the whole temperature range.

Typical fracture surfaces of CTOD specimens are presented in Fig. 2. The fracture mechanism changed with test temperature from a mixture of ductile and brittle to completely brittle fracture with decreasing temperature from 0ºC to -90ºC for the CGHAZ specimens (Fig. 2b, d and f). These fracture mechanisms are characteristic of high, medium and low CTOD values, respectively. Although the fracture was dominated by the cleavage mode for CGHAZ specimens tested at -60 °C, there was still some evidence of plastic tearing by microvoid coalescence, Fig. 2d. Fig. 2a, c and e contain examples of cleavage initiation sites in the fracture surface of ICCGHAZ samples.

The 3D imaging procedure was used to construct a 3D model of a cleavage facet that was located in the fracture surface. An example of the application of this procedure is given in the following. The sample is an ICCGHAZ specimen that was CTOD tested at -30 ºC. Fig. 3 (a) shows the 3D- simulated image of a cleavage facet, and its depth profile along the line AB oriented normal to the trace between the facet and the polished surface, is shown in Fig. 3b. The line profile shows that the angle α between the cleavage facet and the polished surface in this case is 75º, which is also the angle between the two plane normals.

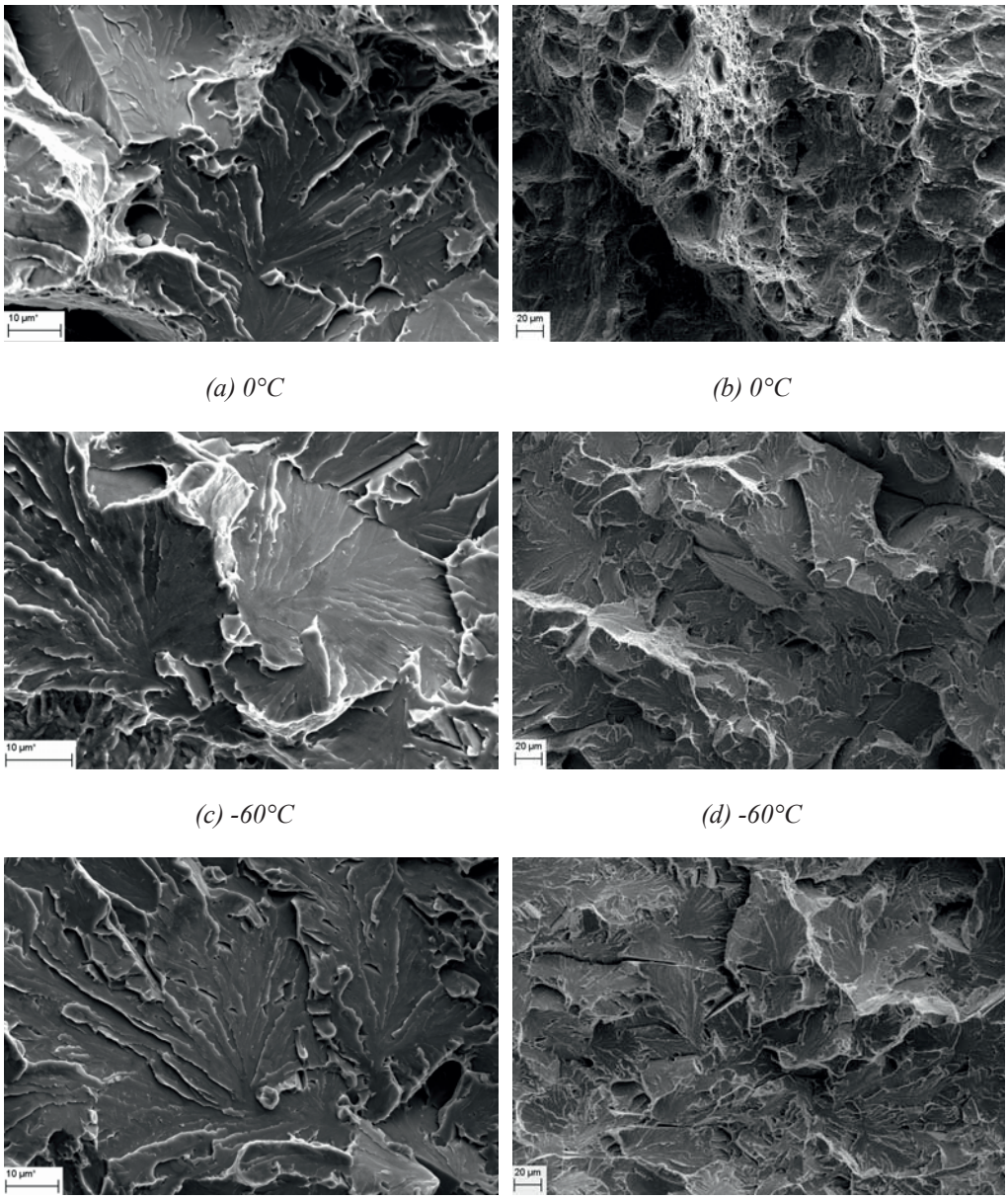

(a) 0°C *(b) 0°C*

(c) -60°C *(d) -60°C*

(e) -90°C *(f) -90°C*

Fig. 2. *Fracture surface of the specimen at different temperature. (a), (c), (e) ICCGHAZ, (b), (d), (f) CGHAZ region.*

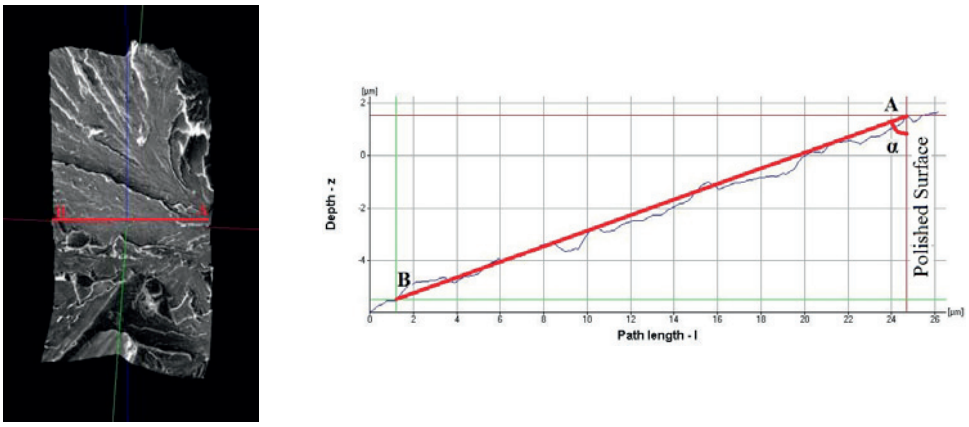

(a) *(b)*

Fig. 3. *Micrograph of a region on a fracture surface , a) 3D- elevation model of the facet, b) Height profile along the line shown in (a).*

In this work, to identify the actual crystallographic cleavage plane of each facet, an EBSD pattern was recorded close to the trace of the cleavage facet in the fracture surface with the polished surface, and from this pattern the poles of the possible cleavage planes, i.e. {100}, {110}, {211} and {310} were plotted in individual pole figures and compared with the data from the 3D simulation. For instance, Fig. 4 illustrates the EBSD results related to the cleavage facet that is presented in Fig. 3a. The pole of the cleavage facet in Fig. 3a should be located along the line n, which is normal to the line T (trace of the cleavage facet in the fracture surface with the polished surface), in the pole figure. The exact position of the pole should be located 75º from the normal direction ND, given by the short arc segment intersecting line n. From the four pole figures, it is seen that there is only one pole within the {100} family that coincides with this intersection, so the facet in Fig. 3a belong to the {100} family.

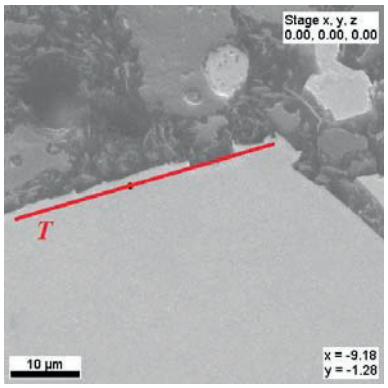

(a) Metallographic polished length section

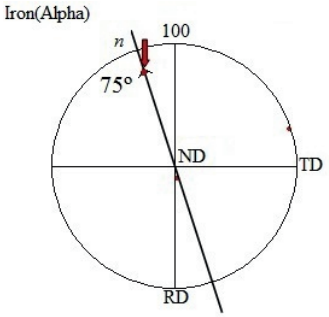

(b) (100) pole figure

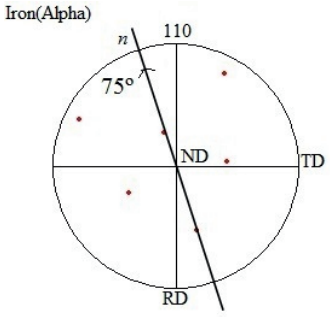

(c) (110) pole figure

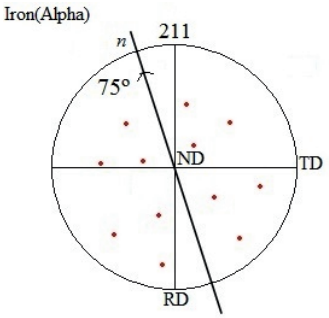

(d) (211) pole figure

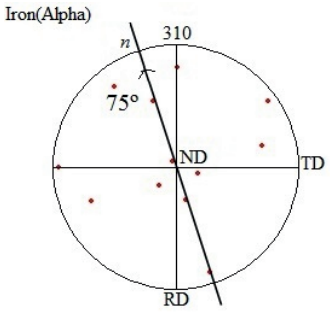

(e) (310) pole figure

Fig. 4. *EBSD result, RD: Rolling Direction, TD: Transverse Direction, ND: Normal Direction.*

This analysis was repeated for 40 randomly selected cleavage facets for each test temperature. The results are presented in Table 1. If the number of cleavage facets of each crystallographic type is divided by the number of equivalent planes within

each family of planes, we obtain a number that gives the potential of each single crystallographic plane to become a cleavage plane, which is displayed in Fig. 5.

Table 1 Number of cleavage facet planes for different test temperature

Temperature \ Crystallographic plane		{100}	{110}	{211}	{310}
CGHAZ	0ºC	18	3	9	10
	-30 ºC	11	10	10	9
	-60ºC	16	7	5	12
	-90ºC	13	8	9	10
ICCGHAZ	0ºC	9	5	12	14
	-30 ºC	15	7	10	8
	-60ºC	15	3	13	9
	-90ºC	12	4	13	11

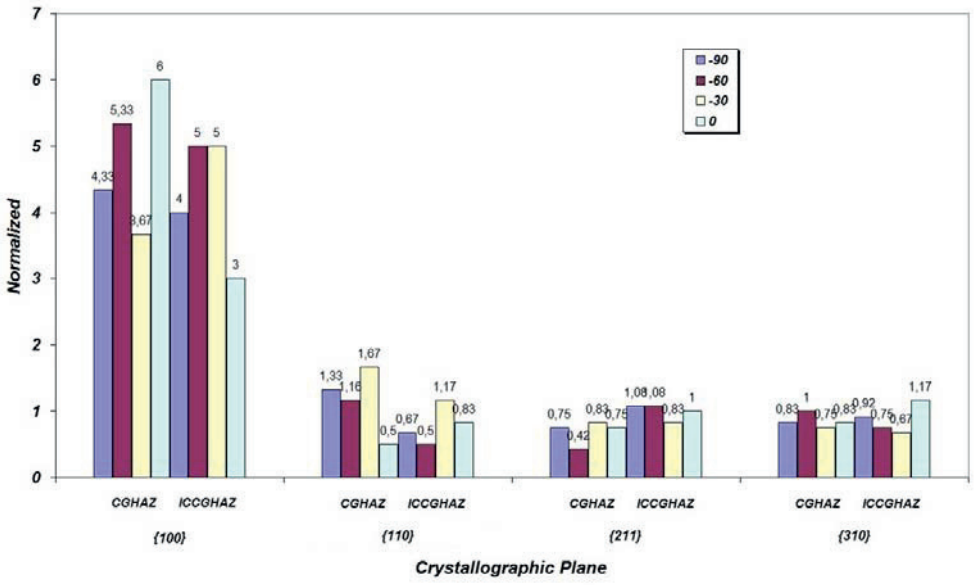

Fig. 5. *Distribution of normalized numbers of cleavage planes at low temperatures.*

It can be concluded that the cleavage facets can propagate along different crystallographic planes at subzero temperatures. It is seen that the {100} and {110}

planes are the most potent cleavage planes for CGHAZ microstructures, while the {100} and {211} planes are the most potent cleavage planes at temperatures lower than -30 °C for the ICCGHAZ microstructures.

According to this observation, it can be suggested that fracture of the ICCGHAZ specimens might have occurred by a mixture of different mechanisms at low temperatures. For instance, deformation twinning might have occurred at the lowest temperature range (the ductile to brittle transition) at the onset of yielding in these specimens. The detailed examination of the polished and etched surfaces (both CGHAZ and ICCGHAZ) revealed the presence of deformation twinning only within the heat affected zone of the ICCGHAZ samples that were tested at the lower two temperatures (-60ºC and -90ºC). These samples contain M-A constituents that might be able to encourage the development of deformation twinning during CTOD testing at low temperatures.

For instance, Fig. 6 shows deformation twinning nucleated from the M-A constituents which are indicated by arrows (Fig. 6b) in the vicinity of a cleavage crack in an ICCGHAZ sample CTOD tested at -60 ºC. It is seen that the 211 pole which is marked with the red arrow (Fig. 6c), strongly supporting the assumption that the parallel lines indicated by the arrow in Fig. 6 are traces of 211 twin planes.

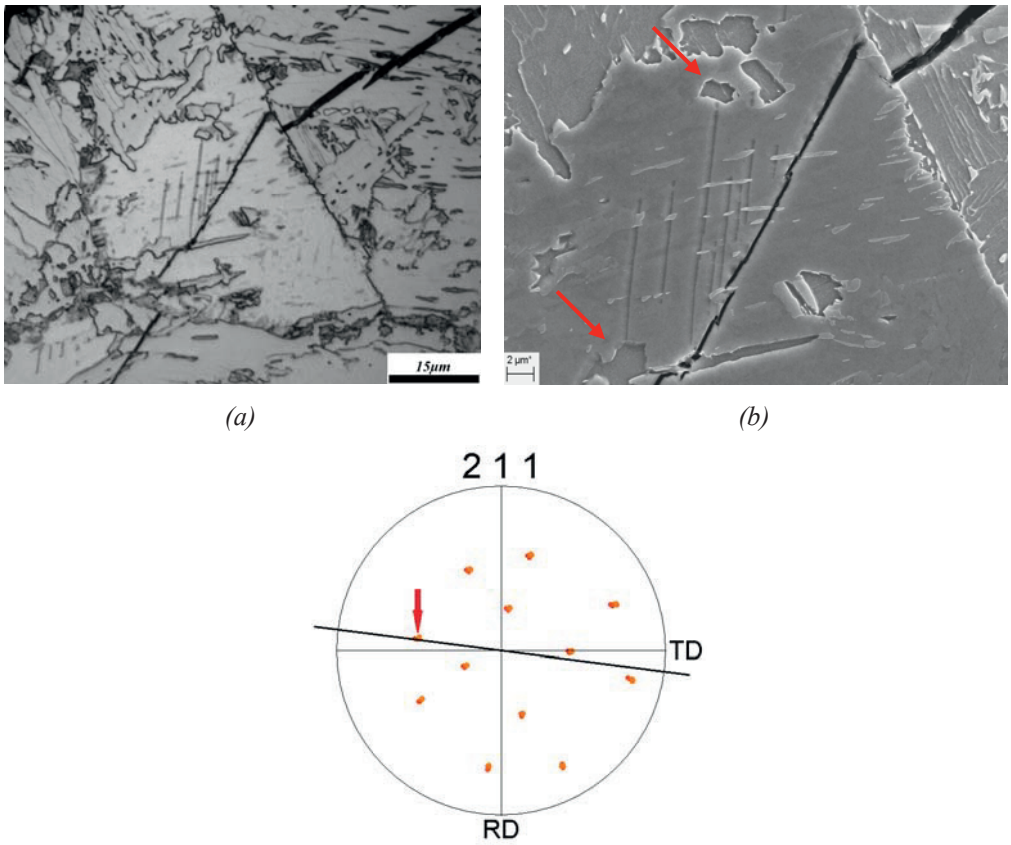

(a) *(b)*

(c)

Fig. 6. *(a) and (b) light optical and SEM micrograph of deformation twinning within ICCGHAZ that tested at -60 ºC, (c) (211) pole figure correspond to the deformation twinning in (a) and (b).*

4. 5 Paper 5 and 6

Paper 5: Determination of crystallographic facet orientations on fracture surfaces of an Arctic steel by using EBSD.

Paper 6: Application of electron backscatter diffraction (EBSD) on facet crystallographic orientation studies in Arctic Steels. (The EBSD results of this paper were also presented in paper 5. This paper also included due to the part of the results has been referred in the other papers.)

The main purpose of these papers was to apply the EBSD method to identify the crystallographic planes and orientations of cleavage facets in low temperature fracture surfaces of the X80 Arctic steel. The tested temperature range was -90°C - 0°C.

Electron backscatter diffraction was applied to assess crystallographic features of fracture surfaces after CTOD testing of weld thermally simulated CGHAZ samples of the X80 steel. The crystallographic orientations were obtained by EBSD from a polished section perpendicular to the major fracture surface of the sample. This technique was combined with computer assisted 3D - imaging. The main conclusions of the work are:

1- The fracture mechanism changes with the test temperature from ductile to completely brittle with decreasing temperature from 0ºC to -90ºC; corresponding to the upper and lower part of the CTOD vs. temperature curve.

2- The EBSD results in combination with the cleavage trace directions were consistent with crack propagation on {100}, {110}, {211} and {310} planes.

3- The number of cleavage facet planes of the {100} family was significantly higher than those of other plane families in the tested temperature range, especially when

considering the number of cleavage facet planes normalized with the number of planes within each family.

4- During this investigation, the tendency seemed to be that the number of {100} facets decreased and the number of {110} facets increased with decreasing test temperature. The numbers of {211} and {310} facets were nearly independent of test temperature.

5- The {100} and {110} planes were the most potent crystallographic planes for cleavage fracture at subzero temperatures.

5. Concluding Remarks:

In this PhD work, the effect of microstructure and changes in microstructure introduced by welding procedure, on the brittle to ductile transition properties of an Arctic pipeline steel have been investigated. The experimental works were applied at low temperatures down to -90°C (0°C, -30°C, -60°C and 90°C). The basic conclusions from this PhD work on the Arctic steel X80 can be divided into three different categories: (1) the low temperature embrittling effects of M-A constituents formed in the weld heat affected zone after welding, (2) slip system activity during low temperature deformation, and (3) crystallographic features of brittle fracture surfaces after low temperature CTOD testing. The main conclusions of the work are as follows:

Category 1:

- Two main types of M-A constituents were identified by SEM: blocky M-A constituents formed along prior austenite grain boundaries, and elongated stringers, developed between bainite and martensite laths. The specific configurations of connected or nearly connected M–A constituents were also observed.
- Hardness measurements performed by Vickers indentation and nanoindentation showed that the hardness of the M-A constituents was significantly higher than that of the matrix. The hardness of the M-A constituents was in the range of 600-1000 Hv.
- The carbon concentration of the M-A constituents was measured by EPMA quantitative analysis. The results from the EPMA analysis showed that the carbon content of the M-A constituents was significantly higher than the carbon content in the matrix (within the range of 0.6-1.1%).
- Detailed TEM analysis revealed the presence of twinned martensite inside particles that are located at initiation sites of cleavage facets, proving that they are M-A constituents, and thus that M-A constituents are potential initiation sites for cleavage cracks.

- In this investigation, cracks initiated either from debonded M-A constituents or from the region between two or more closely separated blocky M-A constituents.
- Fractographic analysis revealed that the critical distance from the pre-fatigue crack tip to the crack initiation site of the cleavage crack increased with increasing CTOD value. The critical distance was less than the double CTOD value from the crack tip, indicating that a combination of high stresses and high strains triggered the initiation of the cracks.

Category 2:

- The lowest Schmid factor that was observed to activate a slip system was 0.32 in the whole temperature range. The slip system activation was divided into two different regions: (i) the slip activation followed Schmid's law for low Schmid factors (0.32 - 0.4), and (ii) the slip activation does not follow Schmid's law for high Schmid factors (>0.40).
- The first activated slip system is not necessarily that with the highest Schmid factor at low temperatures. Thus, it can be concluded that the Schmid factor is not the only parameter that determines the activation of slip. Other parameters such as crystallographic orientation of the loading axis and slip activity in the neighbouring grains must be considered.
- The distribution of angles between the loading axis and (i) observed slip traces, and (ii) theoretical traces of slip planes with maximum Schmid factor had a maximum for angles of 50-70º.

Category 3:

- The potential for a single crystallographic plane to become a cleavage facet plane was significantly higher for {100} planes than for other planes in the tested temperature range for both CGHAZ and ICCGHAZ specimens.
- The number of {100} facets decreased with falling temperature in the case of CGHAZ, while the tendency was opposite for the ICCGHAZ specimens.

- For the CGHAZ specimens, there may seem to be a tendency of decreasing number of {100} facets and increasing number of {110} facets with decreasing temperature. The numbers of {211} and {310} facets were nearly independent of temperature. It can thus be concluded that the {100} and the {110} planes were the most favourable cleavage facet planes at low temperatures in the CGHAZ specimen.
- For the ICCGHAZ specimens, the number of {211} facets were significantly higher than the number of {110} facets. Especially at temperatures lower than -30 ºC (Arctic region) deformation twinning might have occurred in these specimens.
- Detailed EBSD analysis proved that deformation twinning occurred along {211} planes at low temperatures in the case of ICCGHAZ specimens.

References

[1] W. W. Bose-Filho, A. L. M. Carvalho and M. Strangwood, “Effect of alloying elements on the microstructure and inclustion formation in HSLA multipass welds”, Materials Characterization, Vol. 58, 2007, pp 29- 39.

[2] S. K. Das, S. Sivaprasad, S. Dasa, S. Chatterjee and S. Tarafder, “The effect of variation of microstructure on fracture mechanics parameters of HSLA-100 steel”, Materials Science and Engineering A, Vol. 431, 2006, pp 68-79.

[3] A. Lambert-Perlade, A. F. Gourgues and A. Pineau, “Austenite to bainite phase transformation in the heat-affected zone of a high strength low alloy steel”, Acta metallurgica, Vol. 52, 2004, pp 2337-2348.

[4] OM. Akselsen, JK. Solberg and Ø. Grong, “Effects of martensite-austenite (M-A) islands on intercritical heat-affected zone toughness of low carbon miroalloyed steels”, Scandinavian Journal of Metallurgy, Vol. 17, 1988, pp 194-200.

[5] C. L. Davis, and J. E. King, “Cleavage initiation in the intercritically reheated coarse-grained heat affected zone: Part II. Failure criteria and statistical effects”, Metallurgical and Materials Transactions A, Vol. 27, 1996, pp 3019-3029.

[6] S. Shanmugam, N. K. Ramisetti, R. D. K. Misra, J. Hartmann, and S. G. Jansto, “Microstructure and high strength-toughness combination of a new 700MPa Nb-microalloyed pipeline steel”, Materials Science and Engineering A, Vol. 478, 2008, pp 26-37.

[7] J. Bauer, P. Fluss, E. Amoris and V. Schwinn, “Microstructure and properties of thermomechanical controlled processing steels for linepipe applications”, Ironmaking and steelmaking, Vol. 32, 2005, pp 325-330.

[8] M. Meier, “THE ductile to britthle transition”, Department of Chemical Engineering and Materials Science, University of California, Davis, 2004.

[9] F. B. Pickering, “High strength low alloy steels - A decade of progress”, Proceeding of International Symposium, Microalloying 75, Washington DC, October 1-3, 1975, p 9.

[10] C. I. Garcia and A. J. DeArdo, “Microalloyed HSLA steels”, Proceeding of World Materials Congress, Chicago, Illinois, September 24-30, 1988, p 291.

[11] S. A. Blackman, “An economic assessment of mechanised welding of high strength linepipe for the Australian pipeline industry”, Pipes and Pipelines International, Vol. 48, 2003, pp 27-37.

[12] V. Chaudhari, “German gas pipeline first to use new generation linepipe”, Oil and Gas Journal, Vol. 93, 1995, pp 40-47.

[13] Y. Terada, “X100 Linepipe with excellent HAZ toughness and deformability”, Proceedings of the 22nd International Conference on Offshore Mechanics and Arctic Engineering (OMAE03), Cancun, Mexico, 8-13 June 2003.

[14] S. Dittrich, “Welding of high yield strength X80 - state of the art 1991”, Welding in the World, Vol. 30, 1992, pp 33-36.

[15] J. M. Gray and M. Pontremoli, “Metallurgical options for API grade X70 and X80 linepipe”, Proceedings of the Conference on Microalloyed HSLA Steels, Chicago, USA, 24-30 Sept 1988, pp 171-199.

[16] M. Okatsu, “Metallurgical and mechanical features of X100 linepipe steel”, Proceedings of the 16th International Conference on Offshore Mechanics and Arctic Engineering (OMAE97), III – Materials Engineering, 1997, pp 119-124.

[17] H. Asahia, H. Fujii and N. Sato, “Heavy wall X80 seamless linepipe”, Proceedings of the 2nd International Conference on Pipeline Technology, Ostende, Belgium, 11-14th September 1995, 2, pp 253-261.

[18a] S. W. Poole, “Properties and Selection - Iron and Steel”, Metals Handbook, 9th edition, ASM, Metals Park, OH, 1978, Vol. 1, p 403.

[18b] S. W. Poole, “Properties and Selection - Iron and Steel”, Metals Handbook, 10th edition, ASM, Metals Park, OH, 1990, Vol. 1, p 389.

[19] Y. Okamura, M. Okushima, H. Tamechiro, T. Kasuya, M. Tanaka, R. Yamaba, H. Inoue and A. Seto, “Development of copper precipitation hardened 780N/mm^2 high strength steel with lower preheating temperature characteristics”, Nippon Steel Technical Report, 1995, Vol. 66, p 65-76.

[20] R. J. Schmitt and E. H. Phelps, Journal of Metals, 1970, Vol. 9, p 47.

[21] F. Blekkenhost, G. M. Ferrari, C. J. Van Der Wekken and F. P. Ijesseling, “Development of high strength low alloy steels for marine applications part 2:

simulation of marine exposure of steel by means of laboratory tests in flowing sea water", Corrosion, Vol. 23, 1988, pp 165-171.

[22] W. A. Laura, "Role of chromium in weathering steel passivation", Materials Performance, 1991, Vol. 9, pp 62-63.

[23] F. Blekkenhost, G. M. Ferrari, C. J. Van Der Wekken and F.P. Ijesseling: "Development of high strength low alloy steels for marine applications", Corrosion, Vol. 21, 1986, pp 163-176.

[24] M. Staratmann, K. Bohnenkamp and T. Ramachandran, "The influence of copper upon the atmospheric corrosion of iron", Corrosion Science, 1987, Vol. 27, pp 905-926.

[25] B. A. Graville, "Cold Cracking in Welds in HSLA Steels", ASM, Metals Park, OH, 1978, p 85.

[26] L. E. Collins, J. D. Boyd, J. A. Jalkman, L. D. Bailey and M. R. Krishnadev, "Microalloyed HSLA steels", World Materials Congress, Chicago, Illinois, September 24-30, 1988, p 607.

[27] E. C. Hamre and A. M. Gilroy-Scott, Proceeding of International Symposium Microalloying'75, Washington DC, October 1-3, 1975, p 375

[28] J. M. Gray, "Microalloyed HSLA steels", World Materials Congress, Chicago, Illinois, September 24-30, 1988, p 61

[29] T. Gladman, "The Physical Metallurgy of Microalloyed Steels", Institute of Materials, London, 1997, p 38.

[30] M. Pontremoli, P. Bufalimi, A. Aprile and C. Jannml, "Development of grade API X80 pipeline steel plates produced by controlled rolling", Metals Technology, Vol. 11, 1984, pp 504-514.

[31] W. B. Morrison, "Relationship between thermo mechanical treatment and properties of HSLA steels", Scandinavian Journal of Metallurgy, Vol. 9, 1980, pp 83-90.

[32] A. Ghose, B. Mishra, S. Das and S. Chatterjee, "Structure and properties of a low carbon Cu bearing high strength steel", Materials Science and Engineering A, 2005, Vol. 396, pp 320-332.

[33] C. H. Lorig and R. R. Adans, “Copper as an alloying element in steel and cast iron”, McGraw-Hill Book Co., New York, 1948.

[34] H. Okada, S. Sekino, Y. Hosoi and T. Murata, “Copper in Iron and Steel”, John Wiley and Sons, New York, 1982, p 83.

[35] P. Cizek, B. P. Wynne, C. H. J. Davies, B. C. Muddle and P. D. Hodgson, “Effect of composition and austenite deformation on the transformation characteristics of low-carbon and ultralow-carbon microalloyed steels”, Metallurgical and Materials Transactions A, Vol. 33, 2002, pp 1331-1349.

[36] H. K. D. H. Bhadeshia and R. W. K. Honeycombe, “Steels microstructure and properties”, Elsevier, third edittion, 2006.

[37] H. K. D. H. Bhadeshia, “The bainite transformation: unresolved issues”, Materials Science and Engineering A, Vol. 273, 1999, pp 58-66.

[38] I. Madariaga, I. Gutierrez and H. K. D. H. Bhadeshia, “Acicular ferrite morphologies in a medium-carbon microalloyed steel”, Metallurgical and Materials Transactions A, Vol. 32, 2001, pp 2187-2197.

[39] H. K. D. H. Bhadeshia, “Modelling of steel welds”, Materials Science and Technology, Vol. 2, 1992, pp 123-133.

[40] J. Y. Suh, J. S. Byun, J. H. Shim, Y. J. Oh, Y. W. Cho, J. D. Shim and DN. Lee, “Acicular ferrite microstructure in titanium bearing low carbon steels. Metallurgical modelling of welding”, Materials Science and Technology, Vol. 16, 2000, pp 1277-1281.

[41] I. Olivares, M. Alanis, R. Mendoza, B. Campillo and J. A. Juarez-Islas, “Development of microalloyed steel for pipeline applications”, Ironmaking and Steelmaking, Vol. 35, 2008, pp 452-457.

[42] P. A. Davies, M. Novovoc, V. Randle and P. Bown, “Application of electron backscatter diffraction (EBSD) to fracture studies of ferritic steels”, Journal of Microscopy, Vol. 205, 2002, pp 278-284.

[43] S. Y. Shin, B. Hwang, S. Lee, N. J. Kim and S. S. Ahn, “Correlation of microstructure and charpy impact properties in API X70 and X80 line-pipe steels”, Materials Science and Engineering A, Vol. 458, 2007, pp 281-289.

[44] A. Lambert-Perlade, A. F. Gourgues, J. Besson, T. Sturel and A. Pineau, "Mechanisms and modeling of cleavage fracture in simulated heat-affected zone microstructures of a High-Strength Low Alloy steel", Metallurgical and Materials Transactions A, Vol. 35A, 2004, pp 1039-1053.

[45] S. Moeinifar, A. H. Kokabi and H. R. Madaah Hosseini, "Influence of peak temperature during simulation and real thermal cycles on microstructure and fracture properties of the reheated zones" Materials and Design, Vol. 31, 2010, pp 2948-2955.

[46] OM. Akselsen, Ø. Grong and JK. Solberg, "Structure-property relationships in intercritical heat affected zone of low carbon microalloyed steels", Materials Science and Technology, Vol. 3, 1987, pp 649-655.

[47] C. L. Davis and J. E. King, "Cleavage initiation in the intercritically reheated coarse-grained heat affected zone: Part I. Fractographic evidence", Metallurgical and Materials Transactions A, Vol. 25, 1994, pp 563-573.

[48] J. H. Chen, Y. Kikuta, T. Araki, M. Yoneda and Y. Matsuda, "Micro fracture behaviour induced by M-A constituent (island martensite) in simulated welding heat affected zone of H80 high strength low alloyed steel", Acta Metallurgica, Vol. 32, 1984, pp 1779-1788.

[49] Y. Li and T. N. Baker, "Effect of morphology of martensite-austenite phase on fracture of weld heat affected zone in vanadium and niobium microalloyed steels", Materials Science and Technology, Vol. 26, 2010, pp 1029-1040.

[50] Y. Li, N. Crowther, M. J. W. Green, P. S. Mitchell and TN. Baker, "The effect of vanadium and niobium on the properties and microstructure of the intercritically reheated coarse grained heat affected zone in low carbon microalloyed steels", ISIJ International, Vol. 41, 2001, pp 46-55.

[51] D. P. Fairchild, N. V. Bangary, J. Y. Koo, P. L. Harrison and A. Ozekcin, "A study concerning intercritical HAZ microstructure and toughness in HSLA steels", Welding Journal, Vol. 70, 1991, pp 321-329.

[52] H. K. D. H. Bhadeshia and L. E. Svensson, "Modelling the evolution of microstructure in steel weld metal", Eds. Cerjak H & Easterling KE: Mathematical

Modelling of Weld Phenomena, The Institute of Materials, Cambridge, 1993, pp 109–180.

[53] G. Thewlis, “Transformation kinetics of ferrous weld metals”, Materials Science and Technology, Vol. 10, 1994, pp 110-125.

[54] S. Ohkita and Y. Horii, “Recent development in controlling the microstructure and properties of low alloy steel weld metals”, ISIJ International, Vol. 35, 1995, pp 1170-1182.

[55] Z. Zhang and R. A. Farrar, “Role of non-metallic inclusions in formation of acicular ferrite in low alloy weld metals”, Materials Science and Technology, Vol. 12, 1996, pp 237-260.

[56] H. Qiu, H. Mori, M. Enoki and T. Kishi, “Fracture Mechanism and Toughness of the Welding Heat-Affected Zone in Structural Steel under Static and Dynamic Loading”, Metallurgical and Materials Transactions A, Vol. 31, 2000, pp 2785-2791.

[57] C. L. Davis and J.E. King,“Effect of cooling rate on intercritically reheated microstructure and toughness in high strength low alloy steel”, Materials Science and Technology, Vol. 9, 1993, pp 8-15.

[58] W. You, W. Xu, B. Bai and H. Fang, “Materialometrical approach of predicting the austenite formation temperatures”, Materials Science and Engineering A, Vol. 419, 2006, pp 276-282.

[59] KW. Andrews, “Empirical formulae for the calculation of some transformation temperatures”, JISI, Vol. 203, 1965, pp 721-727.

[60] B. C. Kim, S. Lee, N. J. Kim and D. Y. Lee, “Microstructure and local brittle zone phenomena in high-strength low-alloy steel welds”, Metallurgical and Materials Transactions A, Vol. 22, 1991, pp 139-149.

[61] I. Hrivnak, F. Matsuda and K. Ikeuchi, “Investigation of M-A constituent in high strength welds”, Transactions of Japan Welding Institute, Vol. 21, 1992, pp 9-31.

[62] A. Lambert, J. Drillet, A. F. Gourgues, T. Sturel and A. Pineau, “Microstructure of martensite austenite constituents in heat affected zones of high strength low alloy

steel welds in relation to toughness properties", Science and Technology of Welding and Joining, Vol. 5, 2000, pp 168-173.
[63] A. Lambert, X. Garat, T. Sturel, A. F. Gourgues and A. Gingell, "Application of acoustic emission to study of cleavage fracture mechanism in a HSLA steel", Scripta Materialia, Vol. 43, 2000, pp 161-166.
[64] I. Hrivnak, F. Matsuda, Z. Li, K. Ikeuchi and H. Okada, "Investigation of metallography and behavior of M-A constituent in weld HAZ of HSLA steels", Transactions of JWRI., Vol. 21, 1992, pp 241-250.
[65] I. Hrivnak, F. Matsuda, Z. Li and K. Ikeuchi, "Investigation of M-A constituent in High Strength Steel Welds", Transactions of JWRI., Vol. 21, 1992, pp 9-31.
[66] F. Matsuda, K. Ikeuchi, H. Okada, I. Hrivnak and H. Park, "Effect of M-A constituents on fracture behavior of 780 and 980 MPa class HSLA steels subjected to weld HAZ thermal cycles", Transactions of JWRI., Vol. 23, 1994, pp 231-238.
[67] K. Ohya, J. Kim, K. Yokoyama and M. Nagumo, "Microstructures relevant to brittle fracture initiation at the heat affected zone of weldment of a low carbon steel", Metallurgical and Materials Transactions A, Vol. 27, 1996, pp 2574- 2582.
[68] F. Matsuda, Z. Li, P. Bernasovsky, K. Ishihara and H. Okada, "An investigation on the behaviour of the M-A constituent in simulated HAZ of HSLA steels" Welding in the World, Vol. 29, 1991, pp 307-313.
[69] S. Moeinifar, A. Hossein Kokabi and H. Madaah Hosseini, "Effect of tandem submerged arc welding process and parameters of Gleeble simulator thermal cycles on properties of the intercritically reheated heat affected zone", Materials and Design, Vol. 32, 2011, pp 869-876.
[70] T. Haze and S. Aihara, "Influence of toughness and size of local brittle zone on HAZ toughness of HSLA steels", Proc. 7th International Conference on Offshore Mechanics and Arctic Engineering, Houston, Texas, 7-12 February 1988. Eds. Salama M. et al. U.S.A. The American Society of Mechanical Engineers (ASME), Vol. III., pp 515-523.
[71] F. Matsuda, Y. Fukuda, H. Okada, C. Shiga, K. Ikeuchi, Y. Horii, T. Shiwaku and S. Suzuki S, "Review of mechanical and metallurgical investigations of

martensite-austenite constituent in welded joints in Japan", Welding in the World, Vol. 37, 1996, pp 134-154.
[72] D. Tian, "Microstructure, cleavage fracture and toughness of granular bainite in simulated coarse-grained heat-affected zones of low-carbon high-strength steels", Doctoral Thesis, Department of Mechanical Engineering, University of Oulu, Finland. Acta Universitas of Ouluensis C Technica 113, 1998.
[73] P. L. Harrison and S. E. Webster, "HAZ microstructure and toughness in single pass welds", The 36th Mechanical Working and Steel Processing Conference, Baltimore, Maryland, USA, 1994, pp 551-559.
[74] G. M. Evans, "Affect of nitrogen on C-Mn steel welds containing titanium and boron", Welding Journal, Vol. 77, 1998, pp 239-248.
[75] H. Mabuchi and H. Nakao, "The effects of excess aluminium on mechanical properties of Mn-Mo, Mn-Mo-Ni and Mn-Mo-Ni-Cr with regard to solute interactions", Transactions of ISIJ, Vol. 23, 1983, pp 504-512.
[76] C. Li, Y. Wang, T. Han, B. Han and L. Li, " Microstructure and toughness of coarse grain heat-affected zone of domestic X70 pipeline steel during in-service welding", Journal of Material Science, Vol. 46, 2011, pp 727-733.
[77] I. Hrivnak, "Weldability of modern steel materials", ISIJ International, Vol. 35, 1995, pp 1148-1156.
[78] A. Lambert, A. F. Gourgues, T. Sturel and A. Pineau, "Fracture toughness of simulated HAZ in HSLA steel welds", EUROMAT 2000 Conference on Advanced in Mechanical Behaviour, Plasticity and Damage, 7-9 Nov 2000, Tours, France. Eds. Miannay D., Costa P., François D. & Pineau A., Elsevier. pp 97-102.
[79] OM. Akselsen, Ø. Grong and G. Rorvik, Scand. J. Metall., Vol. 19, 1990, pp 258-264.
[80] C.L. Davis and J.E. King, "Cleavage initiation in the intercritically reheated coarse grained heat affected zone: Part I. Fractographic evidence" Metallurgical and Materials Transactions A, Vol. 25, 1994, 563- 573.
[81] Y. Li, DN. Crowther, MJW. Green, PS. Mitchell and TN. Baker, "The effect of vanadium and niobium on properties and microstructure of intercritically reheated

coarse grained heat affected zone in low carbon microalloyed steels", ISIJ International, Vol. 41, 2001, pp 46-55.

[82] K. S. Kweon, J. H. Kim, J. H. Hong and C. H. Lee, "Microstructure and toughness of intercritically reheated heat affected zone in reactor pressure vessel steel weld", Science and Technology of Welding and Joining, Vol. 5, 2000, pp 161-167.

[83] A. F. Gourgues, H. M. Flower and T. C. Lindley, "Electron backscattering diffraction study of acicular ferrite, bainite and martensite steel microstructure", Materials Science and Technology, Vol. 16, 2000, pp 26-40.

[84] Ø. Grong, "Metallurgical modelling of welding", Materials modelling Series. Ed. Bhadeshia H.K.D. The Institute of Materials, Cambridge, 1994.

[85] J. F. Knott, "Fundamentals of fracture mechanics", John Wiley and Sons, 1973.

[86] L. Reimer, U. Heilers and G. Salinger, Scanning, 1986, Vol. 8, pp. 101.

[87] V. Randle and P. Davies, "Crystallography of brittle fracture and deformation twinning in ferritic steels", Materials Science and Technology, Vol. 21, 2005, pp 1275-1281.

[88] V. Randle and O. Engler, "An introduction to texture analysis", Gordon and Breach, Amsterdam, 2000.

[89] V. Randle, "Crystallographic analysis of facets using electron backscatter diffraction", Journal of Microscopy, Vol. 195, 1999, pp 226-232.

[90] A. Kumar, A. J. Wilkinson and S. G. Roberts, "Quasi-cleavage fracture planes in spheroidized A533B steel", Journal of Microscopy, Vol. 227, 2007, pp 248-253.

[91] V. Randle and C. Hoile, "Crystallographic analysis of facets using electron back-scatter diffraction", Materials Science Forum, Vol. 273, 1998, pp 183-190.

[92] M. Libert, C. Rey, L. Vincent and B. Marini, "Temperature dependant polycrystal model application to bainitic steel behavior under tri-axial loading in the ductile–brittle transition" International Journal of Solids and Structures, Vol. 48, 2011, pp 2196-2208.

[93] V. Vitek, M. Mroveca and J. L. Bassani, "Influence of non-glide stresses on plastic flow: from atomistic to continuum modeling", Materials Science and Engineering A, Vol. 365, 2004, pp 31-37.

[94] P. Villechaise, L. Sabatier and J. C. Girard, “On slip band features and crack initiation in fatigued 316L austenitic stainless steel: Part 1: Analysis by electron back-scattered diffraction and atomic force microscopy”, Materials Science and Engineering A, Vol. 323, 2002, pp 377-385.

[95] A. El Bartali, V. Aubin, L. Sabatier, P. Villechaise and S. Degallaix-Moreuila, “Identification and analysis of slip systems activated during low-cycle fatigue in a duplex stainless steel”, Scripta Materilia. Vol. 59, 2008, pp 1231-1234.

[96] F. S. Lepera, “Improved etching technique for the determination of percent martensite in high strength dual phase steels”, Metallography, Vol. 12, 1979, pp 263-268.

Papers and Manuscripts

Paper 1

Investigation of the mechanism of cleavage fracture initiation in the intercritically coarse grained heat affected zone of an HSLA steel.

Materials Science and Technology, In Press,
DOI: 10.1179/1743284712Y.0000000056

Investigation of the mechanism of cleavage fracture initiation in the intercritically coarse grained heat affected zone of an HSLA steel

P. Mohseni[a], JK. Solberg[a], M. Karlsen[a, c], OM. Akselsen [a, b], E. Østby[b]

[a] *Department of Material Science and Engineering, Norwegian University of Science and Technology(NTNU), Trondheim, Norway*

[b] *Department of Applied Mechanics and Corrosion, SINTEF, Trondheim, Norway*

[c] *Statoil ASA, Trondheim, Norway*

Abstract:

The degradation of the fracture toughness of HSLA steels is attributed to the formation of "local brittle zones" in the welded joint. These local brittle zones are mainly located within the coarse grained heat affected zone (CGHAZ) and the intercritically reheated coarse grained HAZ (ICCGHAZ). Cracking of M-A constituents and debonding of M-A constituent from the surrounding matrix are generally accepted as initiation events of fracture in the ICCGHAZ. In the present work, the low temperature fracture toughness of X80 pipeline steel was examined. The main purpose was to (i) evaluate possible crack initiation sites of cleavage fracture and (ii) to identify the mechanism by which M-A constituents deteriorate the ICCGHAZ toughness.

The results revealed that the microstructure of ICCGHAZ contained blocky M-A constituents along prior austenite grain boundaries. Finally, it was shown that fracture initiation occurred preferentially at M-A constituents by a debonding mechanism rather than cracking of the M-A constituents.

Keywords: Intercritically reheated coarse grained heat affected zone, M-A constituent, weld simulated HAZ, X80 pipeline steel.

Introduction:

High-strength low alloy steels (HSLA) with yield strength higher than 550MPa have been increasingly used for high pressure pipeline operation and offshore structural installation. The installation of pipelines used for transporting oil and gas is sometimes taking place in severe environments such as in the Arctic region, where the pipelines must have low temperature toughness.[1] Thus, the major motivation for the improvement of HSLA steels has been provided by the demand for higher strength, as well as improved toughness, ductility and weldability at low temperatures.[2, 3]

HSLA steels combine excellent tensile strength and ductile to brittle transition (DBT) properties. However, the balance of high strength and toughness can be deteriorated by welding thermal cycles; producing local poor toughness in the welded joints.[4] The heat affected zone (HAZ) is in many cases considered to be the most critical part of a weld.[5]

The region of lowest toughness after single pass welding is the coarse grained heat affected zone (CGHAZ). The main reason for this is attributed to the formation of unfavourable microstructures such as coarse ferrite side plates (upper bainite and widmanstätten ferrite).[6] During multipass welding, the intercritically reheated coarse grained HAZ (ICCGHAZ) is formed by reheating the CGHAZ into the mixed austenite and ferrite region (between A_{c1} and A_{c3}). Thus, parts of the microstructure were transformed into austenite, which nucleated and grew preferentially along the prior austenite grain boundaries and bainite lath boundaries.[7] These austenite islands became enriched in carbon due to the high diffusivity of carbon in ferrite and its high solubility in austenite, and they transformed to hard and brittle M-A constituents during the subsequent cooling stage, [5] leaving a necklace type of M-A distribution along prior austenite grain boundaries.[10]

The ICCGHAZ formed during multipass welding may have even lower toughness than the CGHAZ. It seems that the formation of M-A constituents along prior austenite grain boundaries is the most important reason for the loss in toughness.[5, 8, 9] With respect to the shape of the M-A constituents, they can be classified into two main types: (i) elongated (or stringer like) M-A constituents with L/W>3, and (ii) massive (or blocky) M-A constituents with L/W<3 (L: length, W: width). It has been reported that massive M-A constituents deteriorate the low temperature toughness of ICCGHAZ seriously.[11, 12]

Four possible fracture mechanisms have been proposed in the literature to explain cleavage initiated by M-A constituents: [7, 9, 16]

(1) The M-A constituent is a brittle phase and cracks readily. This microcrack initiates cleavage in the ferrite matrix.

Previous works have shown that the M-A constituents can act as initiation sites for cracks and also promote their propagation.[4, 13] At low temperatures the blocky M-A constituents increase the matrix stresses close to the interface between the M-A constituents and the matrix, and may cause cleavage crack initiation.[14] Stringer type M-A constituents have been shown to crack readily and provide no effective obstacle to crack propagation.[6]

(2) Transformation-induced residual tensile stresses are produced in the surrounding ferrite matrix, assisting cleavage fracture.

Austenite forms at prior austenite grain boundaries and transforms to M-A constituents during cooling. The volume expansion related to this transformation results in elastic and plastic stress concentrations in the surrounding matrix, assisting cleavage fracture. In the case of the closely spaced blocky M-A constituents, the stress and strain concentrations will be magnified because the transformation induced stress fields overlap.

(3) The M-A has a higher hardness than the surrounding ferrite and causes a stress concentration in the neighbouring ferrite matrix. This stress concentration assists cleavage fracture.

The hardness of the M-A constituents is significantly higher than that of the surrounding matrix, and during deformation the stress concentration increases due to this hardness difference. During loading, the matrix will start to deform plastically and an internal stress can be generated in the matrix close to the M-A constituents. A large stress will develop across the interface and may cause the M-A constituents to debond from the matrix.[7, 13, 16] In addition, it has been suggested that the M-A constituent/matrix interface may be weakened by carbon segregation.[17]

(4) A microcrack that is formed at the M-A/matrix interface through interface decohesion can initiate fracture through interfacial decohesion that propagates either in a brittle manner or via linking with other debonded regions.

The main purpose of this paper is to reveal the mechanism by which M-A constituents deteriorate the HAZ toughness. Brittle fracture crack initiation and propagation in the ICCGHAZ of the arctic steel X80 are examined. By analysing the fracture mechanisms, the effect of M-A constituents on the fracture toughness will be investigated.

Experimental procedure

A commercial grade of API X80 pipeline steel with the chemical composition given in Table 1 was selected for the present study.

Table 1 Chemical Composition of the steel (mass %) [1]

C	Si	Mn	P	S	Cr	Cu	Ni	Mo
0.06	0.08	1.79	0.012	0.004	0.12	0.28	0.16	0.15

[1] With 0.044%Nb, 0.013%Ti and 0.028%Al.

To simulate ICCGHAZ microstructures, specimens of dimensions 11x11x100 mm^3 were cut with the longest dimension along the rolling direction and subjected to thermal cycles simulating double pass welding, applying a Smitweld TCS1405 weld simulator.

During the first cycle the specimen was heated to 1350°C followed by cooling at a rate corresponding to a cooling time between 800°C and 500°C ($\Delta t_{8/5}$) of 15 seconds. The second heating cycle had a peak temperature, T_{p2}, of 780°C, and the cooling rate was the same as during the first cycle (Table 2).

Table 2 The thermal cycle for the simulation of HAZ

First peak T_{P1} (°C)	1350
Cooling time $\Delta t_{8/5}$ (s)	15
Second peak T_{p2} (°C)	780
Cooling time $\Delta t_{8/5}$ (s)	15

After the HAZ simulation, Crack Tip Opening Displacement (CTOD) specimens were machined with a 5 mm deep through width notch cut into the sample and subjected to CTOD testing at 0,-30,-60 and -90 ºC. The microstructures of the ICCGHAZ were examined by optical microscopy with a Leica MEF4M and by scanning electron microscopy. Samples for light microscopy were mechanically prepared by conventional grinding and polishing techniques and etched by a Lepera solution (mixture of 4% Picral and 1gr Sodiumtiosulphate ($Na_2S_2O_3$) in 100ml distilled water in a 1:1 ratio) [18], which make the M-A constituents appear white. A Zeiss Supra 55VP low vacuum field emission scanning electron microscope (LVFESEM) was used to observe the fracture surfaces and microstructures (operated at 20kV, 82µA and 30µm aperture size). In order to obtain information about the chemical composition of second phase particles, energy dispersive X-ray spectroscopy (EDS) was performed with an EDAX Genesis spectrometer interfaced with the SEM microscope. In addition, the carbon concentration of the blocky M-A constituents was studied by wavelength dispersive spectroscopy (WDS) in a Jeol

JXA-8500 electron probe micro-analyzer (EPMA), operated at 10 kV, 50nA in spot mode. A LDE6H crystal was used for this measurement.

For detailed analysis of the microstructure, Transmission Electron Microscopy (TEM) was carried out on thin samples from the ICCGHAZ region. The thin samples were prepared from the fractured CTOD specimens by using the Focus Ion Beam (FIB) technique, applying a HELIOS NANOLAB 600 from FEI. The FIB thinning process of the sample included two steps: (i) Thinning with ion beams (30 kV), starting with high currents, 460 pA, that successively was reduced to 50 pA. (ii) Final thinning with a box pattern with ions at 5 kV and 16 pA (approximately 1.5 minutes at each side) to eliminate all damage produced by FIB. The TEM observations were performed in a conventional JEOL-JEM 2010 microscope at 200 kV operating voltage.

The hardness of the M-A constituents and the neighbouring base metal was measured by a nanoindentation technique applying a Hysitron TI 750 UbiTM instrument with a performechTM control unit scanning nanoindentation system. The measurements were performed within the ICCGHAZ region (80μm x 80μm) of the sample after polishing and etching by Lepera solution; the step size being 4μm. The Vickers microhardness was also measured by using 5gf (gram force) load in a Leica VMHTMOT instrument. In both cases the indents were small enough (approximately 4μm in diameter in the Leica) to predominantly sample either the M-A constituent or the matrix.

Results and Discussion:

Microstructure evaluation

The microstructures of the base metal and the simulated ICCGHAZ are shown in Fig. 1 and Fig. 2, respectively. The acicular ferritic microstructure of the base metal had transformed to upper bainite with a large prior austenite grain size during the

weld thermal cycles. In Fig. 2 the prior austenite grain boundaries are decorated by a white phase that is also seen within the grains as smaller particles. The upper bainite is not revealed due to the special colour etchant (Lepera) that was used.

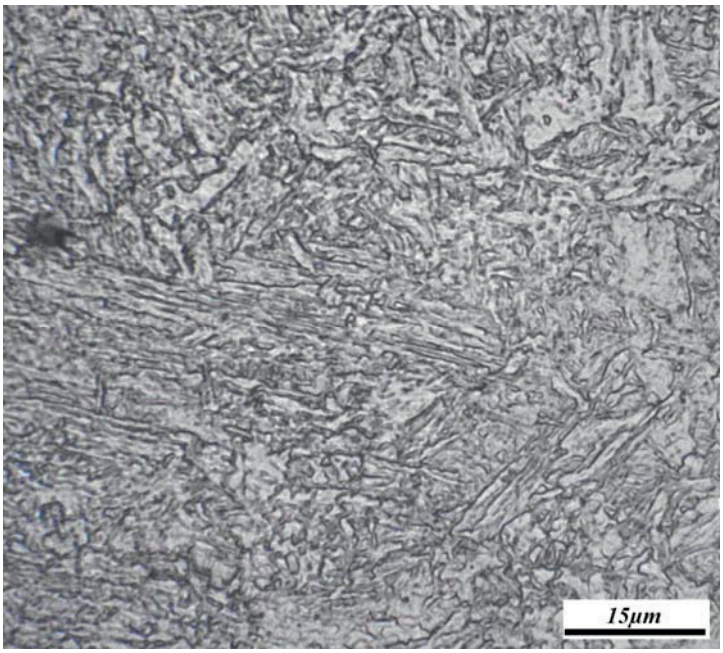

Fig. 1. *Microstructure of base metal.*

As mentioned in the experimental procedure section, the blocky like M-A constituents can be revealed as a white phase by using the Lepera solution as an etchant.[18] Davis and King have also observed a case where the M-A constituents of the steel were shown as a white phase using the Lepera etchant.[16] In the present work, blocky white particles can be seen in the microstructure of the simulated ICCGHAZ after etching by Lepera solution. These particles are shown in Fig. 2, indicated by arrows. It is seen that they are formed either along prior austenite grain boundaries (arrows number 1 and 2) or inside the grains (arrows number 3 and 4). According to earlier observations reported in the literature, [16] it is reasonable to assume that these white particles are M-A constituents. They will therefore be called M-A constituents in the continuation of this work.

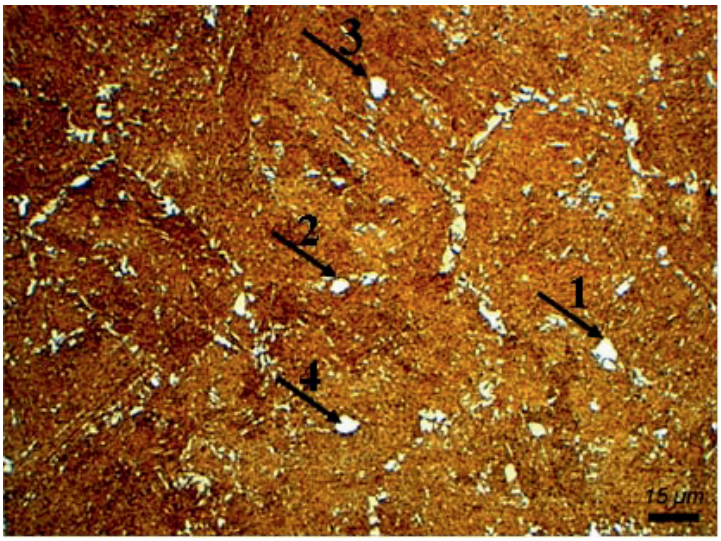

Fig. 2. *Optical microstructure of ICCGHAZ, M-A constituents indicated by arrow, Lepera etchant.*

The microstructure of the ICCGHAZ was also examined by FE SEM, see Fig 3. The prior austenite grain boundaries can be observed clearly in this figure. Two main types of M-A constituents are identified in Fig 3a-c. The blocky M-A constituents that are located at the prior austenite grain boundaries (arrows number 1 and 2) or inside the grains (arrow number 3) have a diameter of 3 to 5µm, while the elongated M-A stringers (arrow number 4), formed between bainite and martensite laths, are approximately 0.2 to 1µm in width and 5-10 µm in length. In Fig. 3d, the blocky M-A constituents form a necklace-like structure that is located at prior austenite grain boundaries in a nearly connected network (arrows number 5 and 6). Li and Baker have also observed a case where the M-A constituents along the prior austenite grain boundaries were connected or nearly connected.[7]

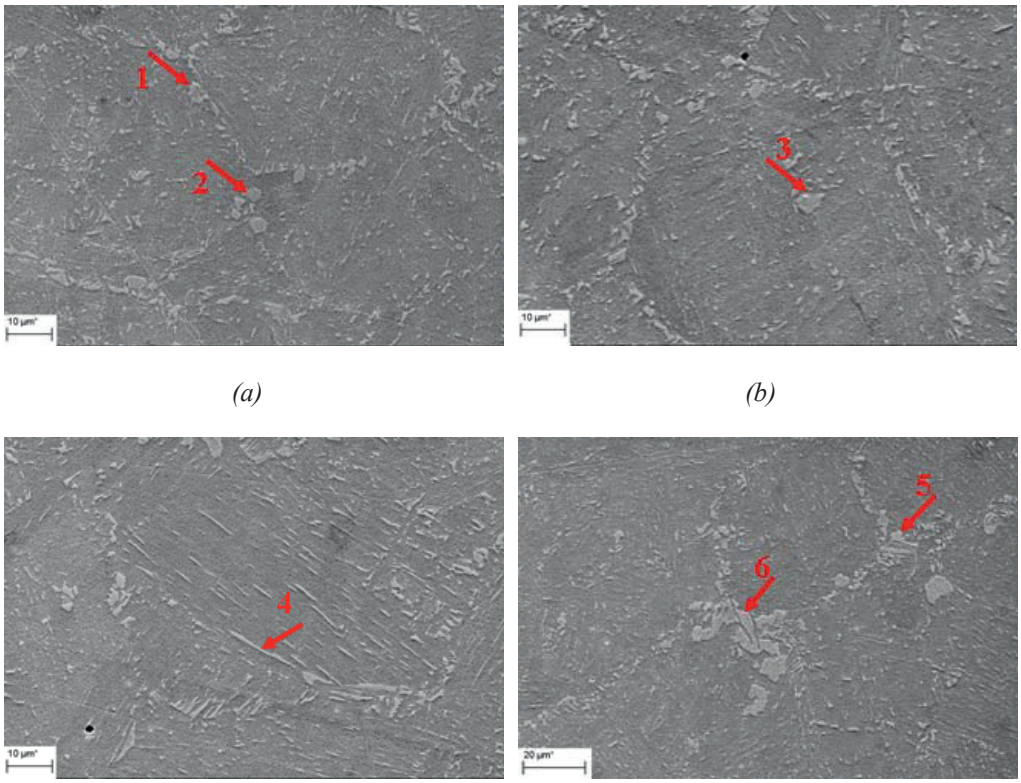

(a) *(b)*

(c) *(d)*

Fig. 3. *FE SEM micrographs from the weld simulated ICCGHAZ region.*

The obtained fracture toughness (CTOD) values as a function of test temperature are presented in Fig. 4. It can be seen that the CTOD value increases with increasing test temperature; the lower and upper parts are associated with brittle and ductile fracture, respectively.

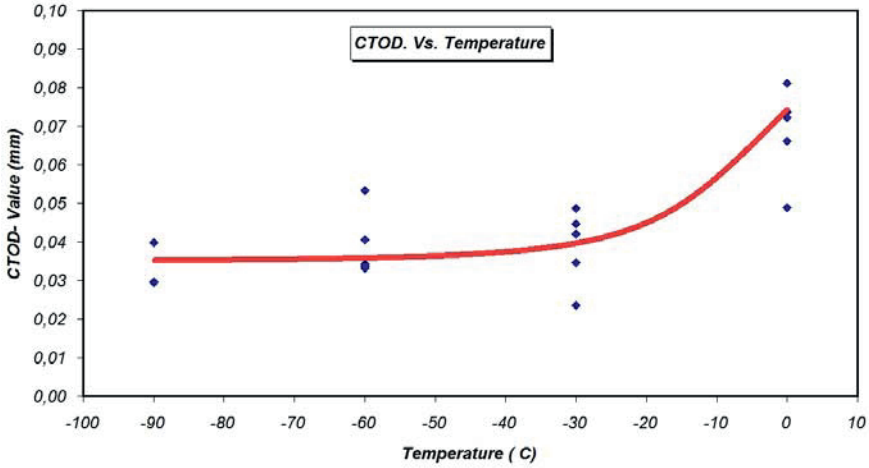

Fig. 4. *The variation of CTOD value with test temperature.*

Hardness and EPMA analysis

The mechanical properties of steel are highly related to its microstructure, the matrix phase, and the distribution of secondary phases or particles therein. Nanomechanical testing has been increasingly used to provide a simple quantitative characterization of such phases. One of the first and reliable applications of this method has been to measure local hardness variations within microstructure features. Fig. 5 shows a SEM micrograph of the area within the ICCGHAZ that was selected to measure local hardness variations by nanomechanical testing. The corresponding hardness mapping (Fig. 5b) shows that the hardness values of the M-A constituents are significantly higher than those of the neighbouring matrix. It can be seen that the hardness of the blocky M-A constituents and the matrix was in the range 600-1200Hv (pink and white areas) and 300-500Hv (Black area), respectively.

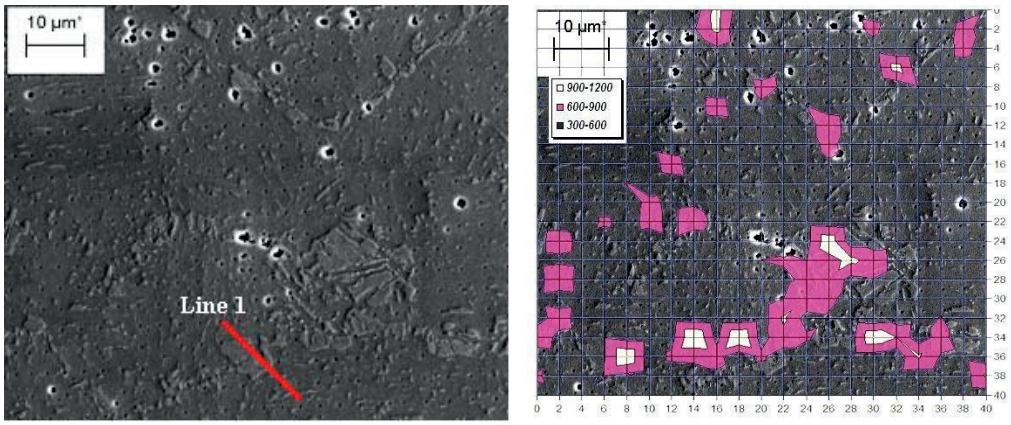

(a) *(b)*

Fig. 5. *(a) SEM micrograph of a grid of nanoindents superimposed on an M-A constituent in ICCGHAZ. (b) Corresponding hardness mapping indicates that the M-A constituents are locally harder than the matrix.*

In addition, the hardness of 50 M-A constituents within ICCGHAZ was measured by the Vickers microhardness method with a 5gf (gram force) load. The obtained hardness values are given in Table 3.

Table 3 Vickers Microhardness values of M-A Constituent in ICCGHAZ (Hv).

716	918	719	884	604
896	744	669	716	615
790	605	728	603	615
931	815	610	684	860
695	635	709	727	880
719	923	779	767	608
601	707	693	692	695
748	673	922	873	847
623	627	731	697	753
675	836	678	691	786

The hardness of blocky and elongated M-A constituents has earlier been reported to be in the range 800-1200Hv and 600-800Hv, respectively.[17] The hardness values obtained in the present investigation (Table 3) are at a similar level (600-1000Hv). It can be seen that, in general, the blocky M-A constituents have significantly higher hardness values than the bainite matrix, indicating that they have high carbon content.

The strength and hardness of M-A constituents have earlier been shown to be related to their carbon content in a nearly linear manner, [17] with carbon content within the range of 0.6-1.1 wt%.[14, 15] In the present work, the carbon concentration of M-A constituents was measured by EPMA line scan analysis (1 μm step length), choosing particles from the same area as that analysed by nanoindentation (Fig. 5a). An example of a line scan analysis along line 1 in Fig. 5a is illustrated in Fig. 6. This figure shows that the level of carbon is divided into three regions along this line. Regions number 1 and 3 illustrate the carbon content in the matrix of this steel which contains 0.06% (Table 1). The carbon content of the M-A constituent was measured relative to the matrix (region 2). It can be seen that the carbon content in the M-A constituent was significantly higher than in the matrix and was identified to be around 0.75 wt%. It can be concluded that the higher hardness values and the higher carbon content of the particles strongly strengthen the assumption that they really are M-A constituents.

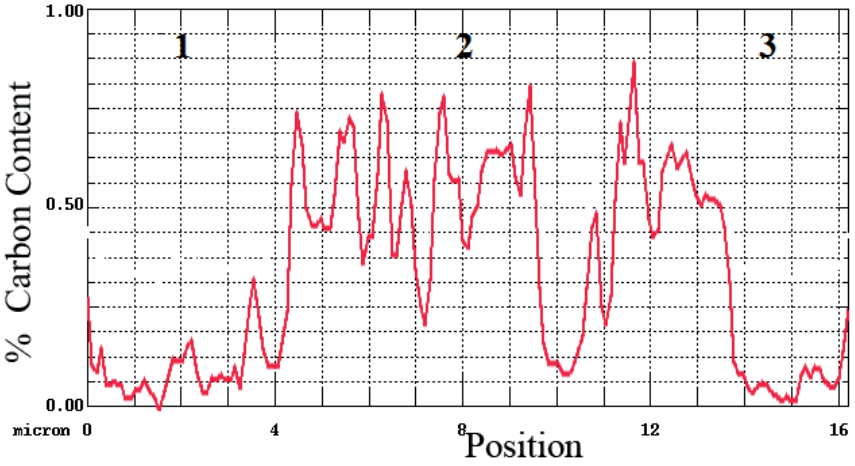

Fig. 6. *EPMA line scan analysis from the M-A constituent in ICCGHAZ.*

Fractography

Detailed fractographic examination was carried out on the CTOD samples with the purpose of classifying and evaluating possible cleavage crack initiation sites and microstructural features in the vicinity of these. An example of a cleavage initiation site is shown in Fig. 7, for test temperatures of 0ºC (Fig.7 a-b) and -90ºC (Fig.7 c-d). It can be seen that the particles have the smooth and blocky appearance typical of M-A constituents. These particles also correspond in morphology and size to M-A constituents. The typical riverline patterns indicate that these particles are the initiation points of the cleavage cracks (Fig.7 a-c, arrows 1 and 3). The matching fracture surfaces show holes corresponding to the locations where the particles have been located and pulled out (Fig.7 b-d, arrows 2 and 4). These features are identical to those reported by Davis and King.[16]

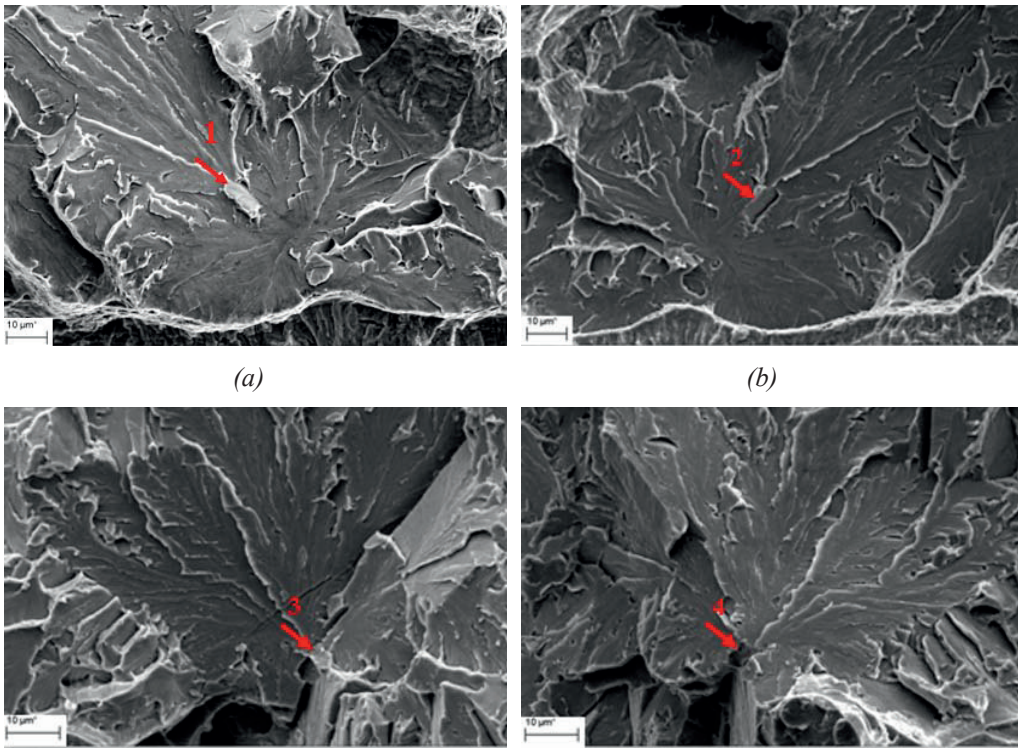

(a) *(b)*

(c) *(d)*

Fig. 7. *Fracture surfaces of the specimens tested at different temperature, (a) and (b) 0°C, (c) and (d) -90°C.*

The results of EDS analyses from the matrix and the particles are presented in Fig. 8 (same test conditions). As can be seen, there was no detectable compositional difference between these blocky features on the fracture surface and the matrix, which clearly indicates that they are not inclusions. In accordance with other published work, [3] these observations demonstrate that the brittle fracture initiation occurs at blocky M-A constituents formed on prior austenite grain boundaries during the second thermal cycle. The fracture mechanism appears to be debonding between the M-A particle and the surrounding bainite matrix.

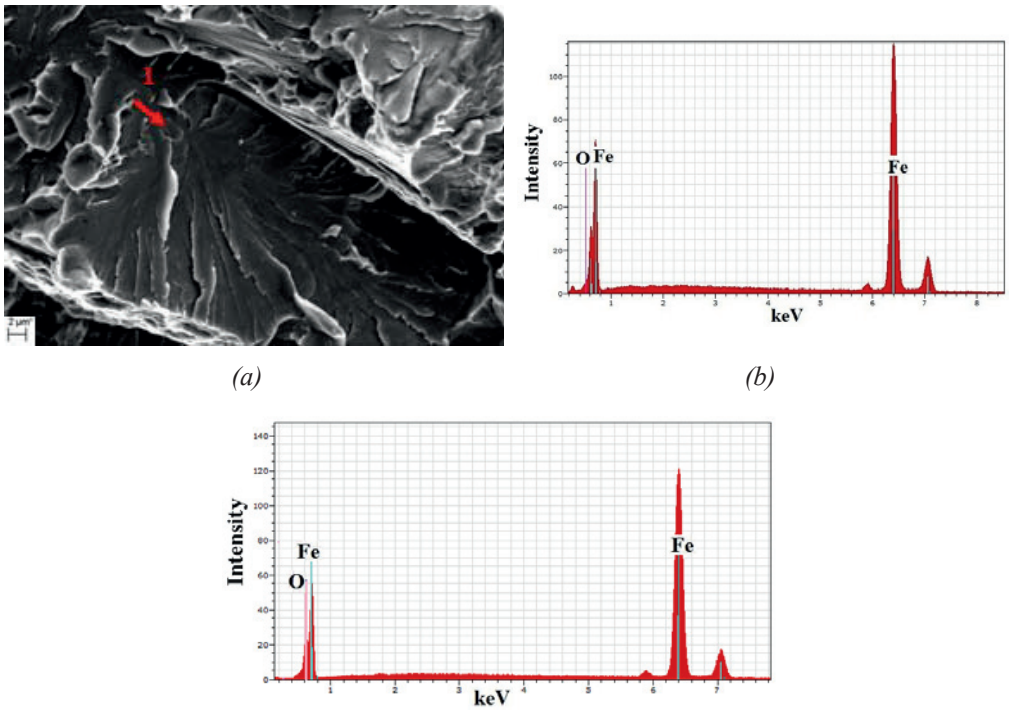

Fig. 8. *(a) Fracture surface of the specimen at -30ºC (b) EDS analysis of particle (c) EDS analysis of matrix.*

In general, the initiation sites are found from the river line pattern radiating from each single initiation point. However, in some cases, mainly in the lath-like microstructure, the river pattern was rather diffuse, thus making identification of the initiation site difficult. A cleavage crack can be initiated from the area between two nearby M-A constituents. Davis and King observed a case where a necklace distribution of M-A constituents along prior austenite grain boundaries was associated with low impact toughness. [16] They argued that the overlap of residual phase transformation stresses and stress concentrations due to debonding of M-A constituents are of importance for the brittle fracture initiation. In the present work, Fig. 9 shows a similar case in the fracture surface of the sample tested at -60ºC. The figure shows an example of re-initiation occurring in the region between several blocky M-A constituents, indicated by arrows 2, 3 and 4. The region between the

debonded M-A constituents has probably been constrained due to high local stresses which can cause a microcrack to form. This microcrack has then propagated through the grain.

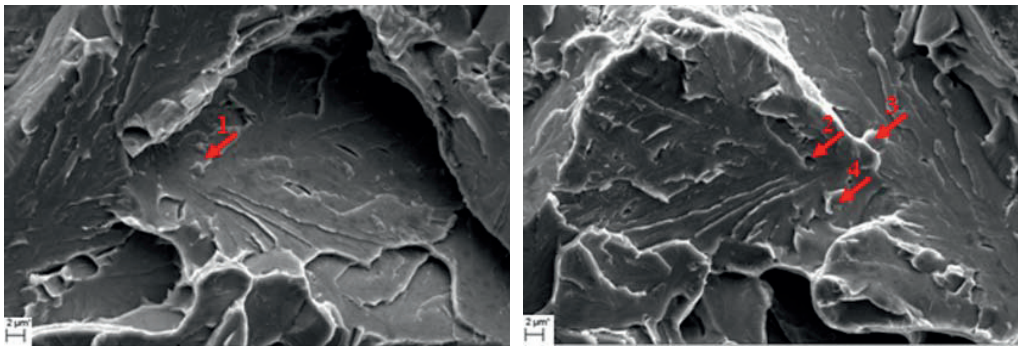

Fig. 9. *Opposite fracture surfaces of the specimen CTOD tested at -60ºC.*

A more detailed examination of the fracture surfaces revealed also the existence of non-metallic inclusions within same cleavage facets. As can be seen in Fig. 10, the particle indicated by arrow 1 may have acted as an initiation site (CTOD sample tested at -60ºC). An EDS point analysis revealed that the inclusion is an aluminium oxide, Fig. 10b.

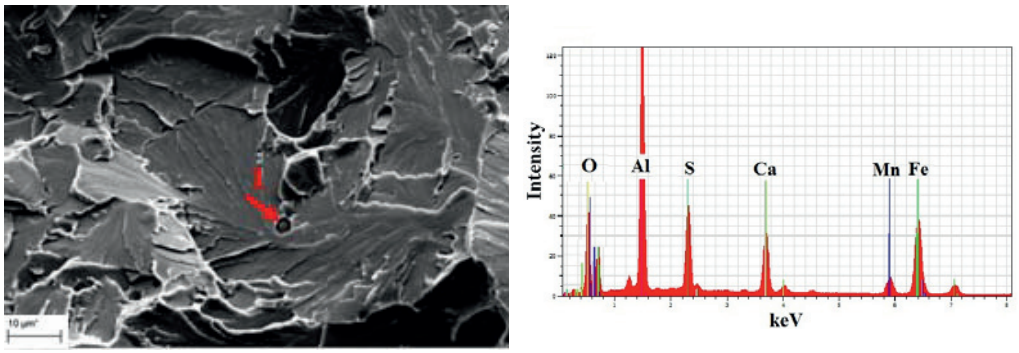

(a) *(b)*

Fig. 10. *(a) Fracture surface of the specimen tested at -60ºC, (b) EDS analysis of the inclusion.*

In the present investigation, also transmission electron microscopy was employed to identify these particles. Fig. 11 shows bright field and dark field images of the particle which is marked with an arrow in Fig. 7a. The bright field image in Fig. 11a shows that the particle is composed of twinned martensite. A selected area diffraction pattern (SADP) from a volume including this twinned martensite region is shown in Fig. 11d. These two spots indexed 110_{t1} and 200_{t2} are from the two twin orientations, respectively. The dark field images of Fig. 11b and 11c were recorded from twin spots 110_{t1} and 200_{t2}, respectively. As can be seen, these images show opposite twin contrast. Twinned martensite is generally associated with high carbon martensite due to a significant enrichment of carbon in the austenite. In total, this TEM observation, together with the previous results, proves that the particles located at cleavage crack initiation sites are M-A constituents.

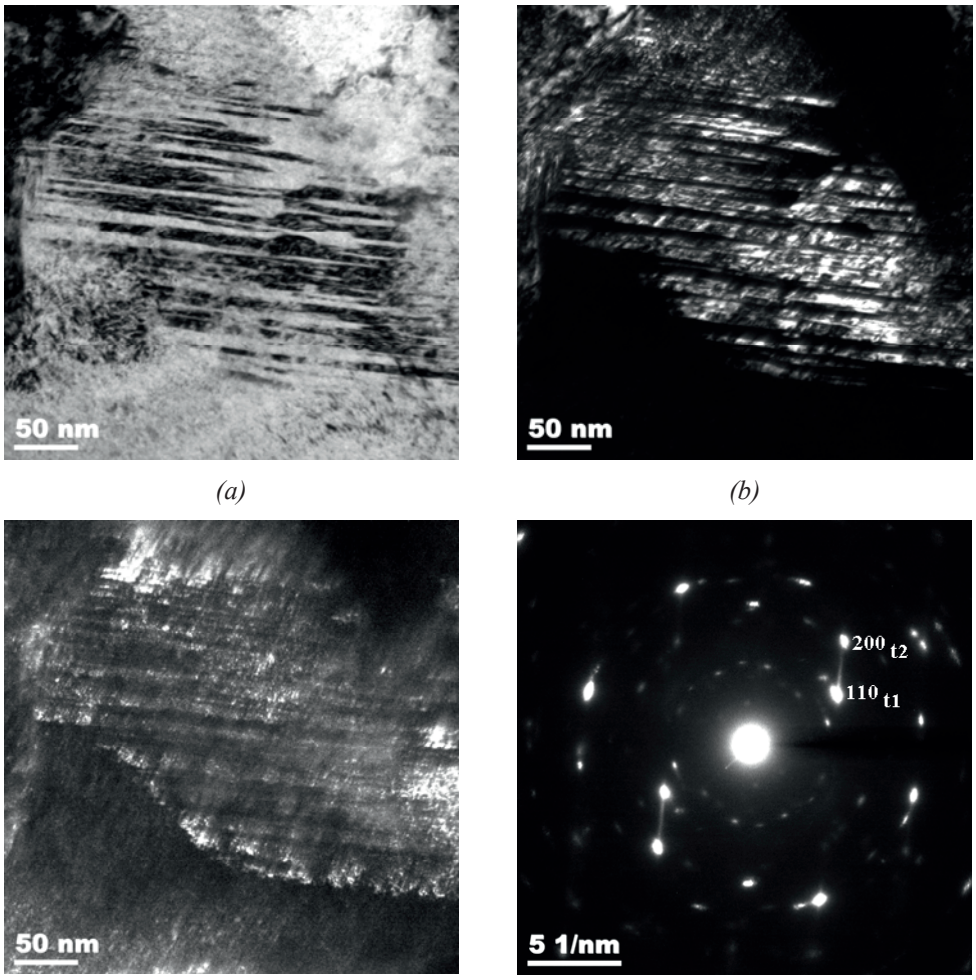

(a) *(b)*

(c) *(d)*

Fig. 11. *(a), (b) and (c), show bright field and dark field micrographs of twinned martensite, (d) selected area diffraction pattern (SADP) of twin region. The dark-field images were obtained by using the indexed spots marked t_1 and t_2 in the SAD pattern (c)*

The mechanisms of crack initiation caused by the presence of M-A constituents are generally proposed to be the concentration and triaxiality of internal stresses close to the interface between the M-A constituents and the matrix. Two main different initiation sites of fracture in HSLA steels subjected to ICCGHAZ weld simulation have been reported: 1- debonding of the M-A constituent/matrix interface, 2- cracking of the M-A constituent.[14, 15] However, in the majority of cases the fracture

facets had initiated preferentially from the M-A constituents that debonded rather than cracked. During the present investigation, the blocky M-A constituents were not observed to crack, and this was also the case in the work of Davis and King.[16, 19] The main reason for that might be auto-tempering of the M-A constituents during cooling from the intercritical peak temperature and by that a recovering of the steel toughness. [7] Instead debonding occurs; increasing the matrix stresses due to stress concentration effects in regions between closely spaced M-A constituents, assisting cleavage fracture.

In the present work, Fig. 5 (hardness mapping) shows a high level of local hardness in the M-A constituents with respect to that in the surrounding matrix. Therefore, an excessive internal stress could have developed in the matrix close to the M-A constituents and across the interface between the M-A constituents and the matrix. These stress concentrations may have caused the M-A constituents to debond from the neighbouring matrix.

Fig. 7 gives an example of debonding of M-A constituent from the surrounding matrix, initiating a cleavage fracture. Fig. 9 shows a similar case where the stress and strain concentrations probably have magnified because the transformation induced stress fields have overlapped. The crack seems to have initiated in the volume between the closely spaced M-A constituents and has propagated through the grain.

In summary, for cracks initiated from M-A constituents, mechanisms 2 and 3 of the introductory section, i.e. transformation-induced residual tensile stress and debonding, seem to have been the dominating initiation mechanisms in the present investigation. The detrimental effect of the stress build up depends on the presence of two or more M-A constituents in close proximity.

Conclusions

In the present investigation, the embrittlement mechanisms of M-A constituents formed in the weld heat affected zone in an Arctic steel have been examined, using CTOD testing of weld thermally simulated ICCGHAZ samples. The main results are as follows:

1- Two main types of M-A constituents were identified by SEM: blocky M-A constituents formed along prior austenite grain boundaries, and elongated stringers, developed between bainite and martensite laths. The specific situations of connected or nearly connected M–A constituents were also observed.

2- Hardness measurements performed by Vickers indentation and nanoindentation showed that the hardness of the M-A constituents was significantly higher than that of the matrix. The hardness value of the M-A constituents was in the range of 600-1000 Hv.

3- The carbon concentration of the M-A constituents was measured by EPMA quantitative analysis. The results from the EPMA analysis showed that the carbon content of the M-A constituents was significantly higher than the carbon content in the matrix (within the range of 0.6-1.1%).

4- Detailed TEM analysis revealed the presence of twinned martensite inside particles that are located at initiation sites of cleavage facets, proving that they are M-A constituents, and thus that M-A constituents are potential initiation sites for cleavage cracks.

5- In this investigation, cracks initiated either from debonded M-A constituents or from the region between two or more, closely separated blocky M-A constituents.

Acknowledgements

The authors wish to thank the Research Council of Norway for funding through the Petromaks Programme. The financial support from ENI, Statoil, Total, Scana Steel Stavanger, JFE Steel Corporation, Nippon Steel Corporation, Brück Pipeconnections, Miras Grotnes, Bredero Shaw, Trelleborg, GE Oil and Gas, Aker Solutions and Technip is also acknowledged.

References

1. W.W. Bose-Filho, A.L.M. Carvalho and M. Strangwood: Mater. Charact., 2007, 58, 29-39.
2. S.K. Das, S. Sivaprasad, S. Das, S. Chatterjee and S. Tarafder: Mater. Sci. Eng., 2006, 431A, 68-79.
3. W.W. Bose Filho, A.L.M. Carvalho and P. Bowen: Mater. Sci. Eng., 2007, 460–461A, 436–452.
4. A. Lambert-Perlade, A.F. Gourgues, J. Besson, T. Sturel and A. Pineau: Metall. Mater. Trans., 2004, 35A, 1039-1053.
5. S. Moeinifar, A.H. Kokabi and H.R. Madaah Hosseini: Mater. Des., 2010, 31, 2948–2955.
6. H. Qiu, H. Mori, M. Enoki and T. Kishi: Metall. Mater. Trans., 2000, 31A, 2785-2791.
7. Y. Li and T.N. Baker: Mater. Sci. Technol., 2010, 26, 1029-1040.
8. OM. Akselsen, Ø. Grong and JK. Solberg: Scand. J. Metall., 1988, 17, 194-200.
9. OM. Akselsen, Ø. Grong and G. Rorvik: Scand. J. Metall., 1990, 19, 258-264.
10. R. Laitinen: 'Improvement of weld haz toughness at low heat input by controlling the distribution of M-A constituents', Acta Univ. Oulu. C234, University of Oulu, Finland, 2006.
11. F. Matsuda, K. Ikeuchi, H. Okada, I. Hrivnak and H. Park: Trans. of JWRI., 1994, 23, 231-238.
12. K. Ohya, J, Kim, K. Yokoyama and M. Nagumo: Metall. Mater. Trans., 1996, 27A, 2574- 2582.
13. J.H. Chen, Y. Kikuta, T. Araki, M. Yoneda and Y. Matsuda: Acta metall., 1984, 32, 1779-1788.
14. I. Hrivnak, F. Matsuda, Z. Li, K. Ikeuchi and H. Okada: Trans. of JWRI., 1992, 21, 241-250.
15. I. Hrivnak, F. Matsuda, Z. Li and K. Ikeuchi: Trans. of JWRI., 1992, 21, 9-31.
16. C.L. Davis and J.E. King: Metall. Mater. Trans., 1994, 25A, 563- 573.

17. F. Matsuda, Z. Li, P. Bernasovsky, K. Ishihara and H. Okada: Weld. In the World., 1991, 29, 307-313.
18. F.S. Lepera: Metallogr., 1979, 12, 263-268.
19. C.L. Davis and J.E. King: Mater. Sci. Technol., 1993, 9, 8–15.

Paper 2

Cleavage fracture initiation at M-A constituents in the intercritically coarse grained heat affected zone of a HSLA steel.

Submitted to Metallurgical and Materials Transaction A

Is not included due to copyright

Paper 3

Slip system activation during low cycle fatigue at low temperatures in HSLA steels

Submitted to Materials Science and Engineering A

Is not included due to copyright

Paper 4

Application of combined EBSD and 3D-SEM technique on crystallographic facet analysis of the X80 steel at low temperature

Submitted to Journal of Microscopy

Is not included due to copyright

Paper 5

Determination of crystallographic facet orientations on fracture surfaces of an Arctic steel by using EBSD.

Proceedings of ISOPE 2012, Rhodes, Greece, June 18-24,
Vol. 4, pp. 305-309.

Determination of crystallographic facet orientations on fracture surfaces of an Arctic steel by using EBSD

Peyman Mohseni[1], Jan Ketil Solberg[1], Morten Karlsen[1], Odd M Akselsen [1,2], Erling Østby[2]

[1]Department of Material Science and Engineering, Norwegian University of Science and Technology (NTNU)
N-7491 Trondheim, Norway

[2]Department of Applied Mechanics and Corrosion, SINTEF,
Trondheim, Norway

ABSTRACT

Electron backscatter diffraction (EBSD) has been increasingly used to identify the crystallographic planes and orientation of cleavage facets with respect to the rolling direction in fracture surfaces. The crystallographic indices of cleavage planes can be determined either directly from the fracture surface or indirectly from metallographic sections perpendicular to the plane of the fracture surface. The commonly observed crystallographic mode (i.e. the micromechanism) of brittle fracture in ferritic steels is cleavage, which involves the separation of atomic bonds along low-index {100} crystallographic planes. The main purpose of this work was to identify the crystallographic orientations of cleavage facets in fracture surfaces with respect to the rolling direction of well known steel at low temperatures. The material used for the work was a steel (API X80 grade) that has been developed for applications at low temperatures. The crystallographic indices of the cleavage crack planes were identified to be {100}, {110}, {211} and {310} at all temperatures.

KEYWORDS: crystallographic facet analysis; EBSD; DBTT temperature; cleavage; ARCTIC steel.

INTRODUCTION

High strength and toughness pipeline steels have been used at high operation pressures to improve the transport efficiency of oil and gas. The major motivation behind the development of such steels has been to obtain the best combination of strength and toughness (Bose-Filho, Carvalho, Strangwood, 2007). Weldability, high fracture toughness and fatigue resistance at low temperatures are additional requirements for transmission of oil and gas through pipelines (Das, Sivaprasad, Dasa, Chatterjee and Tarafder, 2006). The balance of high strength and high toughness can be deteriorated by welding thermal cycles, producing local poor toughness in the welded joints (Lambert-Perlade, Gourgues, Besson, Sturel, and Pineau, 2004, Davis and King, 1996). The heat affected zone (HAZ) is in many cases considered to be the most critical part of a weld. The region of lowest toughness after single pass welding is the coarse grained heat affected zone (CGHAZ) (Qiu, Mori, Enoki and Kishi (2000) and Akselsen, Solberg and Grong, 1988). The main reason for this is attributed to the formation of unfavourable microstructures such as coarse ferrite side plates/upper bainite.

The ductile to brittle transition is characterized by a significantly drop in the energy absorbed by a steel subjected to impact loading. As temperature decreases, the ability of the steel to absorb impact energy decreases (Meier, 2004). Thus, its ductility decreases. In ferritic steels, this transition corresponds to a fracture mechanism change from ductile microvoid coalescence to cleavage, characterized by crack propagation along certain lattice planes (Davies, Novovoc, Randle and Bown, 2002). Low temperature performance and capability to resist large deformation are two features of large interest for arctic application of steel pipelines. Therefore, evaluation of low temperature toughness is required for safe operation and maintenance of pipeline steels (Shanmugam, Ramisetti, Misra, Hartmann and Jansto, 2008 and Bauer, Fluss, Amoris and Schwinn, 2005).

Most body centred cubic (BCC) metals fail by conventional cleavage at low temperatures, characterized by stress-controlled propagation of a single strain-

nucleated microcrack (Kumar, Wilkinson and S. G. Roberts, 2007). It is well established that conventional cleavage cracks propagate in the {100} or {110} crystallographic planes in ferritic and other BCC steels (Farkas, Nogueira, Ruda and Hyde, 2005). The separation process along these planes is considered energetically favourable due to their low surface energy (Davies and Randle, 2001). The surface energy of the {100} planes is less than that of the {110} family of planes. However, cleavage on {110} cannot be ruled out since the {110} family of planes is more closely packed with atoms than the {100} planes (Nohava, Hausˇild, Karlı´k and Bompard, 2003).

Electron backscatter diffraction (EBSD) has been developed for a range of applications including phase identification, grain and surface facet crystallography. The crystallographic indices of cleavage planes can for instance be identified by using EBSD, and this can be done in two ways. Either the crystallographic orientation is determined directly from the fracture surface or it is determined indirectly from a metallographically prepared surface perpendicular to and adjacent to the fracture surface (Randle and Davies, 2005 and Randle, 1999).

A combined 3D scanning electron microscope (SEM) imaging and EBSD technique has been developed to determine crystallographic facet orientations. The orientations are obtained by combining EBSD analysis from a polished section perpendicular to the fracture surface with a fracture surface profile analysis from 3D SEM images (Randle and Hoile, 1998 and Kumar, Wilkinson and S. G. Roberts, 2007). The main purpose of this paper has been to apply this method to identify the crystallographic planes and orientations of cleavage facets in low temperature fracture surfaces of Arctic steel.

EXPERIMENTAL

A commercial grade of API X80 pipeline steel with the chemical composition given in Table 1 was selected for the study.

Table 1 Chemical composition of the steel (mass %) [1]

C	Si	Mn	P	S	Cr	Cu	Ni	Mo
0.06	0.08	1.79	0.012	0.004	0.12	0.28	0.16	0.15

1 With 0.044%Nb, 0.013%Ti and 0.028%Al.

The relationship between the brittle to ductile transition temperature and the microstructure in coarse grained heat affected zone, CGHAZ, was studied by applying Smitweld TCS1405 weld simulation. To simulate CGHAZ microstructures, specimens of dimensions 11x11x100 mm^3 were cut with the longest dimension along the rolling direction of the pipe and subjected to HAZ simulation. During the thermal cycle, the specimen was heated to 1350°C followed by cooling at a rate corresponding to a cooling time between 800°C and 500°C ($\Delta t8/5$) of 15 seconds.

After the HAZ simulation, crack tip opening displacement (CTOD) specimens were machined with a 5 mm deep through width notch cut into the sample and subjected to CTOD testing at 0,-30,-60 and -90 ºC. The microstructures of the CGHAZ were examined optically with a Leica MEF4M microscope and with a scanning electron microscope (operated at 20kV and 82µA at 30µm aperture size). Samples were mechanically prepared by conventional grinding and polishing techniques and etched in a 2% Nital solution. A Zeiss Supra 55VP low vacuum field emission scanning electron microscope (LVFESEM) was used to observe the fracture surfaces and microstructures.

EBSD specimens were prepared by cutting length sections normal to the fracture surface close to the notch tip, so that EBSD could be made near the fracture surface with a TSL EBSD system interfaced with the SEM (Fig. 1).

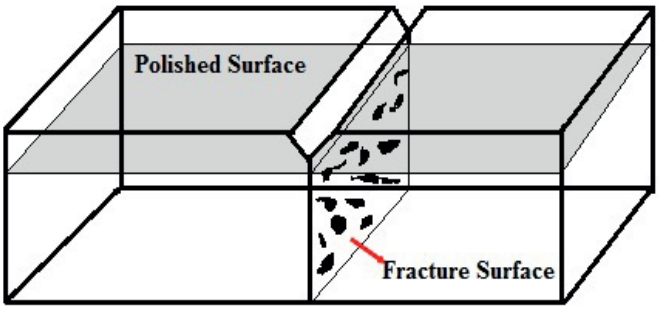

Fig.1. *Schematic diagrams showing a position from which EBSD samples were taken.*

These length sections were ground and polished down to 1μm and finally electropolished (at 20 V, 22 ºC) using Struers Lectropol 5 unit filled with H_2SO_4 elecrolyte (53,5 ml H_2SO_4 mixed with methanol to make a total of 1 liter solution). Computer assisted 3D-imaging was carried out by using the Mex software (Alicona imaging). During 3D imaging, images of a fracture surface are taken for at least two different tilt angles, and they are combined to produce a three-dimensional reconstruction of the fracture surface. This method is applied to measure the angles between the cleavage facets and the adjacent polished surface, and then this measurement is applied together with EBSD diffraction data to determine the crystallographic planes of the facets.

RESULTS and DISCUSSION

The obtained CTOD values vs. test temperature are shown in Fig.2 (Xu, Zhang, Østby, Nyhus and Sun, 2010). At all temperatures there is a scatter in the experimental results. The scatter increases with increasing temperatures, upper transition region, which can be explained as a result of the cleavage fracture initiation is preceded by ductile crack extension. The CTOD dependence on temperature could be represented by a sigmoidal curve. With decreasing test temperature from 0ºC the CTOD values decreased. At lower temperatures the behaviour was fully brittle; whereas at higher temperatures was ductile. The middle

part of the curve, the transition region, is characterized by a mixture of both types of failure. In these cases some ductile tearing prior to onset of cleavage fracture was observed for the higher CTOD values.

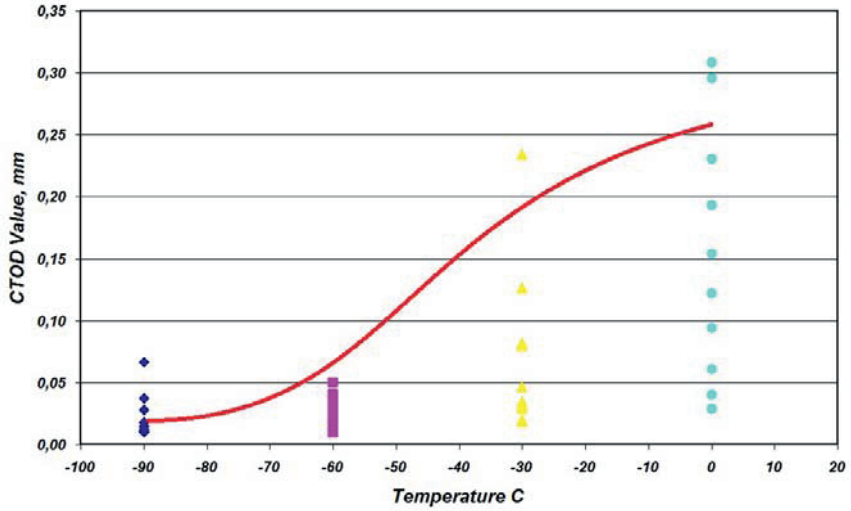

Fig. 2. *The variation of CTOD value with test temperature.*

Typical fracture surfaces of specimens fractured at different temperatures were presented in a previous work (Mohseni, Solberg, Akselsen and Østby, 2011). The fracture mechanism changed with test temperature from a mixture of ductile and brittle to completely brittle fracture with decreasing temperature from 0ºC to -90ºC. These fracture mechanisms are characteristic of high and low CTOD values, respectively.

As mentioned in the introduction paragraph, the crystallographic orientations were identified by a combination of EBSD analysis and fracture surface profile analysis obtained by 3D SEM. Validation of the 3D imaging procedure was achieved by performing a series of tests on a surface feature of known geometry. The Mex software was used to construct a 3D-model of a Vickers hardness indent where the angle between the faces of the pyramidal indent is 136º. Stereo images were acquired separately with the specimen tilted at +4 º and -4 º with respect to the

primary beam direction. The 3D image constructed by the Mex software corresponded very well with the known geometry of the indent, proving that the method can be used to determine the orientations of the cleavage facets and the angle between each facet and the polished surface.

An example of the application of this procedure on a fracture facet is given in the following. The sample is a specimen that was CTOD tested at -30 ºC. Fig. 3(a) shows the 3D- simulated image of the cleavage facet and the depth profile along the line AB oriented normal to the trace between the facet and the polished surface. The line profile shows that the angle α between the cleavage facet and the polished surface in this case is 65º, which is also the angle between the two plane normals.

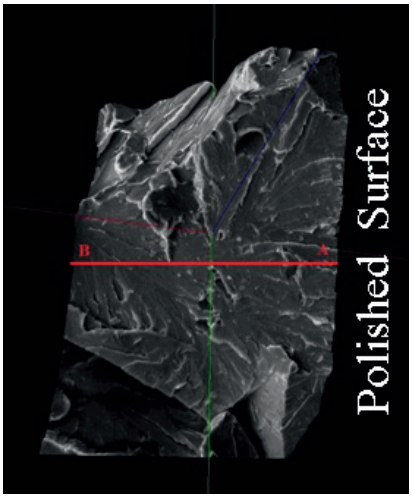

a) 3D- elevation model of the facets

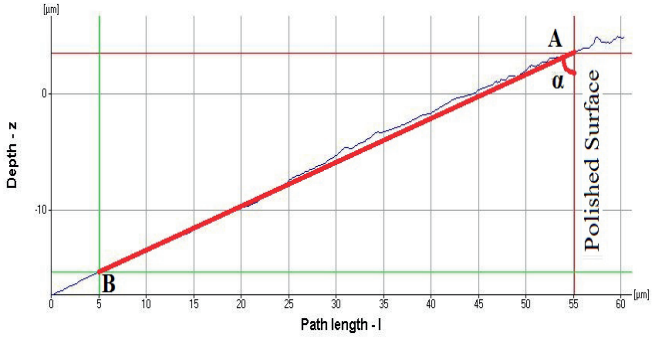

b) Height profile along the line shown in (a)

Fig. 3. *Fracture surface*

The further procedure for determining the crystallographic plane of the facet in Fig. 3(a) is illustrated in Fig. 4. Fig.4 (a) shows a secondary electron image from the metallographic polished length section through the fracture surface close to the fatigue crack tip (Fig.1). The trace of the cleavage facet in the fracture surface with the polished surface is indicated by the line T. According to literature data, in body centred cubic (bcc) metals and alloys, cleavage occurs along crystallographic planes of the families {100}, {110}, {211} and {310}. In this work, to identify the actual crystallographic cleavage plane of each facet, an EBSD pattern was recorded close to the line T, and from this pattern the poles of the possible cleavage planes were plotted in four individual pole figures, Fig.4 (b-e). The pole of the cleavage facet in Fig. 3(a) should be located along the line n, which is normal to the line T, in the pole figure. The exact position of the pole should be located 65º from the normal direction ND, given by the short line segment intersecting line n. From the four pole figures, it is seen that there is only a pole within the {310} family that coincides with this intersection, so the facet in Fig. 3(a) belongs to the {310} family.
This analysis was repeated for 40 cleavage facets for each test temperature. In Table 2 and Fig. 5, the number of cleavage facet planes of each type is shown for the samples that were CTOD tested at low temperatures. For example, we detected 18 {100} cleavage facet planes, 3 {110} planes, 9 {211} planes and 10 {310} planes for the specimen tested at 0ºC.

For all temperatures, facets of all four crystallographic planes were detected. It can be seen that, for each individual test temperature, the number of {100} facets is higher than the number of other facet planes.

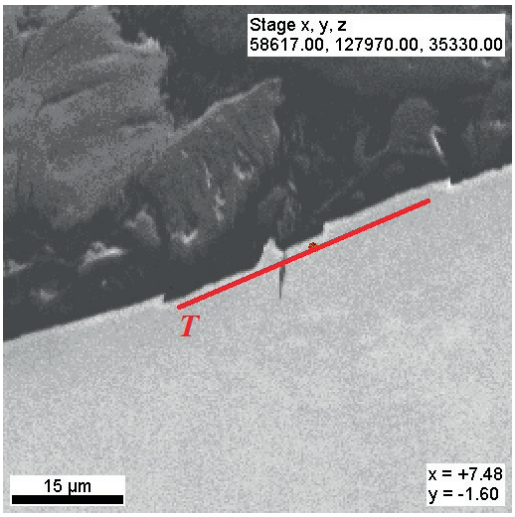

a) metallographic polished length section

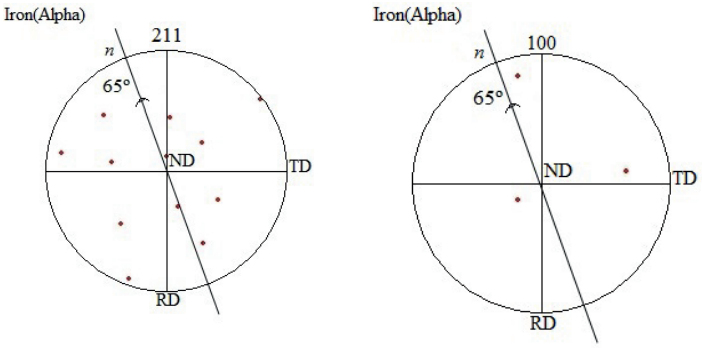

b) (211) pole figure *c) (100) pole figure*

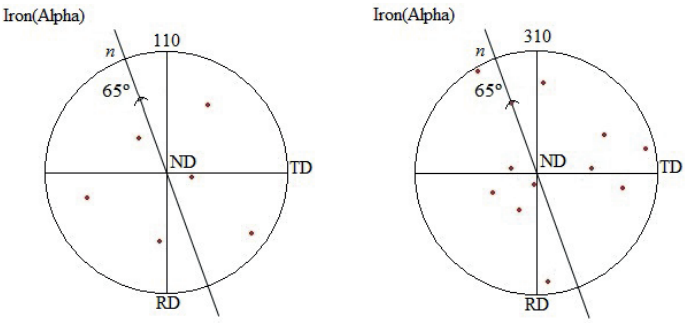

d) (110) pole figure *e) (310) pole figure*

Fig. 4. *EBSD result , RD : Rolling Direction, TD : Transverse Direction, ND: Normal Direction*

With decreasing test temperature from 0 ºC to -90 ºC, the number of facets within each family varies in a more or less random manner, but for the {100} facets there is a tendency toward decreasing the number with decreasing temperature, and the opposite is the case for the {110} facets. It seems that the increase in the number of {110} facets with falling temperature occurred at the expense of the number of {100} facets.

Table 2 Number of cleavage facets planes at different temperature

Crystallographic plane / Temperature	{100}	{110}	{211}	{310}
0ºC	18	3	9	10
-30ºC	11	10	10	9
-60ºC	16	7	5	12
-90ºC	13	8	9	10

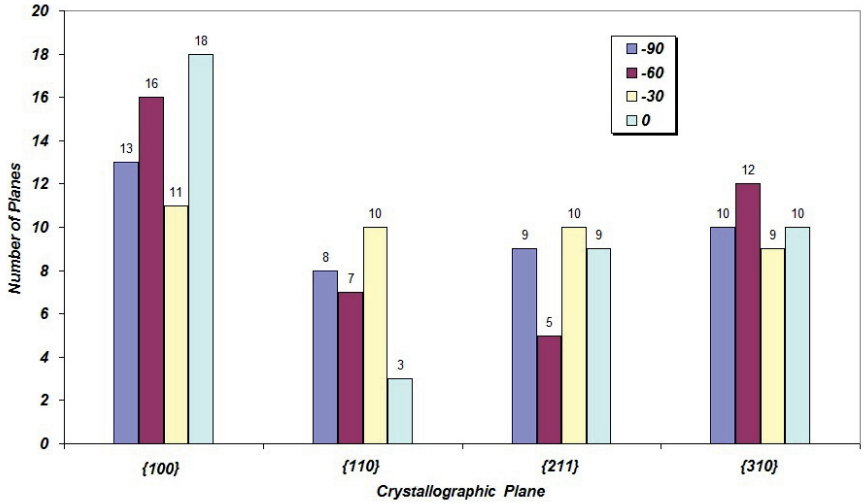

Fig. 5. *Distribution of cleavage plane at low temperature.*

In cubic crystals, there are 3 equivalent {100} planes, 6 equivalent {110} planes, 12 equivalent {211} planes and 12 equivalent {310} planes. If the number of cleavage

facets of each crystallographic type is divided by the number of equivalent planes within each family, we obtain a number that gives the potential of each single crystallographic plane to become a cleavage plane. For instance, in Table 3, it is seen that this 'normalized' value is much higher for a plane within the {100} family than for the other planes, proving that the {100} planes are the most potent cleavage planes at 0 ºC. According to Table 3, the probability that a cleavage facet is a {100} plane is 6 times higher than that it is a {110} plane, but the potential for an individual plane to become a cleavage plane is 12 times higher for a {100} plane than for a {110} plane. This agrees well with the general observation that cleavage cracks are mostly found to propagate along {100} crystal planes at lower temperatures in BCC metals because of their low surface energy and low decohesion critical stress given by elasticity theory (Nohava, Hausˇild, Karlı´k and Bompard, 2003). The {110} planes are also potent cleavage planes since they are closely packed with atoms, in fact more closely packed than the {100} planes are.

Table 3 Cleavage facet planes at 0 ºC

	{100}	{110}	{211}	{310}
Number of cleavage facets	18	3	9	10
Number of planes within each family	3	6	12	12
Normalized	**6**	0.5	0.75	0.83

Fig. 6 shows the normalized number of cleavage planes of each type for all test temperatures. It is seen that the {100} planes are by far the most potent cleavage planes at all temperature, and that the {110} planes are only slightly more potent than the {211} and {310} planes. The normalized number of {211} and {310} planes are nearly independent of temperature.

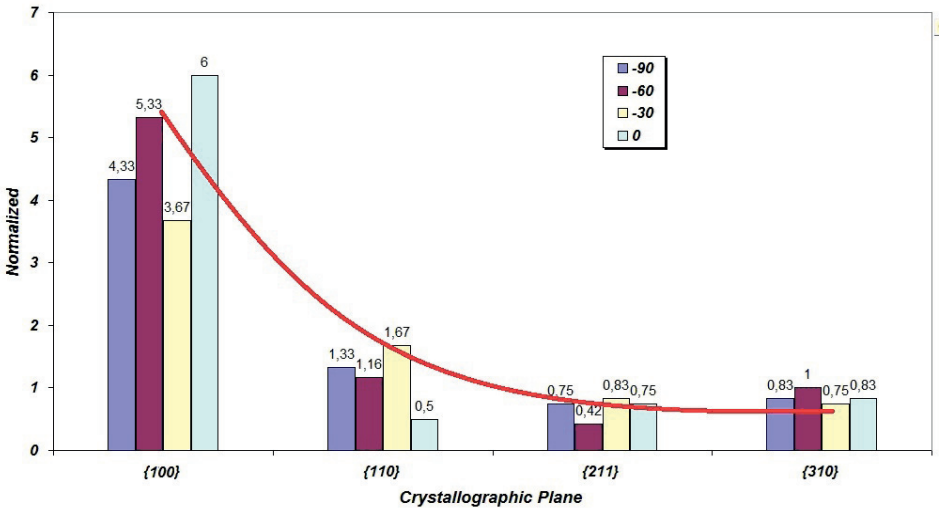

Fig. 6. *Distribution of normalized number of cleavage plane at low temperatures.*

It can be concluded that the {100} and {110} planes are the most potent cleavage planes at subzero temperatures, assuming that no crystallographic texture has influenced the experimental results. But due to the high number of equivalent {211} and {310} crystal planes, {211} and {310} facets were found with the same frequency as {110} facets in the brittle fracture surfaces.

CONCLUSIONS

In this investigation, electron backscatter diffraction has been applied to assess crystallographic features of fracture surfaces after CTOD testing of weld thermally simulated CGHAZ samples of an X80 steel. This technique has been combined with computer assisted 3D - imaging. The main conclusions of the work are:

1- The EBSD results also show that the cleavage trace directions on fractured samples were consistent with crack propagation on {100}, {110}, {211} and {310} planes.

2- The number of cleavage facet planes of the {100} family was significantly higher than those of other plane families in the test temperature range, especially if the number of cleavage facets were normalized with number of planes in each family.

3- In this investigation, with decreasing temperature, the tendency might be that the number of {100} facets seemed to decrease and the number of {110} facets seemed to increase. The numbers of {211} and {310} facets were nearly independent of temperatures.

4- The {100} and {110} planes are the most potent crystallographic planes for cleavage fracture at subzero temperatures.

ACKNOWLEDGEMENTS

The authors wish to thank the Research Council of Norway for funding through the Petromaks Programme. The financial support from ENI, Statoil, Total, Scana Steel Stavanger, JFE Steel Corporation, Nippon Steel Corporation, Brück Pipeconnections, Miras Grotnes, Bredero Shaw, Trelleborg, GE Oil and Gas, Aker Solutions and Technip is also acknowledged.

REFERENCES

Akselsen, OM, Solberg, JK, and Grong, Ø (1988). "Effects of martensite-austenite (M-A) islands on intercritical heat-affected zone toughness of low carbon miroalloyed steels," *Scand. J. Met.*, Vol 17, pp 194-200.

Bauer, J, Fluss, P, Amoris, E and Schwinn, V (2005). "Microstructure and properties of thermomechanical controlled processing steels for linepipe applications," *Ironmaking & steelmaking*, Vol 32, pp 325-330.

Bose-Filho, WW, Carvalho, ALM and Strangwood, M (2007). "Effect of alloying elements on the microstructure and inclustion formation in HSLA multipass welds," *Materials Characterization*, Vol 58, pp 29-39.

Das, SK, Sivaprasad, S, Dasa, S, Chatterjee, S, and Tarafder, S (2006). "The effect of variation of microstructure on fracture mechanics parameters of HSLA-100 steel," *Materials Science and Engineering*, Vol 431, pp 68-79.

Davis, CL, and King, JE (1996). "Cleavage initiation in the intercritically reheated coarse-grained heat affected zone: Part II. Failure criteria and statistical effects," *Metall. Mater. Trans.*, Vol 27A, pp 3019-3029.

Davies, PA, Novovoc, M, Randle, V and Bown, P (2002). "Application of electron backscatter diffraction (EBSD) to fracture studies of ferritic steels," *Journal of Microscopy,* Vol 205, pp 278–284.

Davies, PA and Randle, V (2001). "Combined application of electron backscatter diffraction and stereo-photogrammetry in fractography studies," *Journal of Microscopy*, Vol 204, pp 29-38.

Farkas, D, Nogueira, R, Ruda, M, and Hyde, B (2005). "Atomistic simulations of the effects of segregated elements on grain-boundary fracture in body centred cubic Fe," *Metallurgical and Materials Transactions A,* Vol 36A, pp 2067–2072.

Kumar, A, Wilkinson, AJ and Roberts, SG (2007). "Quasi-cleavage fracture planes in spheroidized A533B steel," *Journal of Microscopy,* Vol 227, pp 248-253.

Lambert-Perlade, A, Gourgues, AF, Besson, J, Sturel, T and Pineau, A (2004). "Mechanisms and Modeling of Cleavage Fracture in Simulated Heat-Affected Zone Microstructures of a High-Strength Low Alloy Steel," *Metallurgical and Materials Transactions A,* Vol 35A, pp 1039-1053.

Meier, M (2004). "The ductile to brittle transition", *Department of Chemical Engineering and Materials, University of California.*

Mohseni, P, Solberg, JK, Akselsen, OM, Østby, E (2011). "Application of electron backscatter diffraction (EBSD) on facet crystallographic orientation studies in Arctic Steels," *Proceeding of ISOPE,* Vol 4, pp 402-406.

Nohava, J, Hausˇild, P, Karlı´k, M and Bompard, P (2003). "Electron backscattering diffraction analysis of secondary cleavage cracks in a reactor pressure vessel steel," *Materials Characterization,* Vol 49, pp 211-217.

Qiu, H, Mori, H, Enoki, M and Kishi, T (2000). "Fracture Mechanism and toughness of the welding Heat – Affected zone in structural steel under static and dynamic loading," *Metallurgical and Materials Transactions A,* Vol 31A, pp 2785-2791.

Randle, V (1999). "Crystallographic analysis of facets using electron backscatter diffraction," *Journal of Microscopy*, Vol 195, pp 226-232.

Randle, V and Davies, P (2005). "Crystallography of brittle fracture and deformation twinning in ferritic steels," *Materials Science and Technology,* Vol 21, pp 1275-1281.

Randle, V. & Hoile, C. (1998). "Crystallographic analysis of facets using electron back-scatter diffraction," *Mater. Sci. Forum*, Vol 273, pp183.

Shanmugam, S, Ramisetti, NK, Misra, RDK, Hartmann, J and Jansto, SG (2008). "Microstructure and high strength–toughness combination of a new 700MPa Nb-microalloyed pipeline steel," *Materials Science and Engineering*, Vol 478, pp 26-37.

Xu, J, Zhang, ZL, Østby, E, Nyhus, B, and Sun, DB (2010). "Effects of temperature and crack tip constraint on cleavage fracture toughness in the weld thermal simulated X80 pipeline steel," *Proceeding of ISOPE,* Vol 4, pp 162-169.

Paper 6

Application of electron backscatter diffraction (EBSD) on facet crystallographic orientation studies in Arctic Steels.

Proceedings of ISOPE, 2011, Hawaii, USA, June 19-24, Vol. 4, pp. 402-406.

The EBSD results of this paper were also presented in paper 5. This paper also included due to the part of the results has been referred in the other papers.

Application of electron backscatter diffraction (EBSD) on facet crystallographic orientation studies in Arctic Steels

Peyman Mohseni[1], Jan Ketil Solberg[1], Odd Magne Akselsen[1,2], Erling Østby[2]
[1]Norwegian University of Science and Technology (NTNU)
Trondheim, Norway
[2]SINTEF,
Trondheim, Norway

ABSTRACT

Thick-walled high strength line pipes are being increasingly used for high-pressure pipeline operations to improve the transport efficiency for natural gas and oil. As an added challenge, pipeline construction for natural gas and oil transport is sometimes taking place in severe environments such as in the Arctic. Thus, the line pipe must have low-temperature toughness together with high tensile properties. In this work, a study of the relationship between the brittle to ductile transition temperature and the microstructure in HAZ was carried out by applying resistant heating weld simulation. The main purpose of the work was to identify the crystallographic orientation of the cleavage facets in the fracture surface with respect to the rolling direction of the steel. The steel selected for this study is API X80 grade. The application of electron backscatter diffraction (EBSD) provided a method for investigating the crystallography of the fracture facets. The results reveal that the crystallographic indices of the cleavage crack planes were identified to be (001), (110), (211) and (310).

KEY WORDS: brittle cleavage fracture; EBSD; arctic steel; crystallography.

INTRODUCTION

High strength low alloy steels are used for high pressure pipeline operations to improve the transport efficiency. Pipeline steels, used for transporting natural gas and oil over a long distance, become stronger, tougher, larger, and thicker for cost reduction and high pressure transportation. The pipeline construction is sometimes taking place in severe environments such as in the Arctic. Thus, the demand for higher strength and toughness in pipeline steels has increased (Bose-Filho, Carvalho, Strangwood 2007; Das, Sivaprasad, Dasa, Chatterjee and Tarafder, 2006).
HSLA steels combine excellent tensile strength and ductile-to-brittle transition (DBT) properties. However, this combination of high strength and high fracture toughness can be deteriorated by welding thermal cycles. The degradation of the fracture toughness of HSLA steels after welding is attributed to the formation of "local brittle zones" in the welded joint (Lambert-Perlade, Gourgues, Besson, Sturel, and Pineau, 2004).

According to literature data, the fracture toughness of these local brittle zones is influenced by metallurgical factors such as prior austenite grain size, bainite packet size, and distribution of second phases such as carbides and martensite austenite (M-A) constituents (Chen et al, 1984; Akselsen et al, 1987 and 1988, Davis and King, 1994 and 1996; Li et al, 2001; Li and Baker, 2010). The cleavage-facet size has been related to the prior austenite grain size. Low temperature performance and capability to resist heavy deformation are two features of large interest for arctic application of steel structures. The low temperature requirements raise the focus on brittle fracture behaviour (Shanmugam, Ramisetti, Misra, Hartmann and Jansto, 2008; Bauer, Fluss, Amoris and Schwinn, 2005).

For ferritic steels with a body centered cubic lattice (BCC), there is a transition from ductile to brittle fracture when the temperature is reduced. This temperature dependency can be represented by a sigmoidal curve. The lower and upper plateaus are associated with brittle and ductile fracture, respectively. The middle part of the

curve, the transition region, is characterized by a mixture of both types of fracture (Davies, Novovoc, Randle and Bown, 2002).

The commonly observed crystallographic mode of brittle fracture in ferritic steels is cleavage, which involves the separation of atomic bonds along low-index {001} crystallographic planes. The separation process along these planes is considered energetically favourable due to their low surface energy. The surface energy of the {001} planes is less than that of the {011} family of planes. However, cleavage on {011} can not be ruled out, since the {011} family of planes is more closely packed with atoms than the {001} planes (Davies and Randle, 2001; Nohava, Hausˇild, Karlı´k and Bompard, 2003).

Determination of the crystallographic orientation of facets on a fracture surface can be used to establish the mechanisms of failure, or to distinguish between different failures modes (Wert and Robertson, 1982). For example, determination of facet plane orientations has been used to show that 'quasicleavage' fracture in steels occurs on the same crystallographic planes as cleavage fracture and therefore probably occurs by similar mechanisms.

Experimental determination of crystallographic facet orientations is difficult. X-ray diffraction techniques can be used for establishing cleavage planes in single crystals or polycrystal specimens. Etch pit orientation studies have been used by several Japanese workers to establish the orientation of quasicleavage facets in tempered martensite (Wert and Robertson, 1982).

The techniques previously developed for determining the crystallographic orientation of facets on fracture surfaces have two features: 1- they are generally applicable only in certain cases (for large grain size) 2- they destroy the fracture surface (etch pit orientation). Electron backscatter diffraction (EBSD) has superseded the first two techniques for a range of applications including

microtexture, phase identification, grain boundary characterization and facet crystallography (Randle, 1999).

The application of electron backscatter diffraction (EBSD) to fracture studies has provided a new method for investigating the crystallography of fracture surfaces. The crystallographic indices of cleavage planes can be measured both directly from the fracture surface and indirectly from metallographic sections perpendicular to the plane of the adjoining fracture surfaces (Randle and Davies, 2005). A two-dimensional analysis technique has been used in which EBSD measured crystal orientations were combined with secondary electron imaging to obtain the trace of the crack facet on the section plane (Kumar, Wilkinson and S. G. Roberts, 2007). The main purpose of this paper is to identify the crystallographic planes and orientation of cleavage facets with respect to the rolling direction in the fracture surface of steel. The crystallographic orientations were obtained by EBSD from a polished section perpendicular to the major fracture surface of the sample.

EXPERIMENTAL

A commercial grade of X80 pipeline steel plates with the chemical composition shown in Table 1 was used for this experiment. The microstructure of the steel is illustrated in Fig.1.

Table 1 Chemical Composition of the steel (mass %)

C	Si	Mn	Cr	Ni	Mo
0.06	0.08	1.79	0.12	0.16	0.15
P	S	Nb	Ti	Al	Cu
0.012	0.004	0.044	0.013	0.028	0.28

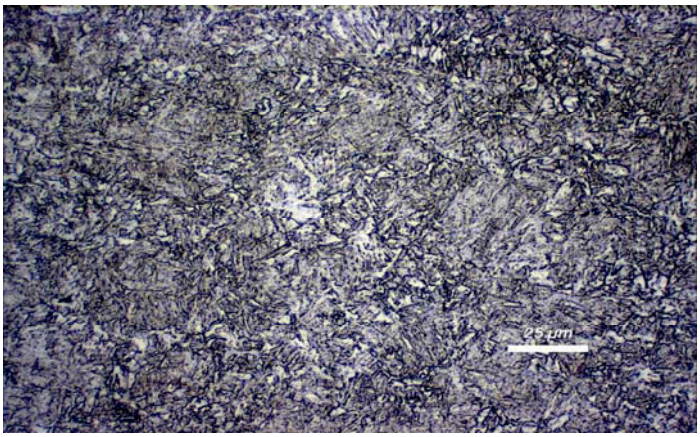

Fig. 1. *Microstructure of Base Metal.*

The relation between the brittle to ductile transition temperature and the microstructure in coarse grained heat affected zone, CGHAZ, has been studied by applying weld simulation. Specimens of dimensions 10*10*100 mm^3 were cut with the longest dimension along the rolling direction from the plates and subjected to thermal cycle with peak temperature of 1350°C and cooling time between 800 and 500°C of 15 seconds (Table 2) in order to simulate the CGHAZ microstructures.

Table 2 The thermal cycle for the simulation of HAZ

Peak temperature T_P (°C)	1350
Holding time at 1350°C	1s
Cooling time $\Delta t_{8/5}$	15s

After the HAZ simulation, CTOD specimens were machined with a 5 mm deep through width notch cut into the sample and subjected to CTOD testing at 0,-30,-60,-90 ºC. The microstructures of the CGHAZ were examined by optical and scanning electron microscopy (SEM). The fracture surfaces were also examined in the scanning electron microscope (SEM), and this study showed that the steel had failed by quasicleavage at all temperatures.

EBSD specimens were prepared by cutting length sections normal to the fracture surface close to the notch tip, so that EBSD could be made near the fracture surface. These length sections were ground and polished down to 1μm and finally electropolished (at 20 V, 22 ºC) using Struers Lectropol 5 unit filled with H_2SO_4 elecrolyte (1L = 53,5 mL H_2SO_4 and rest Methanol). Computer assisted 3D-imaging was carried out by using the Mex software (Alicona imaging). This software was used to construct a 3D-Image model of a number of cleavage facets on the fracture surface, and measurement of the slope of each cleavage facet plane with respect to the electropolished surface was then applied together with EBSD diffraction data to determine the crystallographic planes of the facet.

RESULTS

A typical microstructure of the coarse grained heat affected zone (CGHAZ) is shown in Fig.2. The acicular ferrite microstructure of base metal had transformed to upper bainite with fairly large prior austenite grain size during the simulated weld thermal cycle.

Fig. 2. *Microstructure of CGHAZ*

The obtained CTOD values vs. test temperature are shown in Fig.3. It is seen that, with decreasing test temperature from 0ºC, the CTOD values decrease and reach a minimum at temperatures in the range -60 ºC to -90 ºC (Xu, Zhang, Østby, Nyhus, Sun, 2010).

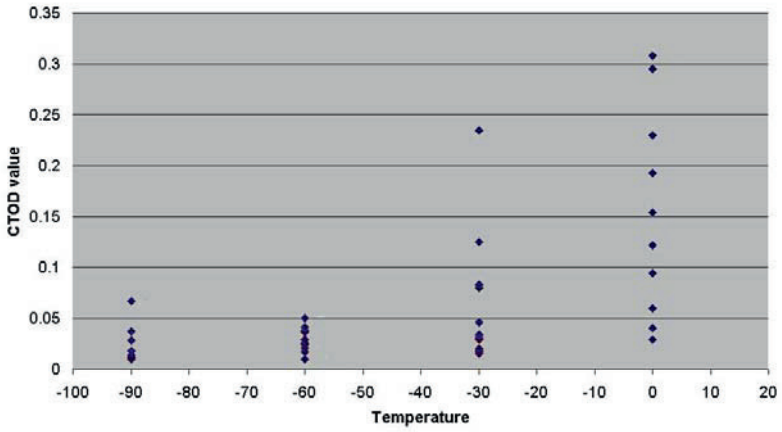

Fig. 3. *The variation of CTOD value with test temperature*

The temperature dependence of the CTOD values could be represented by a sigmoidal curve. The lower and upper shelves were associated with brittle and ductile fracture, respectively. Typical fracture surfaces of specimens fractured at different temperatures are shown in Fig.4. As is seen, the fracture mechanism changes with the test temperature from ductile (dimple deformation type) to a mixture of ductile and brittle and finally to completely brittle with decreasing temperature from 0ºC to -90ºC. These fracture mechanisms are characteristic of high, medium and low CTOD values.

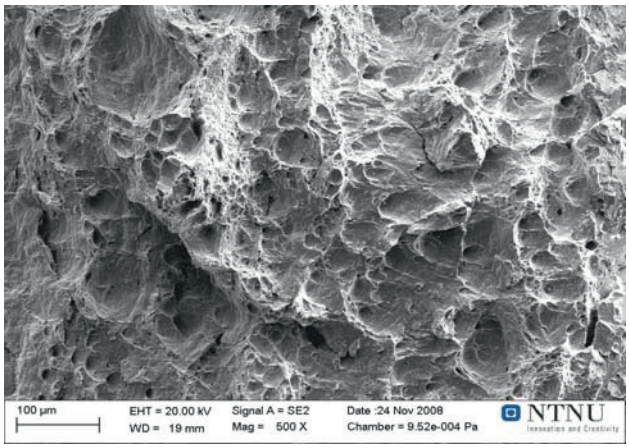

a) 0ºC (upper)

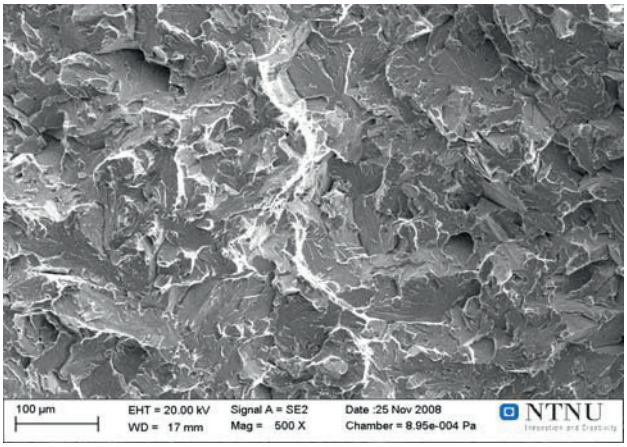

b) -30ºC (middle)

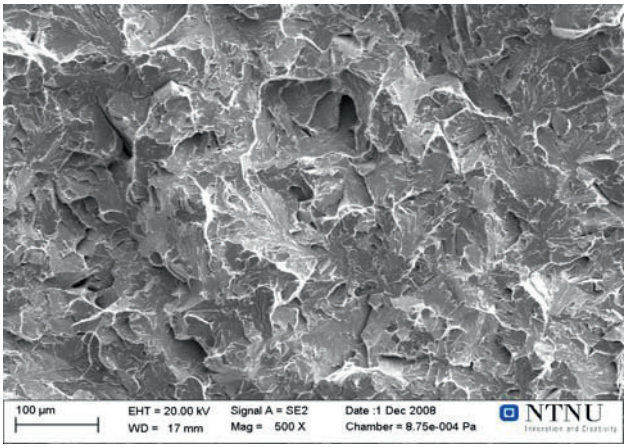

c) -90ºC (lower)

Fig. 4. *Fracture surface of the specimen at different temperature.*

Validation of the 3D imaging procedure was achieved by a series of tests on a surface feature of known geometry. The Mex software was used to construct a 3D-model of the Vickers hardness indent where the angle between the faces of the pyramidal indent is 136º. Stereo images were acquired separately, tilted at +4 º and -4 º with respect to the primary beam direction. The 3D image constructed by the Mex software corresponded very well with the known geometry of the indent, proving that the method can be used to determine the orientations of the cleavage facets and the angle between each facet and the polished surface. An example of the application of this procedure is shown in Fig.5. Fig. 5 (a) shows the 3D- simulated image of a cleavage facet and the depth profile along the line AB oriented normal to the trace between the facet and the polished surface. The line profile shows that the angle α between the cleavage facet and the polished surface in this case is 68º, which is also the angle between the two plane normals.

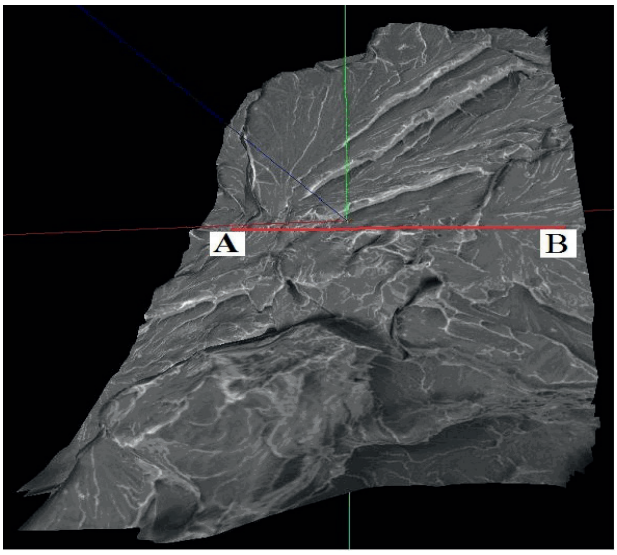

a) 3D- elevation model of the facets

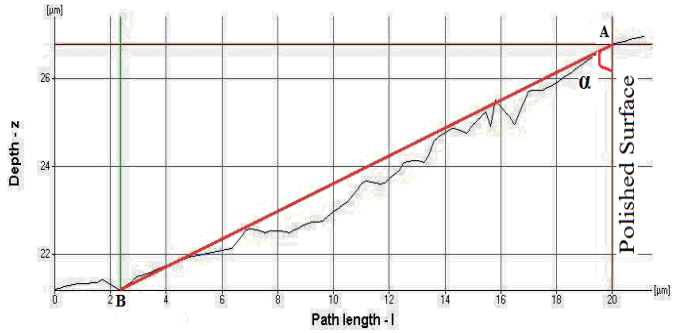

b) Height profile along the line shown in (a)

Fig. 5. *Micrograph of a region on a fracture surface*

The further procedure for determining the crystallographic plane of the facet in Fig. 5 (a) is illustrated in Fig. 6. Fig.6 (a) shows a secondary electron image from metallographic polished length section through the fracture surface close to the fatigue crack tip. The trace of the cleavage facet in the fracture surface with the polished surface is indicated by the line T. According to literature data, in body centred cubic (bcc) metals and alloys, cleavage occurs along crystallographic planes of the families {100}, {110}, {112} and {310} (Nohava, Hausˇild, Karlı´k and Bompard, 2003). In this work, to identify the actual crystallographic cleavage plane of each facet, an EBSD pattern was recorded close to the line T, and from this pattern the poles of the possible cleavage planes were plotted in four individual pole figures, Fig.6 (b-e). The pole of the cleavage facet in Fig. 5(a) should be located along the line n, which is normal to the line T, in the pole figure. The exact position of the pole should be located 68º from the normal direction ND, given by the short line segment intersecting line n. From the four pole figures, it is seen that there is only a pole within the {110} family that coincides with this intersection, so the facet in Fig. 5 (a) belongs to the {110} family.

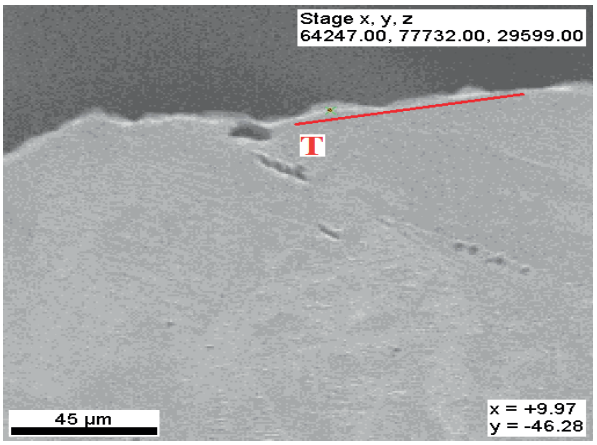

a) metallographic polished length section

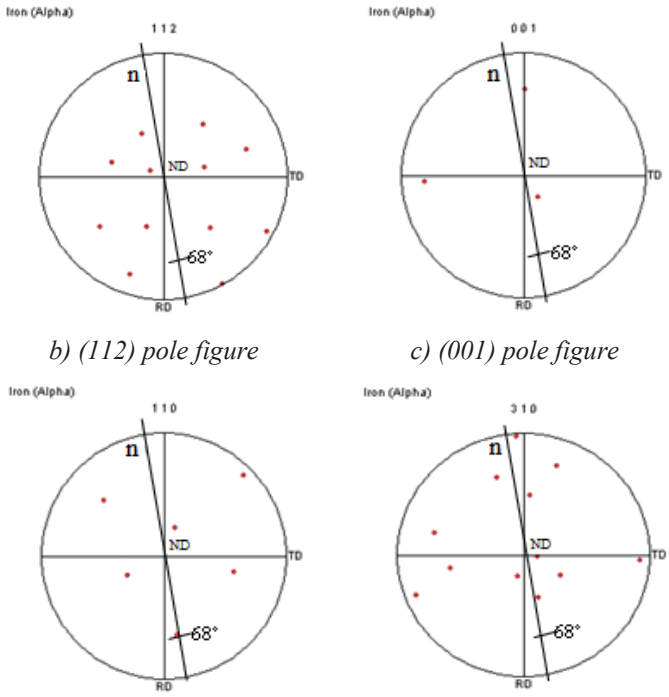

b) (112) pole figure *c) (001) pole figure*

d) (110) pole figure *e) (310) pole figure*

Fig. 6. *EBSD result , RD : Rolling Direction, TD : Transverse Direction, ND: Normal Direction*

This analysis was repeated for 20 cleavage facets for each test temperature. Table 3 shows the number of facet planes of each type for the sample that was CTOD tested

at -60 ºC. In this sample we detected 5 {001} cleavage facet planes, 7 {110} planes, 5 {112} planes and 3 {310} planes.

Table 3 Crack planes

	{001}	{110}	{112}	{310}
Number of cleavage facets	5	7	5	3
Number of planes within each family	3	6	12	12
Normalized	1.67	1.16	0.42	0.25

DISCUSSION

The examined cleavage facets were found to propagate along {100}, {110}, {112} and {310} crystallographic planes. Because of its low surface energy and a low critical stress for decohesion given by the elastic theory, cleavage cracks are mostly found to propagate along {100} crystal planes at lower temperature in BCC metals (Nohava, Hausˇild, Karlı´k and Bompard, 2003).

In ferritic steels, however, it is not uncommon to find cleavage cracks also propagating in the {110} and {112} planes (Kumar, Wilkinson and S. G. Roberts, 2007). Crack growth in cleavage planes different from {100} is facilitated by an even crystallographic distribution of bainitic packets in the material. For each crystal, there are 3 {001} planes, 6 {110} planes, 12 {112} planes and 12 {310} planes. If the number of cleavage facets of each crystallographic type is normalized to the total number of available planes within each family, Table 3 shows that the {100} and {110} planes are the most favourable cleavage planes at -60 ºC , assuming there is no crystallographic texture in the HAZ of the specimen.

The crack plane selected in any given grain in the polycrystal is determined by how the local stress state is oriented with respect to the possible crack planes and slip systems.

CONCLUSIONS

In this investigation, electron backscatter diffraction has been applied to assess crystallographic features of fracture surfaces. This technique has been combined with computer assisted 3D- Imaging. The main conclusions of the work are:

1- The fracture mechanism changes with the test temperature from ductile to completely brittle with decreasing temperature form 0ºC to -90ºC; corresponding to the upper and lower part of the CTOD vs. temperature curve.

2- The EBSD results show that the cleavage trace directions on fractured samples were consistent with crack propagation on {001}, {110}, {112} and {310} planes. If the number of cleavage facets of each plane type is normalized to the total number of planes available within each family, the {001}, and the {110} planes are the most favourable cleavage facet planes at -60ºC.

REFERENCES

Akselsen, OM, Solberg, JK, and Grong, Ø (1988). "Effects of martensite-austenite (M-A) islands on intercritical heat-affected zone toughness of low carbon miroalloyed steels," *Scand. J. Met.*, Vol 17, pp 194-200.

Akselsen, OM, Grong, Ø, and Solberg, JK (1987). "Structure-property relationships in intercritical heat affected zone of low carbon microalloyed steels," *Mater.Sci.Technol.*, Vol 3, pp 649-655.

Bose-Filho, WW, Carvalho, ALM and Strangwood, M (2007). "Effect of alloying elements on the microstructure and inclustion formation in HSLA multipass welds," *Materials Characterization*, Vol 58, pp 29-39.

Bauer, J, Fluss, P, Amoris, E and Schwinn, V (2005). "Microstructure and properties of thermomechanical controlled processing steels for linepipe applications," *Ironmaking & steelmaking*, Vol 32, pp 325-330.

Chen, JH, Kikuta, Y, Araki, T, Yoneda, M, and Matsuda, Y (1984). "Micro-fracture behavior induced by M-A constituent (island martensite) in simulated welding heat

affected zone of HT80 high strength low alloy steel," *Acta Metall.*, Vol 32, pp 1779-1788.

Davis, CL, and King, JE (1994). "Cleavage initiation in the intercritically reheated coarse-grained heat affected zone: Part I. Fractographic evidence," *Metall. Mater. Trans.*, Vol 25A, pp 563-573.

Davis, CL, and King, JE (1996). "Cleavage initiation in the intercritically reheated coarse-grained heat affected zone: Part II. Failure criteria and statistical effects," *Metall. Mater. Trans.*, Vol 27A, pp 3019-3029.

Davies, PA and Randle, V (2001). "Combined application of electron backscatter diffraction and stereo-photogrammetry in fractography studies," *Journal of Microscopy*, Vol 204, pp 29-38.

Das, SK, Sivaprasad, S, Dasa, S, Chatterjee, S, and Tarafder, S (2006). "The effect of variation of microstructure on fracture mechanics parameters of HSLA-100 steel," *Materials Science and Engineering*, Vol 431, pp 68-79.

Davies, PA, Novovoc, M, Randle, V and Bown, P (2002). "Application of electron backscatter diffraction (EBSD) to fracture studies of ferritic steels," *Journal of Microscopy,* Vol 205, pp 278–284.

Kumar, A, Wilkinson, AJ and Roberts, SG (2007). "Quasi-cleavage fracture planes in spheroidized A533B steel," *Journal of Microscopy,* Vol 227, pp 248-253.

Lambert-Perlade, A, Gourgues, AF, Besson, J, Sturel, T and Pineau, A (2004). "Mechanisms and Modeling of Cleavage Fracture in Simulated Heat-Affected Zone Microstructures of a High-Strength Low Alloy Steel," *Metallurgical and Materials Transactions A,* Vol 35A, pp 1039-1053.

Li, Y, and Baker, T (2010). "Effect of morphology of martensite-austenite phase on fracture of weld heat affected zone in vanadium and niobium microalloyed steels," *Mater. Sci. Technol.*, Vol 26, pp 1029-1040.

Li, Y, Crowther, N, Green, MJW, Mitchell, PS, and Baker TN (2001). "The effect of vanadium and niobium on the properties and microstructure of the intercritically reheated coarse grained heat affected zone in low carbon microalloyed steels," ISIJ Int., Vol 41, pp 46-55

Nohava, J, Hausˇild, P, Karlı´k, M and Bompard, P (2003). "Electron backscattering diffraction analysis of secondary cleavage cracks in a reactor pressure vessel steel," *Materials Characterization,* Vol 49, pp 211-217.

Randle, V (1999). "Crystallographic analysis of facets using electron backscatter diffraction," *Journal of Microscopy*, Vol 195, pp 226-232.

Randle, V and Davies, P (2005). "Crystallography of brittle fracture and deformation twinning in ferritic steels," *Materials Science and Technology,* Vol 21, pp 1275-1281.

Shanmugam, S, Ramisetti, NK, Misra, RDK, Hartmann, J, and Jansto, SG (2008). "Microstructure and high strength–toughness combination of a new 700MPa Nb-microalloyed pipeline steel," *Materials Science and Engineering*, Vol 478, pp 26-37.

Wert, JA and Robertson, WM (1982). "Determination of crystallographic facet orientations on fracture surfaces," *Metallography*, Vol 15, pp 367-381.

Xu, J, Zhang, ZL, Østby, E, Nyhus, B, and Sun, DB (2010). "Effects of temperature and crack tip constraint on cleavage fracture toughness in the weld thermal simulated X80 pipeline steel," Proceeding of IS.